INVESTIGATING BIOSPHERE-ATMOSPHERE INTERACTIONS

FROM LEAF TO ATMOSPHERIC BOUNDARY LAYER SCALES

by

Jehn-Yih Juang

Nicholas School of the Environment and Earth Sciences
Duke University

Date: March 6, 2007

Approved:

Gabriel Katul, Supervisor

Ram Oren

Prasad Kasibhatla

John Albertson

Amilcare Porporato

Dissertation submitted in partial fulfillment of
the requirements for the degree of Doctor
of Philosophy in the Nicholas School of the
Environment and Earth Sciences in the Graduate School
of Duke University

2007

ABSTRACT

INVESTIGATING BIOSPHERE-ATMOSPHERE INTERACTIONS FROM LEAF TO ATMOSPHERIC BOUNDARY LAYER SCALES

by

Jehn-Yih Juang

Nicholas School of the Environment and Earth Sciences
Duke University

Date: March 6, 2007

Approved:

Gabriel Katul, Supervisor

Ram Oren

Prasad Kasibhatla

John Albertson

Amilcare Porporato

An abstract of a dissertation submitted in partial fulfillment of the requirements for the degree of Doctor of Philosophy in the Nicholas School of the Environment and Earth Sciences in the Graduate School of Duke University

2007

Abstract

The interaction between terrestrial ecosystems and the atmosphere continues to be a central research theme within climate, hydrology, and ecology communities. This interest is stimulated by research issues pertinent to both the fundamental laws and the hierarchy of scales. To further explorer such topics over various spatial and temporal domains, in this study, biosphere-atmosphere interactions are studied at two different scales, leaf-to-canopy and canopy-to-atmospheric boundary-layer (ABL) scales, by utilizing both models and long-term measurements collected from the Duke Forest AmeriFlux sites.

For the leaf-to-canopy scale, two classical problems motivated by contemporary applications are considered: (1) 'inverse problem' – determination of nighttime ecosystem respiration, and (2) forward problem – estimation of two-way interactions between leaves and their microclimate ''. An Eulerian inverse approach was developed to separate aboveground respiration from forest floor efflux using mean CO_2 concentration and air temperature profiles within the canopy using detailed turbulent transport theories. The forward approach started with the assumption that canopy physiological, drag, and radiative properties are known. The complexity in the turbulent transport model needed for resolving the two-way interactions was then explored. This analysis considered a detailed multi-layer ecophysiological and radiative model embedded in a hierarchy of Eulerian turbulent closure schemes ranging from well-mixed assumption to third order closure schemes with local thermal-stratification within the canopy.

For the canopy-to-ABL scale, this study mainly explored problems pertinent to the impact of the ecophysiological controls on the regional environment. First, the possible combinations of water states (soil moisture and atmospheric humidity) that trigger convective rainfall were investigated, and a distinct 'envelope' of these combinations emerged from the measurements. Second, an analytical model as a function of atmospheric and ecophysiological properties was proposed to examine how the potential to trigger convective rainfall shifts over different land-covers. The results suggest that pine plantation, whose area is projected to dramatically increase in the Southeastern US (SE), has greater potential to trigger convective rainfall than the other two ecosystems. Finally, the interplay between ecophysiological and radiative attributes on surface temperature, in the context of regional cooling/warming, was investigated for projected land-use changes in the SE region.

Contents

List of Tables

List of Figures

1. Overall Introduction

The estimation of carbon and water fluxes from/to terrestrial ecosystems remains a central research theme within the climate, ecology, hydrology, and atmospheric science communities. This interest is most visible by the science questions articulated in the global carbon and water cycle plans within the United States Global Change Research Program. Recent studies have already confirmed that the North American terrestrial ecosystem is a net carbon sink with clear annual to inter-annual variability [*Battle et al.*, 2000; *Bousquet et al.*, 2000; *Fan et al.*, 1998; *Holland et al.*, 1999; *Houghton*, 2000; *Keeling et al.*, 1996]. This variability pattern is strongly linked to climatic and other environmental forcing, as well as the ecosystem functional and structure properties. To characterize the interactions between the ecosystems and their environment in a diagnostic and prognostic manner, it is necessary to explore two inter-related problems: the transfer from (i) leaf to canopy and (ii) the canopy to the atmospheric boundary-layer (ABL) in equilibrium with the landscape.

At the canopy scale, one of the major challenges for quantifying ecosystem carbon budgets from micrometeorological methods remains nighttime ecosystem respiration. [*Baldocchi et al.*, 1996; *Goulden et al.*, 1996; *Law et al.*, 1999a; *Law et al.*, 1999b; *Lindroth et al.*, 1998; *Moncrieff et al.*, 1996; *Schmid et al.*, 2000; *Valentini et al.*, 2000; *Wofsy et al.*, 1993]. An earlier study [*Lai et al.*, 2002a] utilized a constrained source optimization (CSO) method using inverse Lagrangian dispersion theory to infer the two components of ecosystem respiration (aboveground and forest floor) from

measured mean atmospheric CO_2 concentration profiles within the canopy. This method required measurements of within-canopy mean velocity statistics, and did not consider local thermal stratification, which could play a significant role on estimating the carbon budget.

In addition to the nighttime ecosystem respiration, modeling the transfer of heat, water vapor, and CO_2 between the biosphere and the atmosphere inside the canopy remains frustrated by complex two-way interactions between leaves and their immediate microclimate. In applications that require modeling fluxes of these scalars on seasonal to inter-annual time scales, the so-called well-mixed assumption (WMA) [*Aber et al.*, 1996; *De Pury and Farquhar*, 1997; *Kirschbaum et al.*, 1998; *Leuning et al.*, 1995; *Luo et al.*, 2001; *Naumburg et al.*, 2001; *Wang and Leuning*, 1998; *Williams et al.*, 1996; *Williams et al.*, 1998] of mean concentration is often employed, thereby eliminating the need to model how vegetation alters its microclimate. Furthermore, uncertainties in describing the non-stationarity and vertical inhomogeneity in physiological parameters (e.g., in photosynthesis calculations) may overshadow any improvements gained by resolving this 2-way interaction. While the WMA may be defensible for some canopy types, it is too simplistic for tall-forested ecosystems, especially when such an assumption is confronted with experimental evidence that vertical variations in excess of 50 ppm for CO_2 concentration and 3 degrees or more for air temperature occur inside the canopy volume during day time conditions [*Lai et al.*, 2002a; *Siqueira and Katul*, 2002] . Because the vertical variations in mean scalar concentration profiles are not random within the

canopy, the WMA may inject systematic biases in modeling scalar sources, sinks, and fluxes.

In the canopy to ABL scaling, increasing attention is now given to investigating how variability of such biosphere-atmosphere interactions occur over different landscapes and how they exert control on the local meteorology (hydrological cycle, radiative budget), especially local convective rainfall mechanisms and changes in surface temperature (say following conversion of land-cover).

The Southeastern United States (SE) timberland ecosystems are among the most productive in North America and act as an important carbon sink within the continental United States [*Houghton et al.*, 1998; *Schimel*, 1995; *Tans and White*, 1998]. This high productivity is generally attributed to the moderate climate (mean annual temperature ~ 15.5 ^{o}C) and to the significantly large growing-season rainfall (~95 mm month^{-1}). Over the past half century, the timberland acreage of the SE ecosystems experienced only minor fluctuations (between 196 million in 1989 and 209 million in 1953), and is currently about 48% of the total land area. However, the composition of timberland is undergoing dramatic changes. The proportion of planted pine forests to the total timberland area in the SE has dramatically increased from under 1.0% in the early 1950s to about 15.0% in 1999, and is expected to rise steadily to 32.0% by the year of 2040 [*Wear and Greis*, 2002]. The summertime rainfall regime most likely to be impacted by such land-use change is convective rainfall because of its sensitivity to the local land-atmosphere heat and moisture exchange rates. To date, the implications of this projected land cover change on growing-season rainfall remains a vexing problem because of the

numerous nonlinear feedback mechanisms between soil moisture content and the atmospheric state.

Furthermore, the triggers of summertime convective rainfall depend on numerous interactions and feedbacks, often compounded by spatial variability in soil moisture and its impacts on vegetation function, vegetation composition, terrain, and all the complex turbulent entrainment processes near the capping inversion. To progress even within the most restricted and idealized framework, many of the governing processes must be simplified and parameterized.

In addition to the growing season convective rainfall, one interest is the impact of such land cover change on the local climate. Land use conversion, whether be it natural or anthropogenic is considered among the strongest climate forcing mechanisms at global and regional scales (e.g. *Cess* [1978], *Charney et al* [1977], and *Otterman* [1977]). Small changes in surface albedo (α_s), even below detection limits of existing satellite-derived products, can lead to global temperature changes equivalent to any of the enhanced green house gases [*Charlson et al.*, 2005]. At regional scales, following the projected land-cover change in the SE region, maximum change in air temperature occurs when all changes in surface temperature translate to air temperature. Hence, by locally (i.e. at the field scale) exploring how land-conversion influences surface temperature through changes in the surface properties (albedo, emissivity, and bulk aerodynamic conductance), some constraints on the larger climate system can be formulated.

2. Modeling nighttime ecosystem respiration from measured CO_2 concentration and air temperature profiles using inverse methods

2.1. Background and Introduction

Long-term measurements of net ecosystem exchange (NEE) are now routinely employed to estimate ecosystem carbon budgets using eddy-covariance (EC), yet the large error in the measurement of ecosystem respiration (R_E) under nighttime conditions remains an unresolved problem that must be confronted [*Baldocchi et al.*, 1996; *Goulden et al.*, 1996; *Law et al.*, 1999a; *Law et al.*, 1999b; *Lindroth et al.*, 1998; *Moncrieff et al.*, 1996; *Schmid et al.*, 2000; *Valentini et al.*, 2000; *Wofsy et al.*, 1993]. Often, nocturnal conditions are dominated by vertical subsidence, lack of steadiness in mean atmospheric conditions, and intermittent turbulent transport often initiated by transients such as passage of clouds [*Cava et al.*, 2004]. When viewed from the one-dimensional vertically integrated scalar continuity equation, these factors contribute to increased "de-coupling" between the desired R_E quantity and the CO_2 flux above the canopy, the latter being the observed quantity by EC methods. Furthermore, these nocturnal conditions tend to amplify the limitations of the EC instrument configurations for measuring the turbulent flux. For example, separation distance between gas analyzers and anemometers, volume averaging by anemometers across some path length, and finite sampling periods that may be too short to resolve intermittency (and other low frequency contributions) contribute to a reduction in the measured turbulent flux by EC systems [*De Bruin et al.*, 1993; *Kaimal*

and Gaynor, 1991; *Kaimal and Finnigan*, 1994; *Leuning and Judd*, 1996; *Massman*, 2000; *Moncrieff et al.*, 1996].

In this study, we argue that these theoretical and sampling reasons necessitate exploring other micrometeorological methods that are sensitive to different set of assumptions and approximations to constrain or independently verify nighttime R_E estimates derived from EC.

An independent approach to estimating R_E is to utilize a functional relationship between aboveground mean CO_2 sources, $\overline{S}(t,z)$, or turbulent fluxes, $\overline{F}(t,z)$, and a relatively simpler quantity to measure such as mean CO_2 concentration profiles, $\overline{C}(t,z)$, within the canopy volume, where t is time, z is the height from the forest floor and the overbar denotes the temporal and spatial averaging operator. This framework is not new and dates back to *Woodwell and Dykeman* [1966]. The basic premise is that $\overline{S}(t,z)$ and $\overline{F}(t,z)$ can be related to $\overline{C}(t,z)$ using the temporally and horizontally averaged one-dimensional continuity equation for a planar homogeneous flow, given by

$$\frac{\partial \overline{C}(t,z)}{\partial t} = -\frac{\partial \overline{F}(t,z)}{\partial z} + \overline{S}(t,z) \tag{2-1}$$

which, upon vertical integration, yields

$$\frac{\partial}{\partial t}\left[\int_0^h \overline{C}(t,z)dz\right] = -\overline{F}(t,h) + R_E \tag{2-2}$$

where h is the mean canopy height, and R_E is defined as

$$R_E = \int_0^h \overline{S}(t, z)dz + \overline{F}(t,0) \qquad (2\text{-}3)$$

where $\overline{F}(t,0)$ is the forest floor efflux. In Equation (2-2), $\overline{F}(t, z)$ (which can be measured by EC) represents R_E when $\frac{\partial}{\partial t}\left[\int_0^h \overline{C}(t, z)dz\right] = 0$. A primitive approach to compute $\overline{S}(t, z)$ in Equation (2-1) can be formulated based on $\overline{C}(t, z)$ measurement using first order closure principles (or K-theory) by assuming that

$$\overline{F}(z) = -K_t \frac{\partial \overline{C}}{\partial z}$$

where K_t is the eddy-diffusivity.

Over the past 30 years, however, theoretical developments and many laboratory and field experiments have demonstrated that scalar and momentum fluxes within many canopies do not always obey K-Theory [*Corrsin*, 1974; *Deardorff*, 1972; 1978; *Denmead and Bradley*, 1985; *Finnigan*, 1985; *Raupach*, 1988; *Shaw*, 1977; *Sreenivasan et al.*, 1982; *Wilson*, 1989]. To alleviate K-Theory limitations, other theoretical and practical methods were developed without resorting to a local eddy diffusivity approximation [*Katul and Albertson*, 1999; *Raupach*, 1988; 1989a; b; *Siqueira and Katul*, 2002].

For example, *Lai et al.* [2002a] used the Localized Near Field (LNF) theory to relate $\overline{S}(t,z)$ to $\overline{C}(t,z)$ and demonstrated some success in estimating the two components of R_E (i.e. $\int_0^h \overline{S}(t,z)dz$ and $\overline{F}(t,0)$) over a one year period for near neutral and mildly stable flows. However, they pointed out a drawback of their method, titled Constrained Source Optimization (CSO), in that it was incapable of resolving the effects of local thermal stratification at a particular z within the canopy except through a Lagrangian integral time scale. Previous Lagrangian methods attempted to correct the Lagrangian time scale via a uniform multiplier derived from Monin-Obukhov similarity theory [*Hsieh et al.*, 2003; *Leuning*, 2000]. Several basic issues within Lagrangian models remain subject to debate outside the stability effects – most notable is that almost all Lagrangian models assume a vertically uniform time scale [*Lai et al.*, 2002a]. This assumption cannot be reconciled with a uniform mixing length scale inside the canopy [*Katul et al.*, 2004].

On the other hand, *Siqueira et al*.[2002; 2003], and *Siqueira and Katul* [2002] developed Eulerian closure models that are capable of accounting for local thermal stratification within the canopy volume if mean air temperature profile measurements are available.

This study combines the two approaches by revising the CSO method of *Lai et al.* [2002a] to include local thermal stratification within the canopy volume using higher order closure principles. We tested this modified CSO method over a three-year period at

a maturing southeastern pine forest using independent measurements of $\int_0^h \overline{S}(t,z)dz$ and $\overline{F}(t,0)$. The study period includes a mild drought (2001), a severe drought (2002), and a very wet year (2003) so that widest ranges of hydrologic and climatic conditions at this site are sampled. Improvements over R_E estimation from EC measurements using standard friction velocity u^* thresholds are discussed within the context of annual carbon balances.

2.2 Theory

2.2.1 Governing equations and turbulent transport

Rather than using K-theory, we consider the steady-state one-dimensional budget equation for the temporally and horizontally averaged carbon flux for high Reynolds and Peclet numbers flows (i.e. the molecular diffusion and conductive heat transfer are neglected), given by:

$$\frac{\partial \overline{F}}{\partial t} = 0 = -\overline{w'w'}\frac{\partial \overline{C}}{\partial z} + \frac{g}{\overline{T}}\overline{T'C'} - \overline{C'\frac{\partial p'}{\partial z}} - 2\varepsilon_C - \frac{\partial \overline{w'w'C'}}{\partial z} \qquad (2\text{-}4)$$

where w is the vertical velocity, $\overline{T}$ is the mean air temperature, p is the turbulent static pressure normalized by air density ρ, g is the gravitational acceleration constant, and ε_C is the molecular dissipation term. The symbol prime denotes the departures from averaging operator. To solve Equation (2-4) from measured mean CO_2 concentration profiles, further parameterizations are needed to quantify the vertical velocity variance $\overline{w'w'}$, the covariance between temperature and CO_2 turbulent fluctuations $\overline{T'C'}$ (i.e. the local atmospheric stability effects), the concentration-pressure interaction term $\overline{C'\frac{\partial p'}{\partial z}}$, the flux dissipation term ε_C, and the triple moment $\overline{w'w'C'}$. For $\overline{w'w'}$, we employ a second order closure model [*Katul and Albertson*, 1998; *Wilson and Shaw*, 1977] that solves for the mean velocity $\overline{u_i}$ and Reynolds stresses $\overline{u_i'u_j'}$, as discussed in Appendix A.

In Equation (2-4), the air temperature $\overline{T}$ and $\overline{T'C'}$ need to be determined. The corresponding steady-state one-dimensional temporal and horizontally averaged budget equations of the mean air temperature $\overline{T}(t, z)$ and the vertical kinematic turbulent flux of sensible heat $\overline{F_T}(t, z)$ can be derived as:

$$\frac{\partial \overline{T}(t,z)}{\partial t} = 0 = -\frac{\partial \overline{F_T}(t,z)}{\partial z} + \overline{S_T}(t,z) \tag{2-5}$$

$$\frac{\partial \overline{F_T}}{\partial t} = 0 = -\overline{w'w'}\frac{\partial \overline{T}}{\partial z} + \frac{g}{\overline{T}}\overline{T'T'} - \overline{T'\frac{\partial p'}{\partial z}} - 2\varepsilon_T - \frac{\partial \overline{w'w'T'}}{\partial z} \tag{2-6}$$

where ε_T is the molecular dissipation term for sensible heat, and $\overline{S_T}(t, z)$ is the corresponding heat source/sink term at level *z*.

Unlike the LNF approach utilized by *Lai et al.* [2002], the covariance $\overline{T'C'}$ and variance $\overline{T'T'}$ explicitly characterize the local (i.e. at given level *z* within the canopy) buoyant production/destruction effects. To compute the budgets of these two variables, additional steady-state one-dimensional prognostic equations are needed and given by *Meyers and Paw U* [1987]:

$$\frac{\partial \overline{T'C'}}{\partial t} = 0 = -\overline{F_T}\frac{\partial \overline{C}}{\partial z} - \overline{F}\frac{\partial \overline{T}}{\partial z} - 2\varepsilon_{TC} - \frac{\partial \overline{w'T'C'}}{\partial z} \tag{2-7}$$

and

$$\frac{\partial \overline{T'T'}}{\partial t} = 0 = -2\overline{F_T}\frac{\partial \overline{T}}{\partial z} - 2\varepsilon_{TT} - \frac{\partial \overline{w'T'T'}}{\partial z} \tag{2-8}$$

where ε_{TC} and ε_{TT} are the corresponding molecular dissipation terms.

In Equations (2-4), (2-6), (2-7), and (2-8), the pressure-gradient diffusion terms $\overline{T'\frac{\partial p'}{\partial z}}$, $\overline{C'\frac{\partial p'}{\partial z}}$, molecular dissipation terms ε_T, ε_C, ε_{TC}, ε_{TT}, and triple correlation terms $\overline{w'w'C'}$, $\overline{w'w'T'}$, $\overline{w'T'T'}$, $\overline{w'T'C'}$ are unknowns that need parameterizations. To solve these additional variables, standard second-order closure approximations are employed [*Donaldson*, 1973; *Katul and Albertson*, 1998; *Mellor*, 1973; *Mellor and Yamada*, 1974; *Meyers and Paw U*, 1986; 1987; *Wilson and Shaw*, 1977]. After utilizing these closure parameterizations, equations (2-4), (2-6), (2-7), and (2-8) can be rewritten as

$$\frac{\partial \overline{F}}{\partial t} = 0 = -\overline{w'w'}\frac{\partial \overline{C}}{\partial z} + \frac{g}{\overline{T}}\overline{T'C'} - \frac{Q}{3\lambda_2}\overline{F} - 2\frac{Q}{\lambda_3}\overline{F} - \frac{\partial}{\partial z}\left[-2Q\lambda_1\frac{\partial \overline{F}}{\partial z}\right] \tag{2-9}$$

$$\frac{\partial \overline{F_T}}{\partial t} = 0 = -\overline{w'w'}\frac{\partial \overline{T}}{\partial z} + \frac{g}{\overline{T}}\overline{T'T'} - \frac{Q}{3\lambda_2}\overline{F_T} - 2\frac{Q}{\lambda_3}\overline{F_T} - \frac{\partial}{\partial z}\left[-2Q\lambda_1\frac{\partial \overline{F_T}}{\partial z}\right] \tag{2-10}$$

$$\frac{\partial \overline{T'C'}}{\partial t} = 0 = -\overline{F_T}\frac{\partial \overline{C}}{\partial z} - \overline{F}\frac{\partial \overline{T}}{\partial z} - 2\frac{Q}{\lambda_3}\overline{T'C'} - \frac{\partial}{\partial z}\left[-Q\lambda_1\frac{\partial \overline{T'C'}}{\partial z}\right] \tag{2-11}$$

and

$$\frac{\partial \overline{T'T'}}{\partial t} = 0 = -2\overline{F_T}\frac{\partial \overline{T}}{\partial z} - 2\frac{Q}{\lambda_3}\overline{T'T'} - \frac{\partial}{\partial z}\left[-Q\lambda_1\frac{\partial \overline{T'T'}}{\partial z}\right] \tag{2-12}$$

where Q is the characteristic turbulent velocity (square root of the mean turbulent kinetic energy $\sqrt{\overline{u_i' u_i'}}$); λ_1, λ_2, λ_3 are length scales for the various terms as in *Wilson and Shaw* [1977] and *Katul and Albertson* [1998], and physically represent the characteristic length scales for the triple velocity correlations, the pressure-velocity gradient correlations, and the viscous dissipations, respectively. The parameterizations for these length scales are discussed in Appendix A.

Coupling Equations (2-1), (2-5), (2-9), (2-10), (2-11), and (2-12) with the set of equations (A1) for momentum in Appendix A (mainly to solve for Q and $\overline{w'w'}$) results in 6 equations with 8 unknowns ($\overline{T}$, $\overline{C}$, $\overline{S}$, $\overline{S_T}$, $\overline{F}$, $\overline{F_T}$, $\overline{T'C'}$, $\overline{T'T'}$). If $\overline{C}(t,z)$ and $\overline{T}(t,z)$ measurements are available, the system reduces to 6 equations with 6 unknowns thereby permitting one to numerically determine $\overline{S}(t,z)$, $\overline{F}(t,z)$ and, in turn, R_E.

2.2.2 Eulerian inverse model for heat

We used the Eulerian inverse model proposed by *Siqueira and Katul* [2002] to determine $\overline{S_T}(t,z)$ and $\overline{F_T}(t,z)$ from mean air temperature profile measurement. These variables are needed to solve Equations (2-5), (2-10), and (2-12). The boundary conditions for $\overline{F_T}(t,z)$ and $\overline{T'T'}$ are as proposed by *Meyers and Paw U* [1987] and are applied to Equation (2-10) and (2-12), respectively. After estimating $\overline{F_T}(t,z)$ and $\overline{T'T'}$

from measured temperature profiles, the heat source term $\overline{S_T}(t,z)$ can be directly determined from Equation (2-5).

The advantage of this inverse model is that the effects of atmospheric stability within the canopy volume can be explicitly considered. As discussed by *Siqueira and Katul* [2002], the impact of atmospheric stability is most pronounced in the scalar-temperature covariance equations ($\overline{T'C'}$ and $\overline{T'T'}$). These terms are now directly considered via their budget equations.

2.2.3 Source Calculation

We estimate the CO_2 turbulent fluxes and source terms differently from temperature for several reasons: (1) the aboveground plant area density is indicative of the relative "distribution" of aboveground respiring biomass thereby providing an additional constraint on $\overline{S}(t,z)$; (2) small errors in measured mean CO_2 concentration profile can dramatically impact the inference of $\overline{S}(t,z)$ from measured $\overline{C}(t,z)$ because of the absence of any redundancy [*Siqueira et al.*, 2003]; and (3) the temperature sensitivity of $\overline{S}(t,z)$, while not precisely known, can be constrained from leaf measurements.

The estimation of $\overline{S}(t,z)$ at each level from measured $C(t,z)$ can be re-formulated as an optimization problem [*Lai et al.*, 2002a; *Styles et al.*, 2002] in which the

relative strength of $\overline{S}(t,z)$ and its temperature sensitivity is *a priori* defined. Thus, rather than solving Equations (2-1), (2-5), (2-9), (2-10), (2-11), and (2-12) for $\overline{S}(t,z)$ forced by mean CO_2 concentration profile measurements, the system can be forced by an estimate of $\overline{S}(t,z)$ and predict the mean CO_2 concentration distribution, which can in turn be compared to measurements (e.g. every ½ hour).

To formulate a model for $\overline{S}(t,z)$, we note that the woody and leaf foliage tissue respiration have different physiological properties and hence their contribution to the total aboveground respiration is different. However, *Lai et al.* [2002a] argued that in a first order analysis, the respiration of woody tissue is less important than the contribution from foliage because the total woody surface area is less than the total leaf surface area (at least for this pine site), and the woody parts have smaller tissue-specific respiration rates than the foliage [*Hamilton et al.*, 2002]. With this simplification, *Lai et al.* [2002a] estimated the carbon source vertical distribution $\overline{S}(t,z)$ by assuming that the entire plant surface area was only foliage leading to:

$$\overline{S}(t,z) = a(t,z) \cdot R_d(t,z) \tag{2-13}$$

where $a(t,z)$ is the plant area density (PAD, in m^2 m^{-3}), and $R_d(t,z)$ is the dark respiration rate per unit plant tissue surface area (in μmol m^{-2} s^{-1}). $R_d(t,z)$ can be estimated from the *Farquhar et al.* [1980] model:

$$R_d(t,z) = \alpha(t) \cdot V_{c\max}(t,z) \tag{2-14}$$

where $\alpha(t)$ is a constant that needs to be determined at a given time *t*, and $V_{c\max}(t,z)$ is the maximum catalytic capacity of Rubisco per unit leaf area. The temperature dependency of $V_{c\max}(t,z)$ can be expressed as:

$$V_{c\max}(t,z) = V_{c\max,25}(t,z) \cdot \frac{\exp[a_1(\overline{T}(t,z) - 25)]}{1 + \exp[a_2(\overline{T}(t,z) - 41)]} \tag{2-15}$$

where a_1 and a_2 are the species-specific adjustment coefficients, which are obtained experimentally (e.g. via porometry) and $V_{c\max,25}(t,z)$ is the value of $V_{c\max}(t,z)$ at 25 ^{o}C [*Campbell and Norman*, 1998; *Collatz et al.*, 1991; *Farquhar et al.*, 1980]. From previous studies conducted at the site [*Ellsworth*, 1999; *Naumburg and Ellsworth*, 2000; *Naumburg et al.*, 2001], $V_{c\max,\ 25}$, a_1 and a_2 are 59 µmol m^{-2} s^{-1}, 0.051 and 0.205, respectively for the upper canopy pine foliage, and are 30 µmol m^{-2} s^{-1}, 0.088 and 0.290, respectively for the sub-canopy broadleaved plants [*Lai et al.*, 2002a]. With the exception of the product $\{\alpha(t) \cdot V_{c\max,25}(t,z)\}$, these physiological parameters were considered temporally constant for the model calculations.

2.2.4 Modified constrained source optimization

With this formulation for $\overline{S}(t,z)$, the problem reduces to a 2-parameter estimation ($\{\alpha(t) \cdot V_{c\max,25}(t,z)\}$and $\overline{F}(t,0)$) from the measured nighttime CO_2 concentration profiles $\overline{C}(t,z)$. Thus the question is: what is the optimum combination of

$\{\alpha(t)\cdot V_{c\max,25}(t,z)\}$ and $\overline{F}(t,0)$ so that that the solution to Equations (2-1), (2-5), (2-9), (2-10), (2-11), and (2-12) best matches the measured $\overline{C}(t,z)$? Because only two parameters describe the entire source and they can be constrained to vary within a limited range, a global search for the optimum $\{\alpha(t)\cdot V_{c\max,25}(t,z)\}$ and $\overline{F}(t,0)$ can be conducted until the root mean square error (RMSE) between the calculated and measured CO_2 concentrations at different levels is minimized on a 30-minute time scale. For example, if foliage respiration is the only dominant aboveground respiration component, we anticipate $\alpha(t)$ to be near 0.015, which is a commonly used value in many studies [*Collatz et al.*, 1991; *Farquhar et al.*, 1980; *Lai et al.*, 2002a]. Furthermore, nighttime forest floor respiration should not exceed the maximum daytime photosynthesis in magnitude. An upper limit on the maximum daytime canopy photosynthesis $A_{n,c}$ can be determined from daytime water vapor flux measurements (i.e. latent heat flux) using

$$A_{n,c} \approx \frac{LE}{VPD}\left(1-\frac{C_i}{C_a}\right)C_a$$

where *LE* is determined as the maximum latent heat flux measured for each day throughout the experiment, *VPD* is the mean daytime vapor pressure deficit and C_i / C_a is the ratio of intercellular to ambient atmospheric CO_2 concentration, estimated at 0.66 for sunlit foliage [*Katul et al.*, 2000]. This leads to a maximum conservative estimate of mean photosynthesis and sets an upper limit to a priori constrain nighttime respiration. Because of these constraints and its Eulerian formulation to account for thermal

stratification within the canopy, we refer to this method as the Eulerian constrained source optimization (CSO_E).

2.3. Study site and measurements

2.3.1 Study site

The measurements were made at the Blackwood Division of the Duke Forest near Durham in North Carolina (site location: 35°58'N, 79°05'W, 163 m above sea level) as part of the AmeriFlux long-term CO_2 flux monitoring initiative [*Baldocchi et al.*, 2001]. This study site is a uniformly planted loblolly pine (*Pinus taeda L.*) forest (planted in 1983 at 2 m × 2.4 m spacing) that extends 300 to 600 m in the east-west direction and 1000 m in the south-north direction. The subcanopy also contains about 40 woody species, of which *Liquidambar styraciflua L.*, *Acer rubrum L.*, *Ulmus alata Michx.*, and *Cornus florida L.* are the most prevalent [*Palmroth et al.*, 2005]. The local topographic variations are small (slope < 5%) enough to ignore the effect of the complex terrain on the flow statistics [*Siqueira et al.*, 2002]. The study period extends from year 2001 to 2003. Table 1 describes the variations in ecological, hydrologic, and climatic conditions for these three years at this study site.

Table 1: The overall variability ranges in ecophysiological, hydrological, and climatic factors from 2001 to 2003 at the Duke Forest pine site. The soil moisture content, soil temperature, and the air temperature are half-hourly averages from the profile measurement.

Year	2001	2002	2003
Average canopy height, m	17.0	17.5	18.0
Total PAI range, m^2m^{-2}	2.20~6.53	2.22~5.16	2.09~4.16[+]
Pine PAI range, m^2m^{-2}	1.85~3.26	1.91~2.96	1.74~3.23[+]
Growing season[*] precipitation, mm	529.2	371.4	789.8
Soil moisture content (θ) range, m^3m^{-3}	0.13~0.54 (0.13~0.51)[**]	0.13~0.47 (0.13~0.37)	0.20~0.54 (0.20~0.54)
Soil temperature (T_s) range, ^oC	3.1~23.5 (8.8~23.5)	5.4~23.8 (9.6~23.8)	3.7~23.6 (9.0~23.6)
Air temperature (T_a) range, ^oC	-11.2~35.5 (-2.8~35.5)	-10.7~38.9 (-2.6~38.9)	-12.2~35.2 (0.3~35.2)

[+] In December of 2002, an ice storm reduced the PAI of the pine stand.
[*]The growing season is from April 1st to Sep 30th (Julian day: 152 to 273)
[**]The bracketed numbers represents the range during the growing season.

2.3.2 Eddy covariance flux measurements

The momentum components, Reynolds stresses, sensible heat, latent heat and CO_2 fluxes above the canopy were measured by a conventional eddy-covariance system comprising of a Li-Cor 7500 CO_2/H_2O open-path infrared gas analyzer (Li-Cor Inc., Lincoln, NE, USA) and a tri-axial sonic anemometer (CSAT3, Campbell Scientific Inc., Logan, UT, USA). Both the gas analyzer and the tri-axial sonic anemometer were positioned at z = 20.23 m, which is above the canopy top (from 17 to 18 m during the study period).

The flux measurements were sampled using a Campbell Scientific 23X data micrologger with all digitized signals transferred to a portable computer via an optically isolated RS232 interface for future processing. All the variables in this eddy-covariance measuring system were sampled at 10 Hz and averaged every 30 minutes. The correction for the effects of air density on flux measurements after *Webb et al.* [1980] was applied.

2.3.3 Mean CO_2 concentration and air temperature profiles within the canopy

A multi-layer concentration monitoring system was installed to sample the mean water vapor pressure and CO_2 concentration at 10 different levels throughout the canopy volume (z = 0.1 m, 0.75 m, 1.5 m, 3.5 m, 5.5 m, 7.5 m, 9.5 m, 11.5 m, 13.5 m and 15.5 m) using a Li-Cor 6262 CO_2/H_2O infrared gas analyzer. This profiling system includes a

multi-port gas-sampling manifold to sample each level for 1 minute (45 second sampling and 15 second purging) with a repeating cycle of 10 minutes for the 10 sampled levels. Data was averaged every 30 minutes. In addition, a mean air temperature profiling system was installed to measure the mean air temperature every 30 minutes at eight different levels (z = 1.5 m, 3.5 m, 5.5 m, 7.5 m, 9.5 m, 11.5 m, 13.5 m, and 15.5 m) throughout the canopy volume using copper-constantan shielded thermocouple sensors (see *Siqueira and Katul* [2002] for details).

2.3.4 Volumetric soil moisture content and soil temperature measurement

Long-term volumetric soil moisture content θ (m^3 m^{-3}) was sampled using 4 Campbell Scientific CS615 reflectometers placed in the top 30 cm of the mineral soil, and the soil temperature was measured at 10-12 cm via nonlinear thermistor probes (M 841/S1, Siemens, Germany). All signals were sampled every 30 seconds using a CR23X data logger and averaged every 30 minutes. The mean soil moisture content was obtained by averaging over all 4 CS615 probes.

2.3.5 Forest floor CO_2 efflux measurements

The forest floor CO_2 efflux was measured with the automated carbon efflux system (ACES, US Patent 6692970) developed by the USDA Forest Service, Southern Research Station Laboratory in Research Triangle Park, NC [*Butnor et al.*, 2003; *Butnor and Johnsen*, 2004; *Palmroth et al.*, 2005]. The ACES is an open system with an infrared gas analyzer connected to several soil chambers equipped with soil and air thermocouples, pressure equilibration ports, and reflective covers. The ACES system was installed at the site in February of 2001. The details of the ACES configuration, quality checks, and spatial sampling area, are described in *Palmroth et al*. [2005].

To quantify the variation of forest floor efflux with varying volumetric soil moisture content θ ($m^3\ m^{-3}$) and soil temperature T_s (^oC), *Palmroth et al*. [2005] derived a equation modified from *Fang and Moncrieff* [1999], of the form

$$F(t,0) = R_b e^{aT_s}\left[1 - e^{(-b\theta + c)}\right] \qquad (2\text{-}16)$$

where R_b is the base respiration ($\mu mol\ m^{-2}\ s^{-1}$), which is defined as the intercept at 0 ^oC, a is the temperature sensitivity ($Q_{10} = e^{a\times 10}$) when soil moisture content is not limiting, and the constants b and c are fitted parameters of the soil moisture reduction function. All the constants in Equation (2-16) were determined via nonlinear regression methods using the ACES measured respiration, the mean 10-12 cm soil temperature, and the CS615 soil moisture and are summarized in Table 2 [*Palmroth et al.*, 2005]. Equation (2-

16) constitutes the spatially averaged chamber measurements of forest floor efflux and will be used to independently test the CSO_E estimates of $\overline{F}(t,0)$.

2.3.6 Plant area index and plant area density

The plant area index (PAI, m^2 m^{-2}) is routinely measured several times a year using a pair of Li-Cor LAI 2000 optical sensors. The plant area density (PAD, m^2 m^{-3}) measurements were conducted at 1 m intervals from the bottom to the top of canopy. Calibration of PAI was done using allometric relationships derived from different individual species within the canopy volume [*Lai et al.*, 2000b; *Pataki et al.*, 1998; *Schafer et al.*, 2003].

LAI-2000 measurements, coupled with the abovementioned allometric functions, were used to estimate the vertical distribution of PAD at daily time steps [*Schafer et al.*, 2003]. The range of total PAI and pine PAI in 2001, 2002, and 2003 are given in Table 1.

Table 2: The regression parameters for the chamber-based forest floor CO_2 efflux equation $F(t,0) = R_b e^{aT_s}\left[1 - e^{(-b\theta+c)}\right]$ given in *Palmroth et al*. [2005] for 2001 to 2003 at the Duke Forest site. The 2003 data is added to the data published in *Palmroth et al.* [2005], which covered 2001-2002.

Year	Day	R_b	A	b	c
2001	001~179	0.570	0.123	25.228	2.301
	180~365	0.648	0.118	27.120	2.882
2002	001~088	0.648	0.118	27.120	2.882
	089~238	0.908	0.092	27.952	3.099
	239~365	0.753	0.106	32.302	3.987
2003	001~365	0.814	0.104	32.302	3.987

2.4. Results and discussion:

To address the study objective, the results and discussion are organized as follows:

(1) We use the measured $\overline{C}(t, z)$ to estimate the nighttime storage fluxes in Equation (2-1) and compare their magnitude to the EC measured nighttime NEE noting that almost all sites that utilize a large u^* threshold for the EC data neglect storage fluxes in Equation (2-1);

(2) We use the CSO_E model to individually estimate the two components of nighttime ecosystem respiration and compare them to the results from chamber measurements and to independent estimates of aboveground respiration;

(3) We discuss the sensitivity of the modeled R_E to local thermal stratification by comparing model calculations with and without the consideration of buoyant production/destruction terms for thermally-stratified condition and neutral flows condition, respectively.

(4) Finally, we discuss the CSO_E respiration components within the context of the annual carbon balance at the site, and explore other methods to constrain annual nighttime ecosystem respiration (e.g. intercept of the NEE light response curve).

To ensure that nighttime conditions are not "contaminated" by photosynthesis, we define nighttime hereafter from 8:00 P.M. to 5:00 A.M. throughout the 3-year study period.

2.4.1 Storage flux

Gap-filled nighttime EC measured flux (hereafter referred to as $\overline{F_{EC}}$) is often derived from high u^* runs, in which the canopy is likely to be ventilated (except for a region close to the ground). Under such conditions, it is reasonable to assume that $\overline{F_{st}} = \left| \frac{\partial}{\partial t} \left[\int_0^h \overline{C}(t,z) dz \right] \right| << \left| \overline{F_{EC}} \right|$. Hence, when determining time series of R_E, $\overline{F_{st}}$ is often neglected when using gap-filled $\overline{F_{EC}}$ collected for high u^*. On a daily basis, the mean value of $\overline{F_{st}}$ is often close to zero, but can be significantly large during sunrise, sunset and during nighttime conditions of low u^* [*Lai et al.*, 2000a; *Lai et al.*, 2002a].

Because $\overline{C}(t,z)$ is the key determinant of $\overline{F_{st}}$, we show the two-month ensemble averaged $\overline{C}(t,z)$ (in ppm) measured at different times of the day during 2003 for illustration (Figure 1). It is clear that the mean CO_2 concentration is unsteady during nighttime conditions and this buildup trend is even stronger during high leaf area season (i.e. May to October). This finding is not surprising because the canopy respires more during the summer months, due to both higher leaf mass and higher temperature, and because the turbulence is dampened during the high leaf area season (see Appendix A).

More subtle is the observation that the temporal variation of the measured ensemble averaged u^* (red solid line) is also different across seasons with lower values measured in the summer. This finding is important when using a global u^* threshold for gap filling $\overline{F_{EC}}$ measurements because such a threshold may disproportionately eliminate summer-time runs.

To quantify the effect of nighttime variations in u^* on EC and storage flux, we compared $\overline{F_{st}}/\overline{F_{EC}}$ at different u^* thresholds (Figure 2, showing 14-day averages during nighttime from the entire 3-year study period). The value of $\overline{F_{st}}$ is derived from the numerical integration of the measured mean CO_2 concentration profile every 30 minutes run and ensemble averaged every 14 days.

Figure 2 indicates that the ensemble averaged $\overline{F_{st}}/\overline{F_{EC}}$ is almost always greater than 0.27 at this experimental site. The mean $\overline{F_{st}}/\overline{F_{EC}}$ ratio increases from 0.27 to about 0.44 when u^* drops from 0.45 to 0.15 m s^{-1}, but significantly increases when u^* drops below 0.15 m s^{-1}. Note also that measured $u^* < 0.15$ m s^{-1} is a common occurrence for summertime runs, especially in 2003 (Figure 1). Thus, this analysis indicates that R_E may be larger than $\overline{F_{EC}}$ by at least 27% at this experimental site if storage is neglected. However, we emphasize that determining $\overline{F_{st}}$ from a single tower is subject to several theoretical and practical limitations, and the need to ensemble average concentration data (e.g. 14-day) beyond averaging random noise are further discussed in Appendix B.

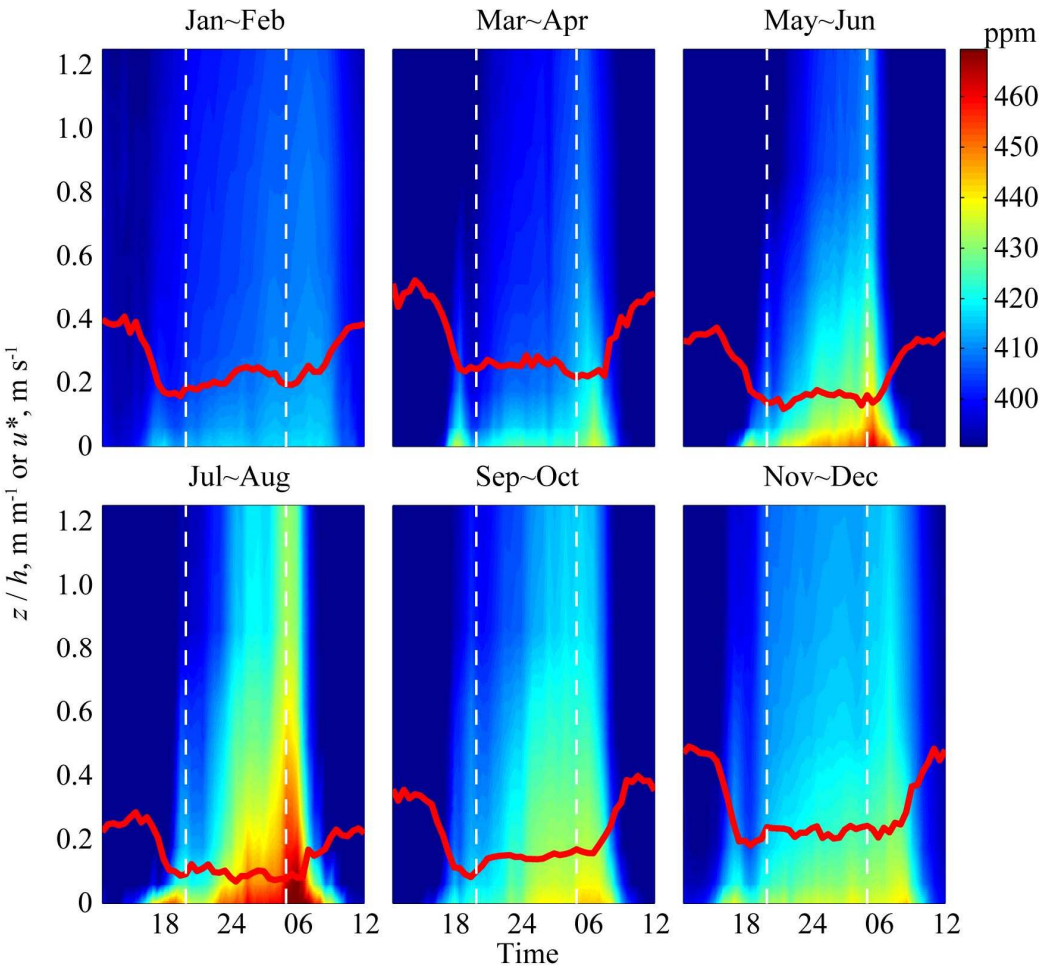

Figure 1: Normalized depth/time of day variations of nighttime (8:00 P.M. to 5:00 A.M., bounded by two dashed lines in each subplot) ensemble averaged CO2 concentration profiles (ppm) for two-month periods in 2003. The two-month ensemble averaged friction velocity

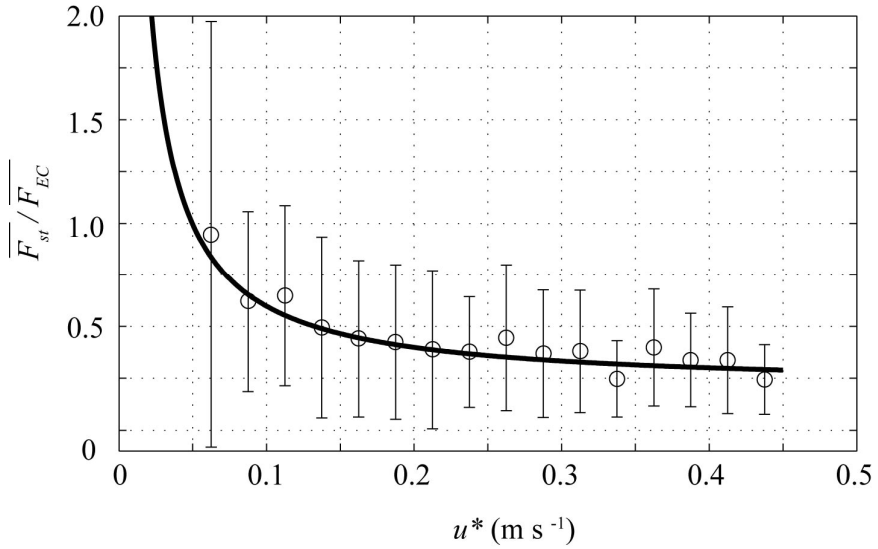

Figure 2: The ensemble variation of the ratio of storage flux to EC measured flux ($\overline{F_{st}}/\overline{F_{EC}}$) with friction velocity u^* during nighttime runs (8:00 P.M. to 5:00 A.M.) for the entire measurement period (2001-2003). The flux ratio $\overline{F_{st}}/\overline{F_{EC}}$ is expressed as 14-day ensemble averages, and vertical bars represent one standard deviation. The solid line is the regression curve.

2.4.2 Optimized forest floor carbon efflux

The optimized $\{\alpha(t)\cdot V_{c\max,25}(t,z)\}$ and $\overline{F}(t,0)$ were determined over a 14-day ensemble average period based on the root-mean squared error ($RMSE \le 10\,ppm$) of 30-minute comparisons between CSO_E modeled and measured $\overline{C}(t,z)$. The available numbers of 30 minute-runs used in the model calculations for 2001 to 2003 are 396, 432, and 450 runs, respectively. The resulting CSO_E optimized $\overline{F}(t,0)$ is then regressed with measured 10-12 cm soil temperature T_s (Figure 3(a)). The relationship is expressed as

$$F(t,0) = A\cdot\exp\left(B\cdot T_s(t)\right) \tag{2-17}$$

where *A* and *B* are regression parameters (Figure 3(a); with an individual regression fit for each year) presented in Table 3. From Table 3, it is clear that these fitted parameters change from year to year. For example, forest floor carbon efflux values modeled with CSO_E for the severe drought year of 2002 were different than the other two years, especially when soil temperature was high (Figure 3a). Calculated from parameter B, the Q_{10} values for 2001, 2002 and 2003 are 2.34, 1.82 and 2.32, respectively, consistent with the values reported by *Palmroth et al.* [2005]. Using a Student's t-test, the reduction in Q_{10} for 2002 is statistically significant at the 95% confidence level.

To investigate whether the variability in parameters are driven by soil moisture effects, we fit Equation (2-16) [*Palmroth et al.*, 2005] to the entire 3 year record. We separate the model results into two different θ regions ($\theta \ge 0.2\ m^3\ m^{-3}$ and $\theta < 0.2\ m^3\ m^{-3}$

^{3}), where the value of $\theta < 0.2$ m^3 m^{-3} is the critical point at which θ significantly affects $\overline{F}(t,0)$ [*Palmroth et al.*, 2005]. For the non-soil moisture-limiting region, it is clear from Figure 3(b) that one temperature curve suffices to explain the entire optimized forest floor flux variability (hereafter, the estimate of $\overline{F}(t,0)$ from this curve is referred to as F_{Ts}). For the soil-moisture limiting region, we plot relative $\overline{F}(t,0)$ (expressed as $\overline{F}(t,0)/F_{Ts}$) against θ and show that resulting reduction is consistent with the chamber data. When combining these two findings, a unique multivariate curve for the entire three year record can be derived (Table 3).

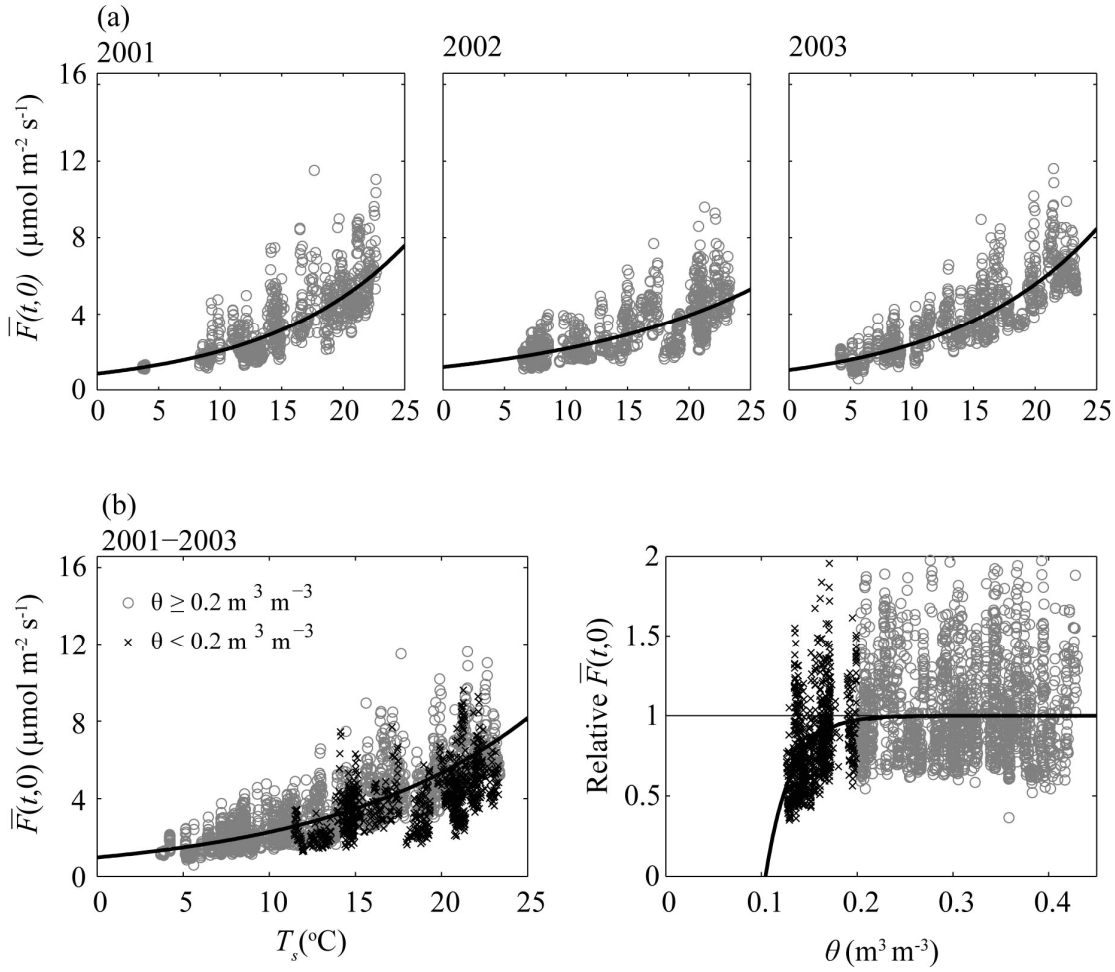

Figure 3: (a) The variation of the CSO_E optimized forest floor efflux (open circle) with soil temperature for each of the three years. The solid lines are obtained by regressing soil temperature to the CSO_E optimized values of $\overline{F}(t,0)$. They demonstrate the non-stationarity in forest floor respiration-soil temperature curve parameters. (b) the soil temperature effect (left panel) for $\theta \geq 0.2\,\mathrm{m}^3\,\mathrm{m}^{-3}$ and soil moisture reduction curve (solid line on the right panel) for all three years. All equations and regression statistics are shown in Table 3.

Table 3: The regression curves for (in μmol m-2 s-1) shown in Figure 3. The coefficient of determination R2 and the root-mean squared error RMSE (in μmol m-2 s-1) are also shown. For reference, we also show the equivalent Q10 values.

Ts-dependent only				
Year	Fitted curve	R^2	*RMSE*	Q_{10}
2001	$F(t,0) = 0.846 \cdot \exp(0.085 \cdot T_s)$	0.66	1.08	2.34
2002	$F(t,0) = 1.191 \cdot \exp(0.060 \cdot T_s)$	0.55	1.22	1.82
2003	$F(t,0) = 1.036 \cdot \exp(0.084 \cdot T_s)$	0.76	1.03	2.32
Unique fitted curve couple with θ-correction				
2001-2003	$F(t,0) = F_{Ts} \cdot [1 - \exp(-37.829\theta + 3.948)]$	0.52	1.12	2.09
T_s-dependence	$F_{Ts} = 0.974 \cdot \exp(0.085 \cdot T_s)$	0.73	1.05	2.34
θ-correction	$1 - \exp(-37.829\theta + 3.948)$	0.15	N/A	N/A

2.4.3 Optimized aboveground C source:

There are no explicit measurements for the aboveground respiration during this period and hence the evaluation of the CSO_E model is not direct. Nonetheless, we can assess whether the CSO_E model is sensitive to well-documented variability in $V_{c\max,25}(t,z)$. Towards this end, we compare the seasonal dynamics in $\{0.015 \cdot V_{c\max,25}(t,z)\}$ as derived from porometry (*Ellsworth* [2000]) with the optimized $\{\alpha \cdot V_{c\max,25}(t,z)\}$ from the CSO_E.

If we set $\alpha = 0.015$ and compute $V_{c\max,25}(t,z)$ via Equations (2-14) and (2-15), the normalized seasonal variation of $V_{c\max,25}$ (expressed as $V_{c\max,25} / \text{mean}V_{c\max,25}$) derived from the CSO_E model calculations can be compared to the porometry data shown in Figure 4. The comparison with the porometry data cannot be direct because the published porometry measurements in *Ellsworth* [2000] were conducted from 1998 to 2000. Nonetheless, the qualitative agreement in Figure 4 suggests that the mean CO_2 concentration profile data, when combined with the CSO_E model, can resolve seasonal shifts in aboveground physiological properties due to leaf acclimation. This agreement also lends indirect support to the CSO_E above ground respiration estimates.

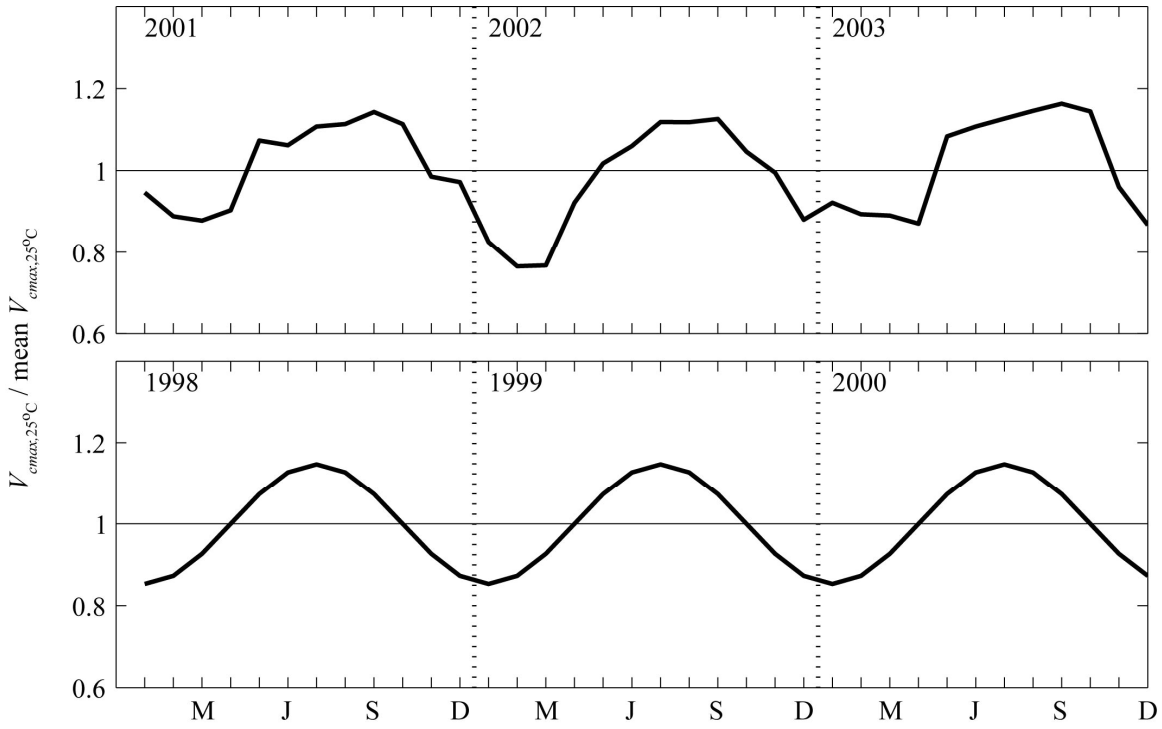

Figure 4: Relative variation of optimized $V_{c\max,25}$ from CSO_E model from 2001 to 2003 (top panel) and the reported relative changes in $V_{c\max,25}$ from 1998-2000 after *Ellsworth* [2000] (bottom panel).

Table 4: Annual carbon budgets (gC m-2 yr-1) at the Duke Forest pine site from 2001 to 2003.

Carbon budget components	2001	2002	2003	Notes
Annual ecosystem respiration, R_E	1767	1623	2022	$R_E = F(t,0) + R_{AB}$
Forest floor carbon efflux, $F(t, 0)$	1224	1127	1473	CSO_E model
	(1328)	(1230)	(1599)	ACES chamber exp.
	(1344)	(1180)	(1565)	ACES model Eq. (16)
Aboveground respiration, R_{AB}	543	498	549	CSO_E model = $\int_0^h S(t,z)\,dz$
(Dark respiration)	(391)	(387)	(412)	$\int_0^h [a(t,z)\cdot 0.015\cdot V_{c\max}(t,z)]dz$
Total root respiration, R_R	673	620	810	$R_R = 0.55\cdot F(t,0)^*$
Autotrophic respiration, R_A	1216	1118	1359	$R_A = R_R + R_{AB}$
Heterotrophic Respiration, R_H	551	507	663	$R_H = 0.45\cdot F(t,0)^*$
Modeled GPP	2211	2033	2471	$\frac{NPP}{GPP} = 1 - \left\|\frac{R_A}{GPP}\right\| \approx 0.45^{**}$
Modeled NPP	995	915	1112	
Nighttime values				
R_E from CSO_E	837	791	987	
R_E from $F(t,h)$-*PPFD* curve	987	796	1033	
Fst	197	203	227	
F_{EC}	(616)	(691)	(759)	

2.4.4 Ecosystem Respiration

From the optimized $\{\alpha \cdot V_{c\max,25}(t,z)\}$ and $\overline{F}(t,0)$ described in the previous two sections, we proceed to estimate the ecosystem respiration. Figure 5 shows separately the modeled monthly variation of $\overline{F}(t,0)$, aboveground respiration, and R_E (in gC m^{-2} $month^{-1}$) from 2001 to 2003, along with measured monthly averaged air and soil temperature. Based on the CSO_E calculations, the contribution of the forest floor efflux is larger than the contribution of the aboveground biomass to total ecosystem respiration. In the winter, modeled $\overline{F}(t,0)$ can be as much as 85% of modeled R_E, while in the summer, it drops to about 70%. This finding is consistent with a recent study at the site based on stable isotope measurements and analysis [*Mortazavi et al.*, 2005].

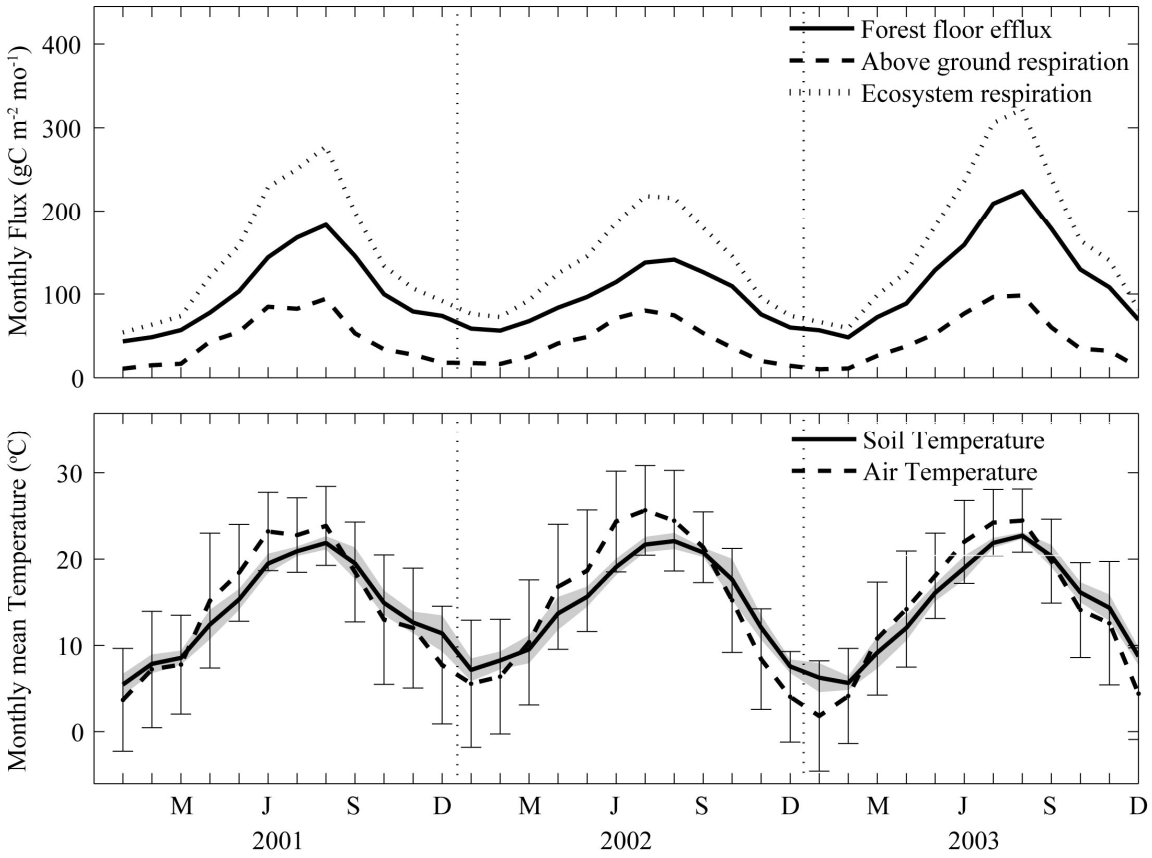

Figure 5: CSO_E model results for monthly forest floor efflux, aboveground respiration, and ecosystem respiration (upper panel), and monthly mean air temperature and soil temperature (lower panel) from 2001 to 2003. The error bars and shaded area in the lower panel represent the standard deviation of air temperature and soil temperature respectively.

2.4.5 CSO_E Model Testing

To check the performance of the CSO_E model, we compare the monthly modeled forest floor carbon efflux with monthly $\overline{F}(t,0)$ determined from chambers [*Palmroth et al.*, 2005] (Figure 6). When comparing the monthly data, the largest divergence between the chamber estimates and the CSO_E model is during the severe drought in 2002. It appears that the CSO_E model predictions of $\overline{F}(t,0)$ are lower than estimates by the chambers suggesting over-sensitivity to drought. Furthermore, the CSO_E model under-predicts the chamber-based high respiration rate. Despite these differences, there is a good agreement between these two independent estimates on annual time scales (Table 4). These differences result in CSO_E modeled efflux that is about 111 gC m^{-2} $year^{-1}$ smaller than the chamber-based estimates. The difference might be attributed to several factors that are difficult to de-convolve: 1) the footprints of the chambers and CSO_E model are very different, and it is possible that the average of the patches sampled with the chambers consistently respired more than the area sampled by the mean concentration used in the CSO_E; and 2) the CSO_E modeled turbulent diffusivity near the ground (highly sensitive to how $\overline{w'w'}$ and Q decay near the forest floor) may be consistently low (due to both model formulation of the mixing length and plant area distribution near the ground) thereby biasing the CSO_E model inversion to lower values. Regardless of the reason, relative to the annual rate of forest floor efflux (>1000 gC m^{-2}), the difference in annual estimates based on these very different approaches is surprisingly small (about 10%),

especially considering the large differences (23%) obtained using different approaches [*Law et al.*, 1999a].

Finally, we compared $\overline{F_{EC}}$ with CSO_E modeled $\overline{F}(t,z)$ for different u^* thresholds and for the entire 3-year period (Figure 7). $\overline{F_{EC}}$ is consistently lower than modeled $\overline{F}(t,z)$ by almost 30% for small u^* and almost 8% for high u^*. Note that this comparison is a direct flux comparison between measured and modeled fluxes above the canopy and not a respiration comparison, which is dependent on storage flux estimates. To explore whether high frequency corrections to $\overline{F_{EC}}$ (not applied to the EC data here) alone may explain this underestimation, we used the analytical model by *Massman* [2000]. For the model calculations (also shown as dashed line in Figure 7) we employed the following configuration: the CSAT3 sonic anemometer has collocated vertical and horizontal paths of length 0.15 m; the sampling period is 30 minutes; the sampling frequency is 10 Hz; the measurement height above the zero plane displacement is 9.95 m; no anti noise band pass filtering or de-trending is used; block-averaging is conducted every 30 minutes; planar separation distance between the CSAT3 and the LI7500 gas analyzer is 0.15 m with no vertical separation; and the LI7500 sensor path length is 0.20 m with a time constant determined by assuming line-averaging only. The ensemble ratio of corrected to uncorrected fluxes predicted by this analytical model only explains about half of the differences of $\overline{F_{EC}}$ (i.e. 15%-4% with increasing u^*).

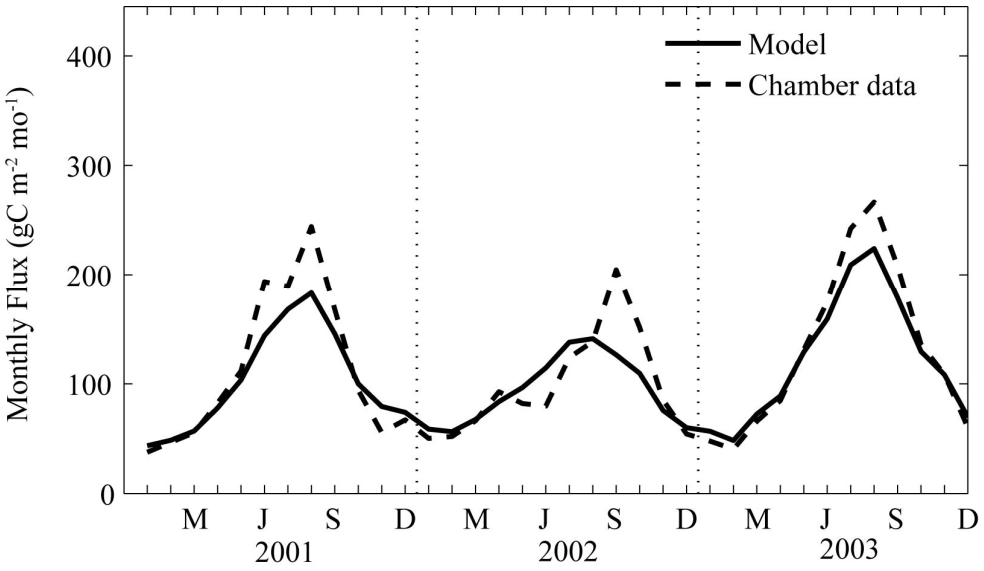

Figure 6: Comparisons between the monthly forest floor effluxes from CSOE and the chamber data generated from the regression equation in Palmroth et al. [2005] for all three years.

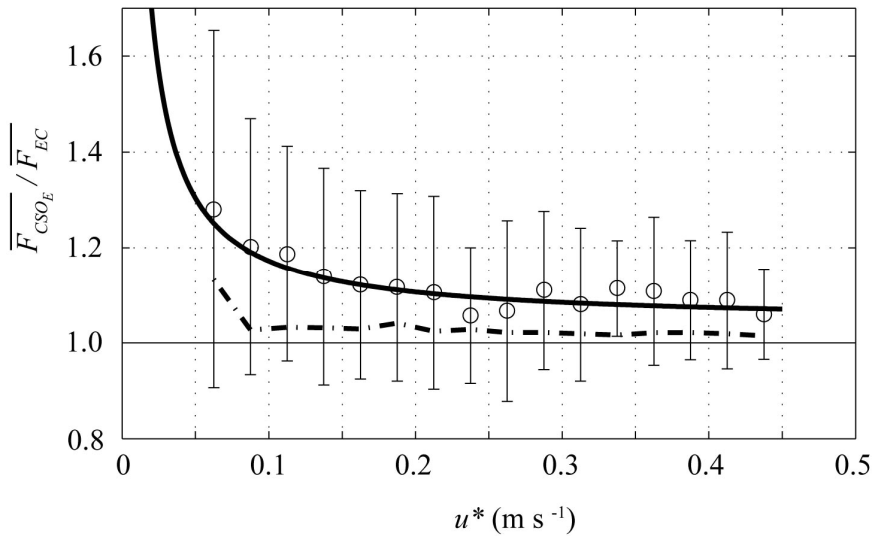

Figure 7: The ratio of modeled CSOE flux above the canopy ( ) to that from eddy-covariance measurements ( ) in relation to the threshold employed for data collected during the 3-year period. The circles are ensemble-averaged and the vertical lines are one standard deviation around the average. The dot-dashed line is the high frequency spectral corrections to the predicted by the Massman [2000] model.

2.4.6 Nighttime net ecosystem respiration comparison: effects of atmospheric stability

In Figure 8, we compare the CSO_E model calculations assuming neutral atmospheric stability conditions with the density-stratified CSO_E model results for R_E. By setting $g = 0$ (i.e. the contribution from terms $\overline{T'C'}$ and $\overline{T'T'}$ = 0) and not correcting the upper boundary conditions for atmospheric stability guarantee neutral stratification within the general CSO_E model. We found that by ignoring local atmospheric stability, the modeled R_E is about 10% lower for the entire study period. For reference, Figure 8 also shows the nighttime ecosystem respiration comparison between the CSO_E model (solid lines) and $\overline{F_{EC}}$ (dot-dashed line) and $\overline{F_{EC}} + \overline{F_{st}}$ (dotted line). This comparison demonstrates that resolving the storage flux and correcting for local thermal stratification tends to increase R_E over its eddy-covariance estimate (without storage). Interestingly, correcting for monthly storage fluxes may be comparable to correcting for the stability effects (~20 gC m^{-2} $month^{-1}$ in summer of 2003).

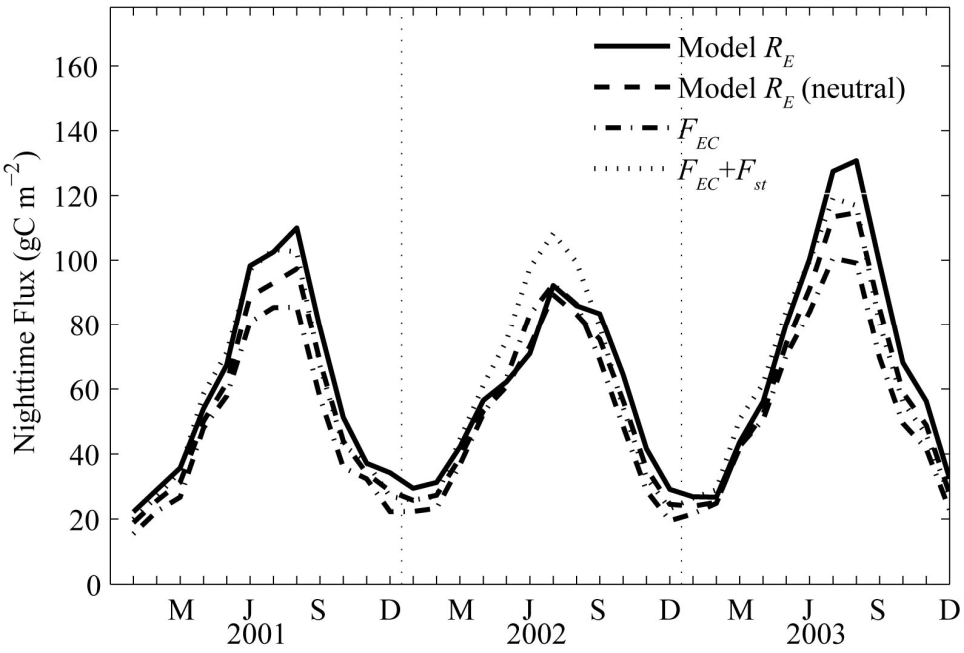

Figure 8: Comparison between nighttime (monthly ensemble average from 8:00 P.M. to 5:00 A.M.) ecosystem respirations obtained from eddy-covariance measurements and CSO_E model results with and without the consideration of atmospheric stability

2.4.7 Ecosystem carbon budget at the Duke Forest Pine Site

From the CSO_E model results, we summarize the carbon budget for the site from 2001 to 2003 (Table 4). Summing up the modeled forest floor carbon efflux and modeled aboveground respiration leads to total ecosystem respiration of 1767, 1623, and 2022 gC m^{-2}, respectively, for 2001, 2002, and 2003. These values are consistent with independent estimates made earlier at the site (see Table 4). To further assess whether the modeled R_E is also consistent with the expected overall carbon balance at the site, we estimated root-respiration from $R_R = 0.55 \cdot \overline{F}(t,0)$ [*Andrews et al.*, 1999] using CSO_E modeled $\overline{F}(t,0)$. The autotrophic respiration R_A can be determined from the R_R and the CSO_E modeled aboveground respiration (R_{AB}). To determine gross primary production (GPP) and net primary production (NPP) from R_A, we used the following relationship:

$$\frac{NPP}{GPP} = 1 - \left| \frac{R_A}{GPP} \right|$$

Lai et al. [2002b] quantified the NPP/GPP ratio using aboveground biomass for a young (6 year old) pine stand. In this study, we used the averaged aboveground biomass of 5128 gC m^{-2} estimated by *Hamilton et al.* [2002] to determine the NPP/GPP ratio as about 0.45 for this study site. Using this estimate, the modeled GPP computed from modeled R_A varied from 2033 to 2471 gC m^{-2} for these three years. This range is comparable to other estimates [*Hamilton et al.*, 2002; *Lai et al.*, 2002a; *Schafer et al.*, 2003] conducted earlier at the site (2371 to 2486 gC m^{-2} from 1998 to 2000). As for NPP, the modeled values here ranged from 915 to 1112 gC m^{-2} during the 3-year study period.

This range is higher by about 200 gC m^{-2} when compared to biometric estimates [*Hamilton et al.*, 2002; *Schafer et al.*, 2003] conducted for an earlier period from 1998 to 2000 (705 to 1060 gC m^{-2}).

Up to this point, we showed how the CSO_E model is used to constrain annual nighttime respiration from CO_2 concentration data. Here, we compare these CSO_E results to other proposed methods that attempt to constrain nighttime respiration. In particular, we used the so-called light response curve method [*Lee et al.*, 1999], which is based on determining the intercept of the $\overline{F}(t,h)$ and photosynthetically active photon flux density (*PPFD*) [*Clark et al.*, 1999; *Lai et al.*, 2002a; *Law et al.*, 1999a]. The curve is expressed as:

$$\overline{F}(t,h) = \frac{\omega_p \cdot PPFD \cdot F_{sat}}{\omega_p \cdot PPFD + F_{sat}} - R_o$$

where ω_p is the mean apparent quantum yield, F_{sat} is the net CO_2 flux at light saturation, and intercept R_o is the mean net CO_2 flux when *PPFD* = 0. The R_o can provide estimates of mean nighttime ecosystem respiration independent of the nocturnal CO_2 concentration or $\overline{F}(t,h)$ data.

Figure 9 shows the light response curves for 2001 to 2003, respectively. The lower daytime fluxes in 2002 are due to the severe drought event. The R_o estimated for each year resulted in nighttime ecosystem respiration of 987, 796, and 1033 gC m^{-2} yr^{-1},

which are slightly higher than the estimates from the CSO_E model (higher by about 0.5% to 16%).

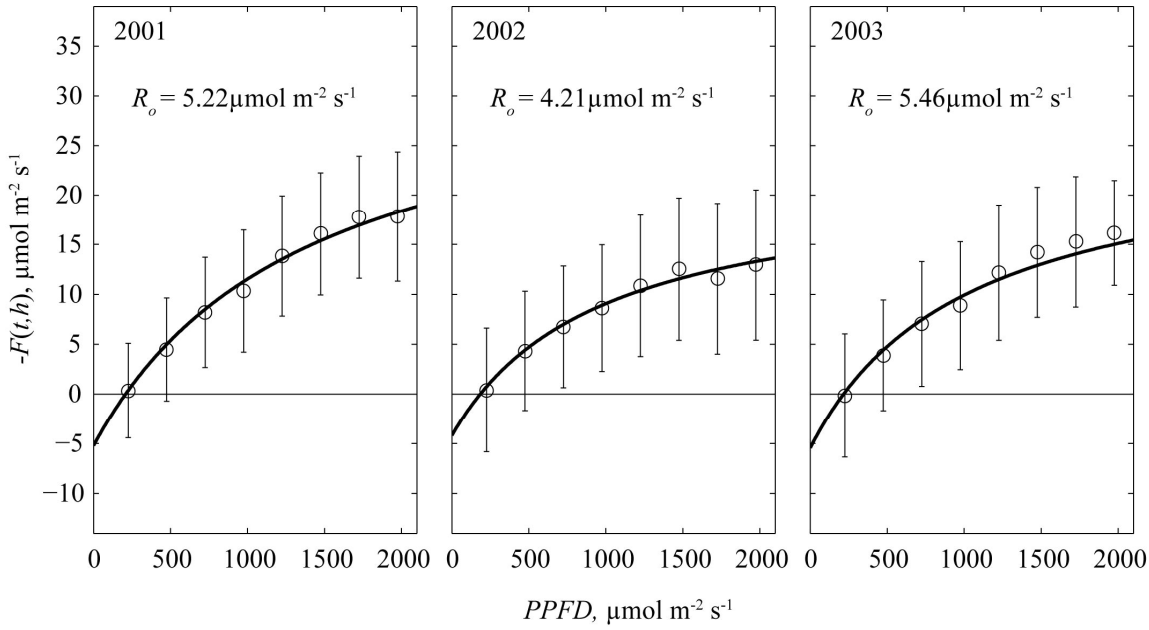

Figure 9: The canopy scale light response curve determined from eddy-covariance flux measurements and *PPFD* measurements at the top of canopy for each year. The open circle and error bar shows the statistics (mean and standard deviation) of the flux measurement against different *PPFD* levels, and the solid line shows the fitted light response curve for each year. The values of R_o are shown for convenience.

2.5. Summary and Conclusions

We developed a Eulerian version of the constrained source optimization (CSO_E) model that considers local atmospheric stability and storage fluxes. The model uses simultaneous mean air temperature and mean CO_2 concentration profiles in the inversion for forest floor efflux and above ground source distribution. Based on model calculations and measurements at a maturing pine forest in the southeastern United States, we demonstrated the following:

(1) At this study site, the contribution of the storage flux during nighttime conditions is at least 27% of the EC measured flux, even under high friction velocity u^* conditions.

(2) Considering local atmospheric stability in the CSO_E model increases the modeled ecosystem annual respiration by about 10%, and can be comparable to storage fluxes.

(3) The CSO_E model captures well forest floor carbon efflux during both wet and dry years. Also, the variation of the optimized aboveground source parameter is consistent with seasonal variation in $V_{c\max,25}$.

(4) The CSO_E modeled CO_2 flux above the canopy was systematically higher than the eddy-covariance measurements by about 30% for low u^* and about 10% for high u^*. A separate analysis using the *Massman* [2000] analytical model revealed that high

frequency corrections to the eddy-covariance measurements can explain only 50% of this difference.

(5) The CSO_E modeled ecosystem respiration, when evaluated within the overall carbon balance at the site, appears consistent with various independent component estimates.

(6) The CSO_E modeled ecosystem respiration agreed well with independent respiration estimates derived from the intercept of the annual $\overline{F}(t,h)$-*PPFD* light-response curves. This agreement lends support to a symbiotic use of both methods to further constrain nighttime ecosystem respiration.

The broader implications of this work are twofold. Given the large uncertainties in R_E, a logical starting point is to derive multiple estimates of R_E - with each estimate sensitive to different assumptions. Chamber estimates provide bottom-up values with limited spatial extent; EC methods provide top-down estimates that can be linked to R_E using numerous assumptions and simplifications (but independent from the chamber data). Agreement between these estimates hints at a robust value for R_E, while disagreement flags uncertainties. The proposed CSO_E provides an additional, independent estimate of R_E at the EC spatial scale but has the decisive advantage over EC based estimates because of its ability to separate forest floor effluxes from aboveground fluxes. Therefore, the model can serve as a link between EC based measurements and chamber measurements of R_E, helping to isolate uncertainties in R_E originating from forest-floor estimates from those generated by above ground estimates.

The CSO_E model can be readily linked to stable isotope measurements. Information from stable isotope measurements can be combined into the CSO_E optimization by providing further constraints on the ratio of floor efflux and above ground CO_2 production at multiple levels within the canopy. The optimization solutions above ground can also be qualitatively assessed against expected shifts in physiological properties (e.g. $V_{c\max,25}$).

Although the CSO_E model is a useful step for constraining nighttime R_E, certain difficulties remain. For example, the Eulerian formulation provided is 1-dimensional and neglects topography-induced drainage flows. The closure formulations are derived assuming fully developed turbulence; an assumption that may frequently be violated at night. Lastly, the CSO_E formulation has several inconsistent "internal" approximations. For example, the assumption of non-steady state means continuity equation (to account for mean storage fluxes) *versus* that of steady-state flux budget equations (for simplicity).

3. Investigating a hierarchy of Eulerian closure models for scalar transfer inside forested canopies

3.1 Background and Introduction

Quantifying the exchange of scalars (e.g., carbon dioxide CO_2, water vapor H_2O, temperature, or other chemical species) between leaves and their local environment (hereafter referred to as microenvironment) is frustrated by a 2-way interaction in which the microenvironment exerts controls over scalar exchange at the leaf surface, and leaves have some capacity to regulate their own microenvironment through stomatal opening and closure. This 2-way interaction is further complicated by the vertical distribution of foliage within the canopy leading to significant vertical gradients in the radiation environment and airflow regimes. The intrinsic non-linearity in leaf physiological responses (e.g. leaf-level photosynthesis and transpiration) to radiation further exasperates this problem.

To date, most eco-physiological approaches to modeling annual and inter-annual ecosystem scale carbon and water fluxes have focused on radiative transfer and the non-linearity in the physiological response to incident radiation at the leaf surface [*Aber et al.*, 1996; *De Pury and Farquhar*, 1997; *Kirschbaum et al.*, 1998; *Leuning et al.*, 1995; *Luo et al.*, 2001; *Naumburg et al.*, 2001; *Wang and Leuning*, 1998; *Williams et al.*, 1996; *Williams et al.*, 1998]. These models assume that within the canopy volume, scalar concentration (primarily CO_2, H_2O, and temperature) is constant and identical to its state above the canopy (hereafter, referred to as the well-mixed assumption, WMA). This is

not surprising because at annual or inter-annual time scales, any attempt to resolve such 2-way interaction adds significant computational burden and model complexity (as we show later) with perhaps modest gains in predictive skills, though the degree of improvement remains largely unexplored. Furthermore, uncertainties in describing the non-stationarity and vertical inhomogeneity in physiological parameters (e.g., in photosynthesis calculations) may overshadow any improvements gained by resolving this 2-way interaction.

While the well-mixed assumption may be defensible for some canopy types, it is too simplistic for tall-forested ecosystems, especially when such assumption is confronted with experimental evidence that vertical variations in excess of 50 ppm for CO_2 concentration and 3 degrees or more for air temperature occur inside the canopy volume during day time conditions [*Lai et al.*, 2002a; *Siqueira and Katul*, 2002] . Because the vertical variations in mean scalar concentration profiles are not random within the canopy, the well-mixed assumption may inject systematic biases in modeling scalar sources, sinks, and fluxes. Hence, future developments in ecosystem carbon-water source-sink, and flux modeling will benefit from answering two inter-related questions:

1) If the well-mixed assumption is to be 'relaxed', then how detailed must the turbulent transport model be to resolve this 2-way interaction?
2) Is the predictive skill gained by resolving this 2-way interaction much smaller than biases incurred by not correcting for non-stationarity in physiological parameters such as the ones most pertinent to leaf photosynthesis?

These two questions frame the study objectives here and are explored using the multi-year record available at the *AmeriFlux* Duke Forest loblolly pine site as a case study.

Several multi-layer one-dimensional models have been developed to resolve the two-way interaction between leaf and microclimate using turbulent transport theories in conjunction with detailed physiological and radiative transfer principles [*Baldocchi*, 1992; *Baldocchi et al.*, 1997; *Baldocchi and Meyers*, 1998; *Leuning et al.*, 1995; *Meyers and Paw U*, 1986; 1987; *Raupach*, 1988; 1989a; *Simon et al.*, 2005a; *Simon et al.*, 2005b]. The term 'CANVEG' (for 'canopy vegetation') was coined for such multi-layer models [*Baldocchi*, 1992; *Baldocchi et al.*, 1997; *Baldocchi and Meyers*, 1998]. Linkages between scalar sources and mean concentration in the original CANVEG (e.g. Baldocchi, 1992) relied on the principles of Lagrangian fluid mechanics for characterizing turbulent dispersion [*Raupach*, 1989a], which was a major theoretical improvement over classical Eulerian first-order flux-gradient closure models (or K-theory). However, the Lagrangian-framework in CANVEG suffered from two fundamental limitations: (i) it cannot explicitly treat thermal stratification inside the canopy volume, known to be significant in tall forested ecosystems [*Malhi et al.*, 1998; *Siqueira and Katul*, 2002], and (ii) it requires detailed higher-order velocity statistics profiles (e.g. vertical velocity standard deviation profile), which either have to be measured or modeled. To circumvent some of these limitations, Lai et al. [2000a; 2000b] and Siqueira et al [2002] modified the CANVEG approach in Baldocchi [1992] and Baldocchi and Meyers [1998] by employing a Eulerian-Lagrangian hybrid framework for turbulent dispersion. The basic premise is to

utilize higher order Eulerian closure approaches [*Meyers and Paw U*, 1986; *Wilson*, 1989; *Wilson and Shaw*, 1977] to compute the velocity statistics within the canopy, and then use Lagrangian transport theory to couple scalar sources to their mean concentration, while retaining similar physiological and radiative transfer schemes as in CANVEG. The approach in Lai et al. [2002a; 2002b] eliminates one of the two limitations earlier mentioned, but thermal stratification inside the canopy was treated as a modifier to the upper boundary conditions of the modeled velocity statistics and on the Lagrangian integral time scale, an approach also employed by Leuning [2000].

Here, we develop a multilayer biosphere-atmosphere model that retains the detailed eco-physiological parameterization and radiative transfer principles in CANVEG, but the complexity in the turbulent transport scheme needed to capture this two-way interaction between the canopy and its microclimate is varied in a hierarchical manner. Different closure approximations ranging from first- to third-order schemes are employed to parameterize higher order turbulent moments in the governing conservation equations for both momentum and scalar transfer. As a reference, we contrast these model calculations with scalar sources and flux calculations made by assuming a well-mixed state for the mean scalar fields (i.e., a zeroth order closure in the model hierarchy). In addition, we repeat these model calculations with and without resolving the effects of atmospheric stability inside the canopy. Resolving atmospheric stability locally inside the canopy necessitates a computationally expensive iterative scheme for solving simultaneously the Reynolds stress budget and heat flux budget equations, which may not be feasible for inter-annual water and carbon flux calculations.

Because the interest here is in the effect of the 2-way leaf-microclimate interaction on fluxes, sources (or sinks), and mean concentration (or temperature) at 'ecological' (i.e. seasonal to inter-annual) time scales, models with different hierarchical turbulent closure complexity are compared against a multi-year long eddy-covariance sensible and latent heat fluxes and CO_2 flux record collected in a uniformly planted Loblolly pine (*Pinus taeda* L.) stand in the Blackwood Division of Duke Forest, described next. Because the CANVEG model does not explicitly account for soil moisture stress (i.e., soil-plant hydrodynamics are not considered), we restrict the data-model inter-comparison to years with well-watered soil moisture states.

3.2 Experiment

3.2.1 Study Site

All data were collected at the *AmeriFlux* pine ecosystem in the Blackwood Division of the Duke Forest near Durham, North Carolina (site location: 35°58'N, 79°05'W, 163 m above sea level) as part of a long-term H_2O/CO_2 flux monitoring initiative [*Baldocchi et al.*, 2001]. The study site is a uniformly planted loblolly pine forest (planted in 1983 at 2 m × 2.4 m spacing) extending some 300 to 600 m in the east-west direction and 1000 m in the south-north direction. The long-term mean annual precipitation is 1185 ± 177 mm, and the annual mean air temperature is 14.9 ± 0.9 °C. The local topographic variations in the vicinity around the micrometeorological tower are

small (slope $< 5\%$) enough to ignore the effect of complex terrain on the flow statistics [*Siqueira et al.*, 2002]. In addition to the dominant pine overstory, the sub-canopy (roughly ranging in height from $0 \sim 0.4h$, where h is the mean canopy height of the main canopy) contains some 40 woody species, of which *Liquidambar styraciflua L.*, *Acer rubrum L.*, *Ulmus alata Michx.*, and *Cornus florida L.* are the most prevalent [*Palmroth et al.*, 2005].

While the forest is evergreen, leaf area index (LAI) variations can be significant as evidenced by the measurements in Figure 10. During the growing-season in 2002, the ecosystem experienced a severe drought lasting few months, and on December 4^{th} and 5^{th} of 2002, an ice storm struck the area causing severe damage to the canopy structure [*McCarthy et al.*, 2006b]. The lower panel of Figure 10 shows the vertical distribution of the foliage at different times of the year. This complex spatial and temporal variation in foliage distribution will have appreciable effects on both the radiation/energy environment and the attenuation of turbulent flow statistics inside the canopy volume, thereby significantly influencing the 2-way interaction.

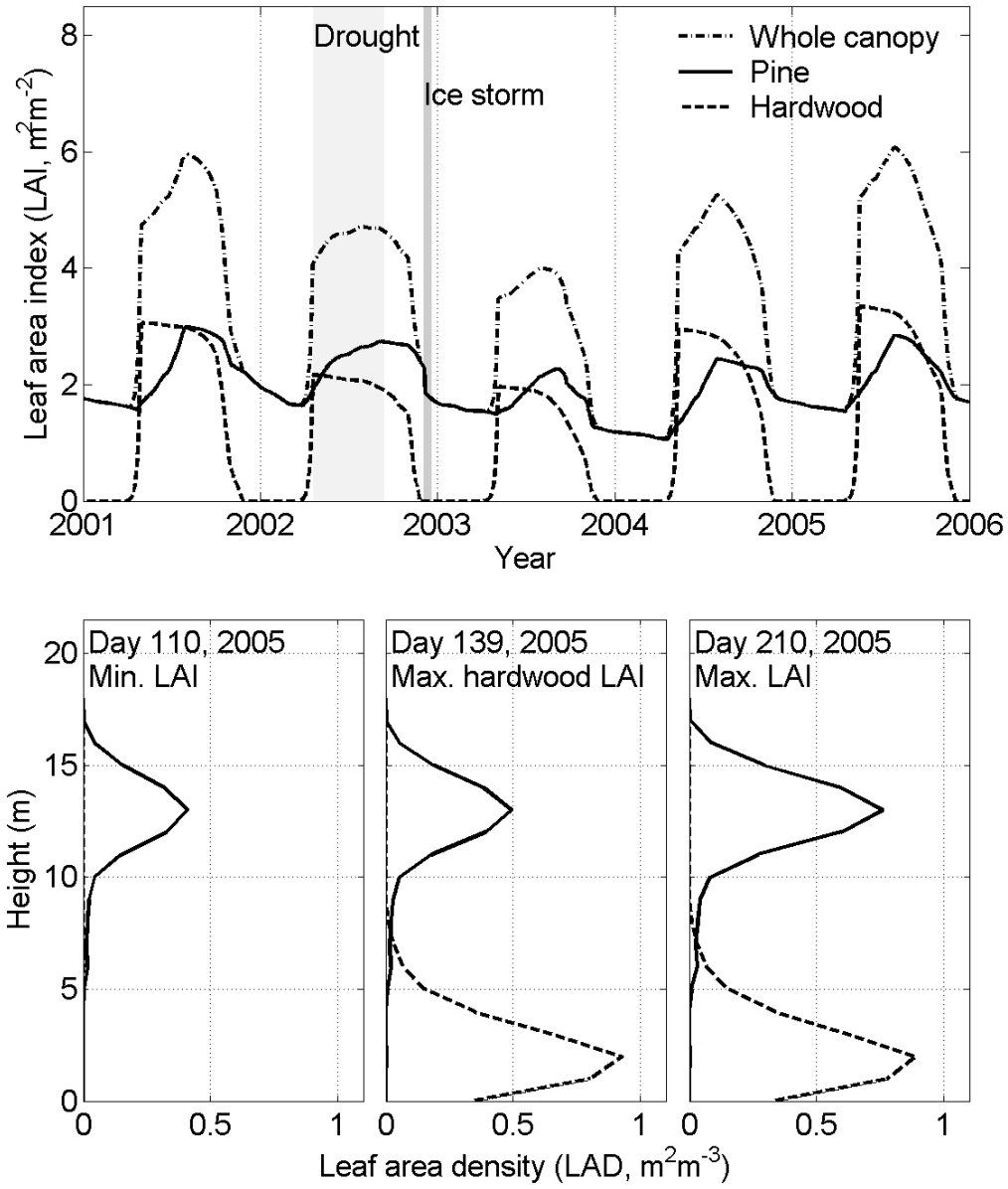

Figure 10: Top: Leaf area index (LAI, $m^2\ m^{-2}$) variation from 2001 to 2005 for the pine canopy and the hardwood understory. The light-gray area and the darker-gray area respectively, represent the severe drought event during the growing season and the ice storm event in December of 2002. Bottom: the leaf area density (LAD, $m^2\ m^{-3}$) profiles at different times of the year based on different LAI values in 2005.

3.2.2 Measurements

The velocity statistics (wind velocity and Reynolds stresses), sensible heat flux (H_S), latent heat flux (LE), and CO_2 fluxes were measured above the canopy using an eddy-covariance (hereafter EC) system composed of a LI-7500 open-path CO_2/H_2O gas analyzer (Li-Cor Inc., Lincoln, NE, USA) and a CSAT3 tri-axial sonic anemometer (Campbell Scientific Inc., Logan, UT, USA). The EC data were sampled at 10 Hz and averaged every 30 minutes. The effects of air density fluctuations on CO_2 and H_2O flux measurements were corrected after Webb et al. [1980] (see also [*Detto and Katul*, 2006].

The net radiation (R_n) was measured using a Fritschen-type net radiometer at the canopy top from 1997 until 2003, and then this radiometer was replaced with a Kipp & Zonen CNR1 net radiometer (Kipp & Zonen USA Inc., Bohemia, NY, USA) in 2004. The photosynthetically active radiation (PAR) was measured with a Li-Cor LI-190SA quantum sensor at the canopy top. The mean air temperature and relative humidity were measured using a Campbell Scientific HMP35C temperature/relative humidity probe at 2/3 canopy height. To sample the vertical distribution of scalar concentrations, a multi-port system was installed at 10 different levels (0.1, 0.75, 1.5, 3.5, 5.5, 7.5, 9.5, 11.5, 13.5, and 15.5 m) and a Li-Cor 6262 CO_2/H_2O infrared gas analyzer was used to measure the concentrations. Another profiling system was employed to measure the air temperature at 8 levels (1.5, 3.5, 5.5, 7.5, 9.5, 11.5, 13.5, and 15.5 m) using shielded copper-constantan thermocouple sensors.

The forest floor CO_2 efflux was measured with an automated carbon efflux system (ACES, US Patent 6692970) developed by the USDA Forest Service, Southern Research Station Laboratory in Research Triangle Park, NC [*Butnor et al.*, 2003; *Butnor and Johnsen*, 2004; *Palmroth et al.*, 2005]. The details of the ACES configuration, quality checks, and spatial sampling area are described in Palmroth et al. [2005]. These measurements were used to drive the lower boundary conditions for the mean CO_2 continuity equation (see **Appendix C**).

The plant area index (PAI, m^2 m^{-2}) was measured several times per year using a pair of Li-Cor LAI 2000 optical sensors. The plant area density (hereafter PAD, m^2 m^{-3}) measurements were conducted at 1 m intervals from the forest floor up to the canopy top [*Lai et al.*, 2000b; *Pataki et al.*, 1998; *Schafer et al.*, 2003]. The dynamics of leaf area were reconstructed using for broadleaf species, data on leaf litterfall mass and timing, specific leaf area and allometry, and for *Pinus taeda*, needle litterfall (lagged by 2 years to account for foliage longevity) and timing, combined with needle elongation rates and fascicle and shoot counts [*McCarthy et al.*, 2006a]. Further details about the site and data processing are described elsewhere [*Juang et al.*, 2006; *Oren et al.*, 1998; *Palmroth et al.*, 2005; *Pataki and Oren*, 2003; *Stoy et al.*, 2005].

3.3. Theory

3.3.1 Governing Equation

For completeness, the models employed in the turbulent closure hierarchy are briefly reviewed. For a steady-state, incompressible, high Reynolds- and Peclet- numbers flows, the time and spatially averaged budget equation for the mean longitudinal momentum, in the absence of Coriolis effects and for the case of planar-homogeneous canopy, can be expressed as [*Katul and Albertson*, 1998; *Meyers and Paw U*, 1987; *Wilson and Shaw*, 1977]

$$\frac{\partial \langle \overline{u} \rangle}{\partial t} = 0 = -C_{\mathrm{d}}\, A(z) \langle \overline{u} \rangle^2 - \frac{\partial \langle \overline{u'w'} \rangle}{\partial z}, \tag{3-1}$$

where u and w are the instantaneous longitudinal and vertical velocity components, C_{d} is the drag coefficient [*Wilson and Shaw*, 1977], and $A(z)$ is the bulk PAD at level z. Over-bars and brackets represent temporal and spatial averaging of a flow variable, and primed quantities denote departures from this average. Using multiple sonic anemometer measurements, Katul and Albertson [1998] determined $C_{\mathrm{d}} = 0.2$ for this stand, and this value is used throughout.

Using similar simplifications and averaging procedures, the steady state budget equation for an arbitrary scalar ξ is given by

$$\frac{\partial\left\langle\overline{\xi}\right\rangle}{\partial t}=0=S_{\xi}-\frac{\partial\left\langle\overline{w'\xi'}\right\rangle}{\partial z}, \tag{3-2}$$

where S_{ξ} are local sources and sinks by the vegetation elements.

Assuming Fickian diffusion (or its resistor analogy) for mass transfer from leaf-to-surrounding atmosphere, S_{ξ} becomes proportional to the difference in scalar quantities between the leaves and their surrounding air. Upon scaling with the local leaf area density (LAD), $a(z)$, leads to a spatially averaged source given by

$$S_{\zeta}=a(z)\,G_{\zeta}\left(\left\langle\overline{\xi_{\mathrm{L}}}\right\rangle-\left\langle\overline{\xi}\right\rangle\right), \tag{3-3}$$

where G_{ζ} (m s^{-1}) is the bulk conductance for scalar ξ between the leaves and the surrounding air, and ξ_{L} is the mean quantity of a specific scalar (ξ) inside the leaf, which could be one of the three considered here: the leaf surface temperature (at the skin) $\left\langle\overline{T_{\mathrm{L}}}\right\rangle$, the intercellular saturated water vapor concentration $\left\langle\overline{q_{\mathrm{L}}}\right\rangle$ and the intercellular CO_2 concentration $\left\langle\overline{C_{\mathrm{L}}}\right\rangle$. For water vapor and CO_2 concentrations, G_{ζ} includes both stomatal conductance ($g_{\mathrm{s},\xi}$, mol m^{-2} s^{-1}) and boundary-layer conductance ($g_{\mathrm{b},\xi}$, mol m^{-2} s^{-1}), while only boundary-layer conductance contributes to heat transfer. Note that PAD is responsible for momentum extraction, but only LAD is responsible for water vapor transfer, though we consider the two to be approximately equal here.

Using a flat-plate boundary layer analogy at the leaf surface, the boundary-layer conductance is given by [*Campbell and Norman*, 1998]:

$$g_{\mathrm{b},\xi} = \upsilon_{\xi} \cdot \left(\frac{\langle \bar{u} \rangle}{0.7 \cdot d} \right)^{0.5},$$

(3-4)

where υ_{ξ} is a molecular transfer coefficient for scalar ξ, and d is the characteristic length of the leaf. Here, $d = 0.0015$ m for the pine foliage and $d = 0.15$ m for the understorey broadleaf foliage.

3.3.2 Closure Approximation

In Equations (3-1) and (3-2), the turbulent momentum $\langle \overline{u'w'} \rangle$ and scalar $\langle \overline{w'\xi'} \rangle$ fluxes are additional unknowns that require parameterization so that sources, sinks, fluxes, and concentration can be solved. In the hierarchy of models, either parameterizations or full budget equations for these higher-order terms are derived.

First-order closure model

The first-order closure approximation (or K-theory) simply parameterizes the turbulent fluxes in Equations (3-1) and (3-2) into

$$\begin{cases} \langle \overline{u'w'} \rangle = -K_{\mathrm{m}} \dfrac{\partial \langle \bar{u} \rangle}{\partial z} \\ \langle \overline{w'\xi'} \rangle = -K_{\xi} \dfrac{\partial \langle \bar{\xi} \rangle}{\partial z} \end{cases},$$

(3-5)

where K is the eddy diffusivity, parameterized based on the Prandtl-von Karman mixing length hypothesis as

$$K = L(z)^2 \left| \frac{\partial \langle \bar{u} \rangle}{\partial z} \right|, \tag{3-6}$$

where $L(z)$ is a canonical mixing length at height z. Katul et al. [2004] recently summarized previous research [*Liu et al.*, 1996; *Massman and Weil*, 1999; *Poggi et al.*, 2004] and concluded that $L(z)$ may be assumed approximately constant inside the canopy volume for a dense canopy and can be estimated from:

$$L(z) = \begin{cases} \alpha h; & z < h \\ k(z - d_0); & z \geq h \end{cases}, \tag{3-7}$$

where $k = 0.4$ is the von Karman constant, and d_0 is the zero-plane displacement height determined from the centroid of the drag force [*Jackson*, 1981; *Thom*, 1971]. The parameter α is calculated by assuming that $L(z)$ is continuous at the canopy top [*Katul et al.*, 2004].

Second-order closure model

Instead of using K-theory to characterize turbulent fluxes in Equations (3-1) and (3-2), budget equations can be derived for the turbulent flux though triple correlation-terms must be subsequently parameterized. For the momentum and Reynolds stress equations, standard closure approximations result in (Wilson and Shaw, 1977; Katul and Albertson, 1998; Katul and Chang, 1999)

$$\frac{\partial\left\langle\overline{u'w'}\right\rangle}{\partial t}=0=-\left\langle\overline{w'w'}\right\rangle\frac{\partial\left\langle\bar{u}\right\rangle}{\partial z}-\frac{Q\left\langle\overline{u'w'}\right\rangle}{3\lambda_2}+C_{\mathrm{w}}Q^2\frac{\partial\left\langle\bar{u}\right\rangle}{\partial z}-\frac{\partial}{\partial z}\left\langle\overline{w'u'w'}\right\rangle \tag{3-8a}$$

$$\begin{aligned}\frac{\partial\left\langle\overline{u'u'}\right\rangle}{\partial t}=0=&-2\left(\left\langle\overline{u'w'}\right\rangle\frac{\partial\left\langle\bar{u}\right\rangle}{\partial z}+\left\langle\bar{u}\right\rangle\frac{\partial\left\langle\overline{u'w'}\right\rangle}{\partial z}\right)-\frac{Q}{3\lambda_2}\left(\left\langle\overline{u'u'}\right\rangle-\frac{Q^2}{3}\right)\\&-\frac{2}{3}\frac{Q^3}{\lambda_3}-\frac{\partial}{\partial z}\left\langle\overline{w'u'u'}\right\rangle\end{aligned} \tag{3-8b}$$

$$\frac{\partial\left\langle\overline{v'v'}\right\rangle}{\partial t}=0=-\frac{Q}{3\lambda_2}\left(\left\langle\overline{v'v'}\right\rangle-\frac{Q^2}{3}\right)-\frac{2}{3}\frac{Q^3}{\lambda_3}-\frac{\partial}{\partial z}\left\langle\overline{w'v'v'}\right\rangle \tag{3-8c}$$

$$\frac{\partial\left\langle\overline{w'w'}\right\rangle}{\partial t}=0=-\frac{Q}{3\lambda_2}\left(\left\langle\overline{w'w'}\right\rangle-\frac{Q^2}{3}\right)-\frac{2}{3}\frac{Q^3}{\lambda_3}+\frac{2g}{\left\langle\bar{T}\right\rangle}\left\langle\overline{w'T'}\right\rangle-\frac{\partial}{\partial z}\left\langle\overline{w'w'w'}\right\rangle \tag{3-8d}$$

where g is the gravitational acceleration, Q is the characteristic turbulent velocity, given by $\sqrt{\left\langle\overline{u_i'u_i'}\right\rangle}$, and λ_1, λ_2, and λ_3 are the characteristic length scales for the triple velocity correlations, the pressure-velocity gradient correlations, and the viscous dissipation, respectively. These three length scales are determined by $\lambda_i=a_i\times L$, where a_i and C_{w} are similarity constants.

Similarly, the closure approximation of the turbulent scalar flux for ξ ($\left\langle\overline{w'\xi'}\right\rangle$) can be derived:

$$\frac{\partial\left\langle\overline{w'\xi'}\right\rangle}{\partial t}=0=-\left\langle\overline{w'w'}\right\rangle\frac{\partial\left\langle\bar{\xi}\right\rangle}{\partial z}-\frac{Q}{3\lambda_2}\left\langle\overline{w'\xi'}\right\rangle+\frac{g}{\left\langle\bar{T}\right\rangle}\left\langle\overline{T'\xi'}\right\rangle-2\frac{Q}{\lambda_3}\left\langle\overline{w'\xi'}\right\rangle+\frac{\partial}{\partial z}\left\langle\overline{w'w'\xi'}\right\rangle$$

. (3-9)

Note that the third terms on the right hand-side of Equations (3-8d) and (3-9) are the buoyant production/consumption that necessitate coupling between momentum and scalar exchange. The steady-state budget equation for the correlation term $\left\langle \overline{T'\xi'} \right\rangle$ is given as

$$\frac{\partial \left\langle \overline{T'\xi'} \right\rangle}{\partial t} = 0 = -\left\langle \overline{w'\xi'} \right\rangle \frac{\partial \left\langle \overline{\xi} \right\rangle}{\partial z} - \left\langle \overline{w'T'} \right\rangle \frac{\partial \left\langle \overline{\xi} \right\rangle}{\partial z} - 2\frac{Q}{\lambda_3} \left\langle \overline{T'\xi'} \right\rangle + \frac{\partial}{\partial z} \left\langle \overline{w'T'\xi'} \right\rangle . \tag{3-10}$$

In Equations (3-8), (3-9), and (3-10), the triple correlation terms are extra unknowns that require closure assumptions. The following second-order closure approximation proposed by Mellor [1973] and modified by Wilson and Shaw [1977] is employed to parameterize the turbulent fluxes of the Reynolds stresses in Equation (3-8),

$$\begin{cases} \left\langle \overline{w'u'w'} \right\rangle = -2Q\lambda_1 \dfrac{\partial \left\langle \overline{u'w'} \right\rangle}{\partial z} \\ \left\langle \overline{w'u'u'} \right\rangle = -Q\lambda_1 \dfrac{\partial \left\langle \overline{u'u'} \right\rangle}{\partial z} \\ \left\langle \overline{w'v'v'} \right\rangle = -Q\lambda_1 \dfrac{\partial \left\langle \overline{v'v'} \right\rangle}{\partial z} \\ \left\langle \overline{w'w'w'} \right\rangle = -3Q\lambda_1 \dfrac{\partial \left\langle \overline{w'w'} \right\rangle}{\partial z} \end{cases} . \tag{3-11a}$$

Similarly, the turbulent fluxes of the scalars and buoyant terms can be expressed as

$$\begin{cases} \left\langle \overline{w'w'\xi'} \right\rangle = -2Q\lambda_1 \dfrac{\partial \left\langle \overline{w'\xi'} \right\rangle}{\partial z} \\ \left\langle \overline{w'T'\xi'} \right\rangle = -Q\lambda_1 \dfrac{\partial \left\langle \overline{T'\xi'} \right\rangle}{\partial z} \end{cases} . \tag{3-11b}$$

Details of the closure approximations for Equations (3-8) to (3-11) are discussed in **Appendix C**.

Third-order closure model

Unlike the second-order closure model, third-order closure schemes do not parameterize the triple correlation terms but employ full budget equations. Here, the equations discussed in previous studies [*Katul and Albertson*, 1998; *Meyers and Paw U*, 1986; 1987] are used. To contrast with second-order closure modeling (equation 11b), we summarize the outcome for the triple moments [*Katul and Albertson*, 1998; *Meyers and Paw U*, 1986; 1987]:

$$\left\langle \overline{w'u'u'} \right\rangle = -\frac{\tau}{C_1}\left(2\left\langle \overline{w'u'w'} \right\rangle \frac{\partial \left\langle \overline{u} \right\rangle}{\partial z} + \left\langle \overline{w'w'} \right\rangle \frac{\partial \left\langle \overline{u'u'} \right\rangle}{\partial z} + 4\left\langle \overline{u'w'} \right\rangle \frac{\partial \left\langle \overline{u'w'} \right\rangle}{\partial z} \right)$$

$$\left\langle \overline{w'u'w'} \right\rangle = -\frac{\tau}{C_1}\left(\left\langle \overline{w'w'w'} \right\rangle \frac{\partial \left\langle \overline{u} \right\rangle}{\partial z} + \left\langle \overline{u'w'} \right\rangle \frac{\partial \left\langle \overline{w'w'} \right\rangle}{\partial z} + 3\left\langle \overline{u'w'} \right\rangle \frac{\partial \left\langle \overline{u'w'} \right\rangle}{\partial z} \right)$$

$$\left\langle \overline{w'w'w'} \right\rangle = -\frac{\tau}{C_1}\left(3\left\langle \overline{w'w'} \right\rangle \frac{\partial \left\langle \overline{w'w'} \right\rangle}{\partial z} \right)$$

$$\left\langle \overline{w'v'v'} \right\rangle = -\frac{\tau}{C_1}\left(\left\langle \overline{w'w'} \right\rangle \frac{\partial \left\langle \overline{v'v'} \right\rangle}{\partial z} \right)$$

$$\left\langle \overline{w'w'\xi'} \right\rangle = -\frac{\tau}{C_1}\left(\left\langle \overline{w'w'w'} \right\rangle \frac{\partial \left\langle \overline{\xi} \right\rangle}{\partial z} + \left\langle \overline{w'\xi'} \right\rangle \frac{\partial \left\langle \overline{w'w'} \right\rangle}{\partial z} + 2\left\langle \overline{w'w'} \right\rangle \frac{\partial \left\langle \overline{w'\xi'} \right\rangle}{\partial z} \right)$$

$$\left\langle \overline{w'T'\xi'} \right\rangle = -\frac{\tau}{C_1}\left(\left\langle \overline{w'w'\xi'} \right\rangle \frac{\partial \left\langle \overline{T} \right\rangle}{\partial z} + \left\langle \overline{w'w'T'} \right\rangle \frac{\partial \left\langle \overline{\xi} \right\rangle}{\partial z} + \left\langle \overline{w'w'} \right\rangle \frac{\partial \left\langle \overline{T'\xi'} \right\rangle}{\partial z} + \left\langle \overline{w'T'} \right\rangle \frac{\partial \left\langle \overline{w'\xi'} \right\rangle}{\partial z} + \left\langle \overline{w'\xi'} \right\rangle \frac{\partial \left\langle \overline{w'T'} \right\rangle}{\partial z} \right) \tag{3-12}$$

In Equation (3-12), the coefficient C_1 is a similarity constant and τ is a relaxation time scale defined as Q^2/ε, where $\varepsilon = \frac{2}{3}\frac{Q^3}{\lambda_3}$ is the mean turbulent kinetic energy dissipation rate. More details are provided in **Appendix C**. Closure models beyond order 3 are rarely used in atmospheric turbulence research and are not considered in this hierarchy.

3.3.3 Radiation Budget within Canopy Volume

The radiative distribution within the canopy volume uses a multi-layer light attenuation model described in Leuning et al. [1995] and Schafer et al [2003]. Basic concepts and applications can be found elsewhere [*Campbell and Norman*, 1998; *Erbs et al.*, 1982; *Goudriaan and van Laar*, 1994; *Pataki et al.*, 1998; *Spitters*, 1986; *Spitters et al.*, 1986; *Stenberg*, 1998]. However, for completeness, salient features of the model are reviewed.

The total incoming solar radiation contains two major components with different spectra: the visible (VIS) and near-infrared radiation (NIR). Because the attenuation

properties of VIS and NIR within the canopy are different, the distributions of these two portions are treated separately [*Weiss and Norman*, 1985].

The isothermal form of net radiation (R_n) absorbed by the leaves at level z is given by [*Leuning et al.*, 1995]

$$R_n(z) = S_A(z) - R_L(z), \tag{3-13}$$

where S_A is the shortwave radiation absorbed by the leaves, and R_L is the isothermal net long-wave radiation, discussed in **Appendix D**.

Within the canopy volume, sunlit leaves absorb all the radiative components, the direct beam $S_{A,b}(z)$, diffuse $S_{A,d}(z)$, and scattered radiation $S_{A,s}(z)$, given by $S_{A,sl}(z) = S_{A,b}(z) + S_{A,d}(z) + S_{A,s}(z)$, while shaded leaves only absorb the diffuse and scattered components, i.e. $S_{A,sh}(z) = S_{A,d}(z) + S_{A,s}(z)$ [*Campbell and Norman*, 1998; *Leuning et al.*, 1995; *Schafer et al.*, 2003], where $S_{A,sl}(z)$ and $S_{A,sh}(z)$ are the absorbed shortwave radiation on sunlit and shaded leaves, respectively (see **Appendix D** for detailed discussion).

The vertical distribution of absorbed shortwave radiation for the sunlit ($S_{A,sl}$) and shaded leaves ($S_{A,sh}$) can be calculated as

$$\begin{cases} S_{A,sl}(z) = f_{sl}(z) S_{A,sl,VIS}(z) + f_{sl}(z) S_{A,sl,NIR}(z) \\ S_{A,sh}(z) = f_{sh}(z) S_{A,sh,VIS}(z) + f_{sh}(z) S_{A,sh,NIR}(z) \end{cases}, \tag{3-14}$$

where $f_{sl}(z)$ and $f_{sh}(z)$ are the fraction of leaf area for sunlit and shaded leaves respectively, and $f_{sl}(z)+f_{sh}(z)=1$. These two fractions are determined by the transmission coefficient of the beam component, τ_b (see **Appendix D**):

$$\begin{cases} f_{sl}(z)=\tau_b \\ f_{sh}(z)=1-\tau_b \end{cases}. \tag{3-15}$$

3.3.4 Leaf-Level Energy Balance

The energy balance at the leaf scale was used to calculate leaf surface temperature T_L [*Campbell and Norman*, 1998]. Using the linearization technique by Penman [1948], the leaf surface temperature T_L is approximated as [*Campbell and Norman*, 1998; *Lai et al.*, 2000a]:

$$T_L = T + \frac{S_A - \varepsilon_L \sigma T^4 - L_v \rho \dfrac{g_b g_{s,v}}{g_b + g_{s,v}} D}{C_p \rho g_b + L_v \rho \dfrac{g_b g_{s,v}}{g_b + g_{s,v}} + C_p \rho g_r} \tag{3-16}$$

where D is the water vapor deficit (kg kg^{-1}), C_p is the specific heat of air (J mol^{-1} K^{-1}), g_r is the radiative conductance (m s^{-1}), σ is the Stefan-Boltzman constant, and $g_{s,v}$ and $g_{b,v}$ are the stomatal and boundary layer conductance (mol m^{-2} s^{-1}) of water vapor, respectively.

3.3.5 Physiological Model and Photosynthesis

The stomatal conductance for CO_2, ($g_{s,c}$), can be estimated from the physiological model of Collatz et al. [1991] (originally proposed by [*Ball et al.*, 1987], given by

$$g_{s,c} = m\frac{A_n\ RH_s}{C_s} + b \tag{3-17}$$

where m and b are parameters determined from gas-exchange measurements, RH_s and C_s are the relative humidity and CO_2 concentration on the leaf surface, and A_n is the leaf net assimilation rate, which can be calculated from the $A_n - C_i$ curve after Farquhar et al [1980], given by

$$A_n = \frac{\kappa_1 (C_i - \Gamma^*)}{C_i + \kappa_2} - R_d \tag{3-18}$$

where $\kappa_1 = \alpha_p\ e_m\ I_p$ and $\kappa_2 = 2\,\Gamma^*$ for light-limited photosynthesis; $\kappa_1 = V_{cmax}$ and $\kappa_2 = K_C (1 + O_i / K_O)$ when the assimilation rate is limited by Rubisco activity, R_d is the dark respiration rate, α_p is the leaf absorptivity for PAR, e_m is the maximum quantum efficiency, I_p is the incident PAR flux density on the leaf surface, Γ^* is the CO_2 concentration in the absence of R_d, V_{cmax} is the maximum catalytic capacity of Rubisco per unit leaf area, K_C and K_O are Michaelis-Menten constants for CO_2 fixation and for oxygen inhibition with respect to CO_2, and O_i are the oxygen concentration

[*Campbell and Norman*, 1998; *Katul et al.*, 2003; *Lai et al.*, 2000b]. R_d can be estimated from V_{cmax} after Farquhar et al. [1980]:

$$R_d = \chi V_{cmax} \tag{3-19}$$

where χ=0.015 for this stand [*Campbell and Norman*, 1998; *Ellsworth*, 2000; *Juang et al.*, 2006]. The temperature dependency of $V_{cmax}(t,z)$ can be expressed as:

$$V_{cmax} = V_{cmax,25} \frac{\exp[a_1(T_L - 25)]}{1+\exp[a_2(T_L - 41)]} \tag{3-20}$$

where a_1 and a_2 are the species-specific adjustment coefficients, which are obtained via porometry measurement and $V_{cmax,25}$ is the value of V_{cmax} at 25 ^oC [*Campbell and Norman*, 1998; *Collatz et al.*, 1991; *Farquhar et al.*, 1980]. From previous studies conducted at the site [*Ellsworth*, 1999; *Naumburg and Ellsworth*, 2000; *Naumburg et al.*, 2001], $V_{cmax,25}$, a_1 and a_2 are 59 µmol m^{-2} s^{-1}, 0.051 and 0.205, respectively for the upper canopy pine foliage, and are 30 µmol m^{-2} s^{-1}, 0.088 and 0.290, respectively for the sub-canopy broadleaved plants [*Lai et al.*, 2002a] though seasonal acclimation of $V_{cmax,25}$ was reported by Ellsworth (1999). The consequences of this seasonal acclimation vis-à-vis resolving the 2-way interaction between the leaves and their microclimate will be discussed.

3.3.6 Combining sub-models: the CANVEG framework

Summing up, the CANVEG model 'skeleton' for an arbitrary layer within the canopy is as follows:

(1) The three mean scalar continuity equations for CO_2, H_2O, and temperature provide 3 equations but with 9 unknowns (2 mean scalar concentrations and 1 mean temperature, 3 turbulent scalar fluxes, and 3 scalar sources or sinks)

(2) The turbulent transport models (at any closure level) establish 3 additional equations linking turbulent fluxes to mean concentration (albeit the complexity of this expression varies with the closure scheme and can be impacted by thermal stratification). Hence, the physical system alone combining mean scalar continuity and turbulent transport theories provides 6 equations with 9 unknowns.

(3) The assumption that mass and heat transfer from the leaf surface (or stomatal pores) to the atmosphere is Fickian provides 3 additional equations that mathematically close the original system (9 equations with 9 unknowns) at the expense of introducing 4 additional unknowns: the stomatal conductance, and 3 internal or leaf-level mean concentration states.

(4) The fact that the 3 scalars considered here are heat, water vapor, and CO_2, permit us to use three additional equations: The leaf energy balance, the Farquhar photosynthesis model, and the assumption that the leaf stomatal pores are saturated. Finally, the system is mathematically closed via a semi-empirical stomatal conductance model for well-hydrated leaves (i.e. equation 17).

Again, because leaf stomatal pores are assumed to be saturated, drought conditions known to induce stomatal closure are excluded from the model-data comparisons. Note that the well-mixed assumption permits us to drop steps (i) and (ii) because the scalar concentration is assumed constant inside the canopy (as is virtually done in all forest growth models).

3.4. Results and Discussion

3.4.1 Boundary conditions

Boundary conditions are needed to solve the governing equations. We used the long-term EC measurements at the canopy top and derived similarity expressions for the normalized standard deviation of the components u, v, w, and the scalar quantities, θ, q, c as a function of the atmospheric stability parameter $\varsigma = \frac{z - d_0}{L}$, where L is the Obukhov length, and d_0 is the zero-plane displacement height (estimated from the centroid of the mean momentum flux). The similarity functions for different quantities and for different stability classes are shown in Figure 11; the least squares fitted curves shown in Figure 11 are summarized in Table 5. Despite the fact that these measurements were collected in the roughness sublayer just above the canopy, they appear to be consistent with a number field experiments in the surface layer summarized by Stull [1988] and Kaimal and Finnigan [1994]. The boundary conditions at the forest floor are detailed in **Appendix E**.

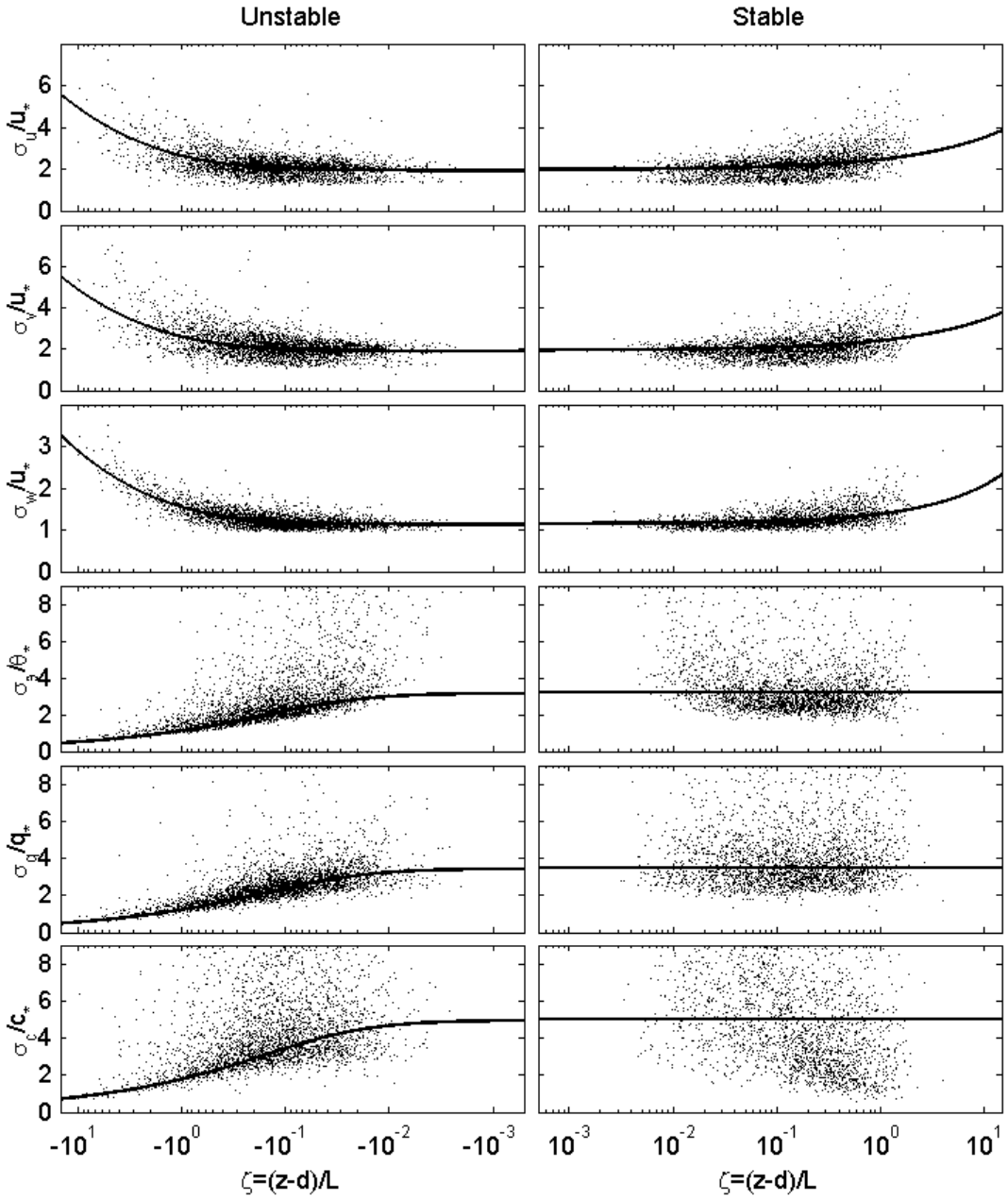

Figure 11: Normalized standard deviation of the velocity components u, u, w, and the scalar quantities, θ, q, and c for unstable (left column) and stable (right column) atmospheric stability conditions. All quantities are analyzed when the fiction velocity at the canopy top exceeds 0.1 m s^{-1}. The solid lines represent the regression curves whose parameters are summarized in Table 5.

Table 5: The similarity expressions for normalized standard deviation of the wind components u, v, w, and the scalar quantities, θ, q, c, for different atmospheric stability conditions ($\varsigma = (z - d_o)/L$).

Stability	Variable	Form	Constants
Unstable	σ_u/u_*	$a(b + c\zeta)^d$	a = 1.95; b = 1.0; c = -1.5; d = 1/3
	σ_v/u_*		a = 1.94; b = 1.0; c = -1.5; d = 1/3
	σ_w/u_*		a = 1.15; b = 1.0; c = -1.5; d = 1/3
	σ_θ/θ_*		a = 1.18; b = 0.05; c = -1.0; d = -1/3
	σ_q/q_*		a = 1.28; b = 0.05; c = -1.0; d = -1/3
	σ_c/c_*		a = 1.84; b = 0.05; c = -1.0; d = -1/3
Stable	σ_u/u_*	$a + b\zeta^d$	a = 1.95; b = 0.39; d = 0.5
	σ_v/u_*		a = 1.94; b = 0.37; d = 0.5
	σ_w/u_*		a = 1.15; b = 0.23; d = 0.6
	σ_θ/θ_*	c	c = 3.20
	σ_q/q_*		c = 3.47
	σ_c/c_*		c = 5.00
Neutral	σ_u/u_*	c	c = 1.95
	σ_v/u_*		c = 1.94
	σ_w/u_*		c = 1.15
	σ_θ/θ_*		c = 3.20
	σ_q/q_*		c = 3.47
	σ_c/c_*		c = 5.00

3.4.2 Radiation environment within the canopy volume

The radiative components (PAR and net) directly influence leaf photosynthesis (described later) and leaf energy exchange (latent heat and sensible heat). Incident shortwave radiation at the top of the canopy was not directly measured before 2004. To estimate the incident shortwave radiation for earlier periods, we derived a relationship between PAR (in μmol m^{-2} s^{-1}) and shortwave radiation (in W m^{-2}) measured by the Kipp & Zonen CNR1 net radiometer installed at the top of the canopy (in the summer of 2003). Note this relationship will be affected by zenith angle, location, and sky properties because the wavebands for PAR (in the spectral range of VIS, 400 to 700 nm) and shortwave radiation (VIS and NIR) are different. To convert units of PAR from μmol m^{-2} s^{-1} to W m^{-2}, a mean waveband =550 nm and a photon energy = 2.30×10^5 J mol^{-1} were used. The coefficient of determination ($R^2 = 0.99$) between PAR and shortwave radiation measurements, shown in Figure 12, suggests excellent linear relationship although minor scatter remains due to cloudy conditions.

To illustrate how the canopy is attenuating PAR, model results for PAR penetration ratios (i.e. the ratio of PAR at a given level z inside the canopy to the incident PAR at the top of the canopy) at midday (1200 LT) and in early morning hours (0800 LT) are shown in Figure 13. The results are presented as 7-day moving averages for the entire year of 2005 for illustration. The normalized leaf area density profiles are shown for reference. As expected, more PAR (~ 40% of the canopy top value) reaches the forest floor at midday in winter months (when LAI is minimum). However, less than 15% of

the canopy top PAR penetrates the canopy volume during the growing season, when LAI is at its maximum value. Figure 13 also shows the effects of solar position (zenith angle) at different times of day and the effects of LAD seasonal dynamics within the year – both significant contributors to the light environment within the canopy.

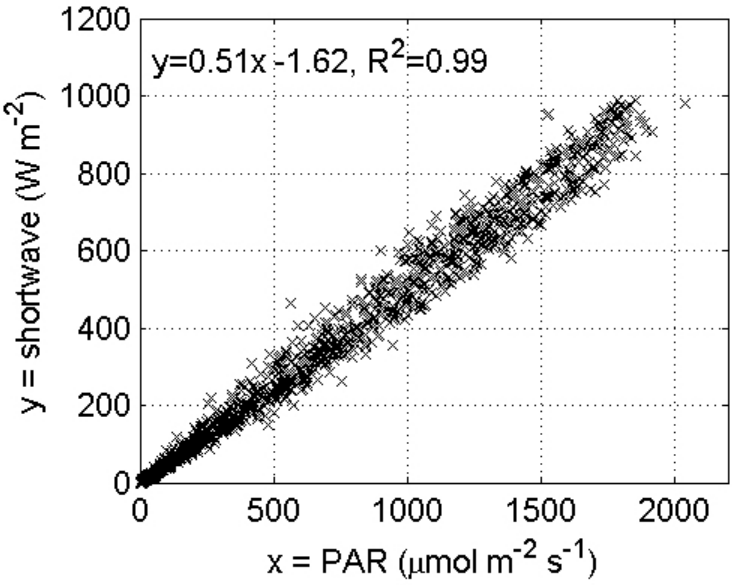

Figure 12: The relationship between half-hourly measured photosynthetically active radiation (PAR) and measured incident shortwave radiation at the top of the canopy during the summer of 2003. Regression equations for are shown for convenience.

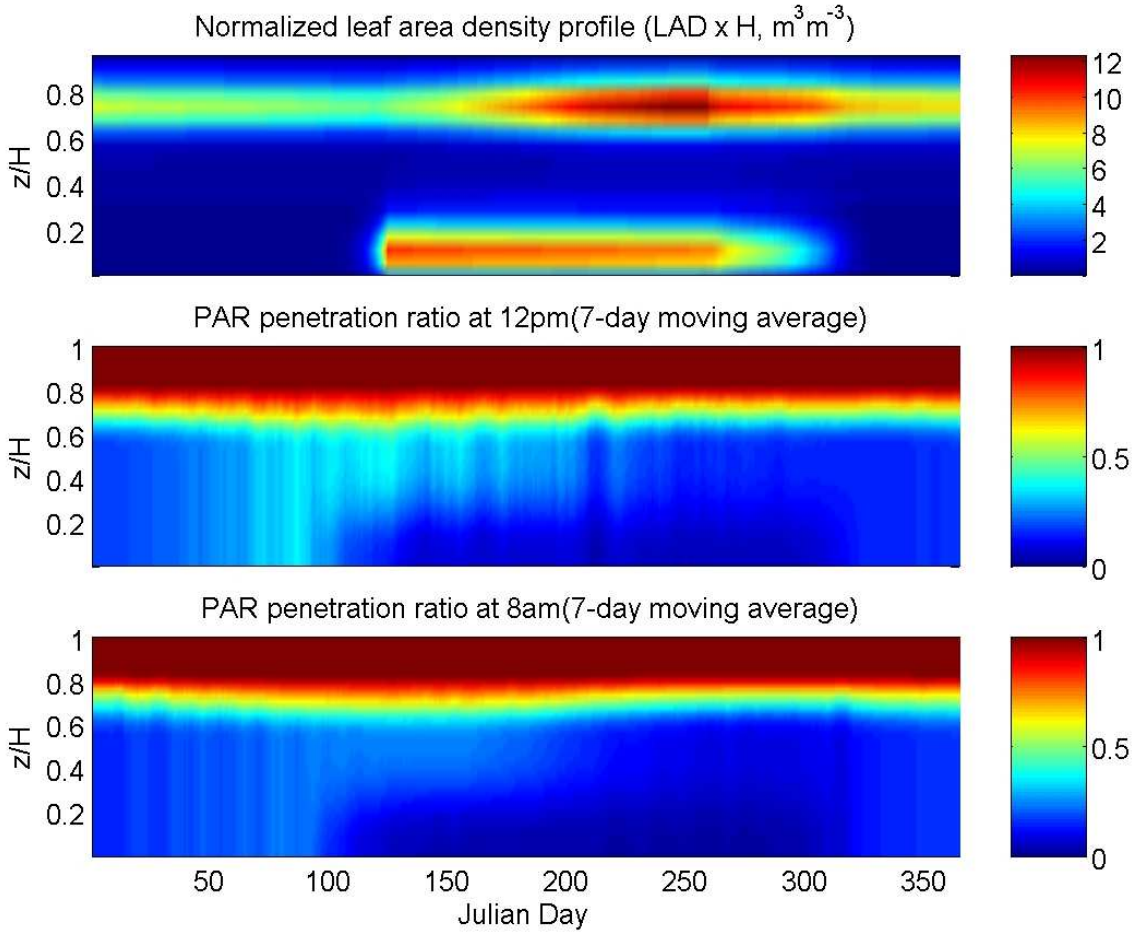

Figure 13: The vertical variation of modeled PAR penetration ratio throughout the year at different times during the day (1200 LT and 0800 LT) during 2005. The upper panel shows the normalized leaf area density profiles (LAD) for reference.

3.4.3 Scalar source strength and flux distribution

Figure 14 shows the source (or sink) strength for different scalars at different times of day throughout the entire year of 2005 using the second-order closure model with atmospheric stability corrections as an example. For the CO_2 source (or sink) strength, it is clear that while respiration dominates during nighttime conditions, the upper canopy becomes a strong sink during the day, especially during the growing-season. The co-existence of both net carbon sinks and sources within various canopy layers during the day is also evident during the winter season, and when the zenith angle is large (i.e., early morning and early evening). The model calculations suggest that the ecosystem is a large source of both latent- and sensible- heat during the growing season (as expected). Furthermore, it appears that canopy heating primarily occurs in the top-third of the canopy, where much of the radiation is intercepted.

Figure 15 shows the modeled time-depth variations of the scalar fluxes for the same time period of Figure 14. Again, the CO_2 flux distribution demonstrates that while soil respiration is large, this ecosystem remains a net carbon sink throughout the year as verified by eddy covariance measurements. Also, Figure 15 shows how the under-story plays a significant role in rapidly increasing CO_2 uptake from the atmosphere for early spring, but its relative impact on water vapor and sensible heat fluxes during this period appears less significant because of the enhanced role of evaporation.

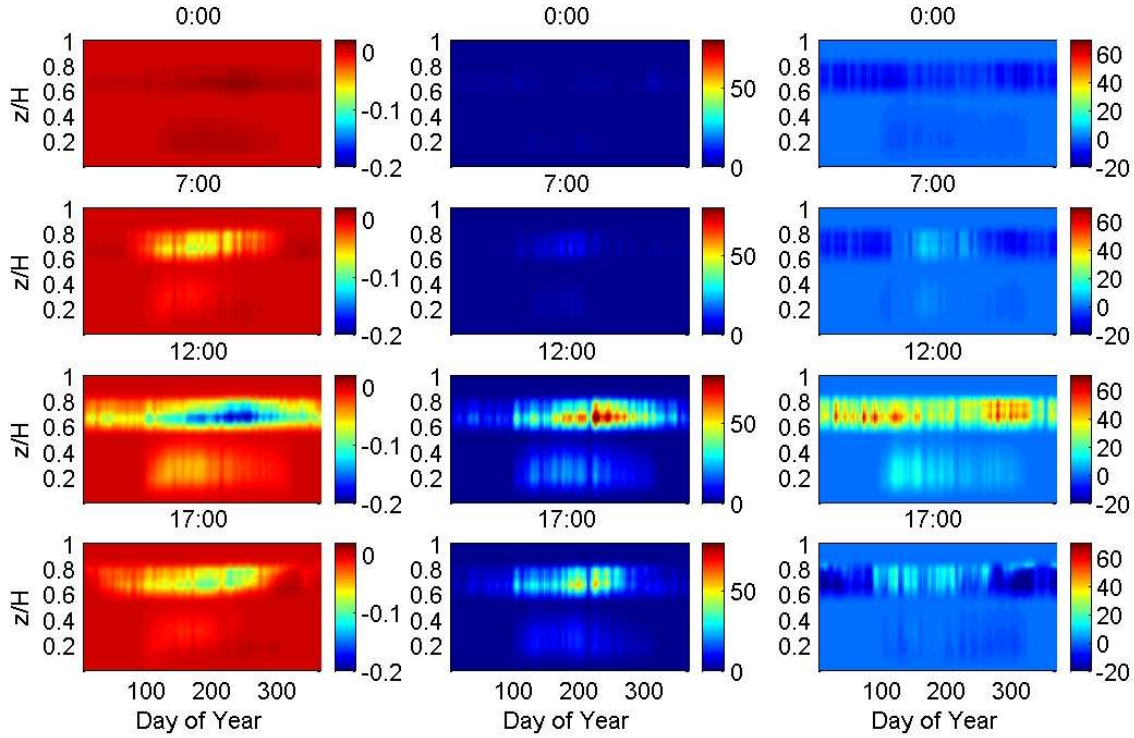

Figure 14: The time-depth distributions of modeled CO_2 sink/source strength (mgC m^{-3} s^{-1}, left column), latent heat source strength (W m^{-3}, middle column), and sensible heat source/sink strength (W m^{-3}, right column) at different times of day and different days of the year for 2005. All the results shown here use the second-order closure model with atmospheric stability corrections.

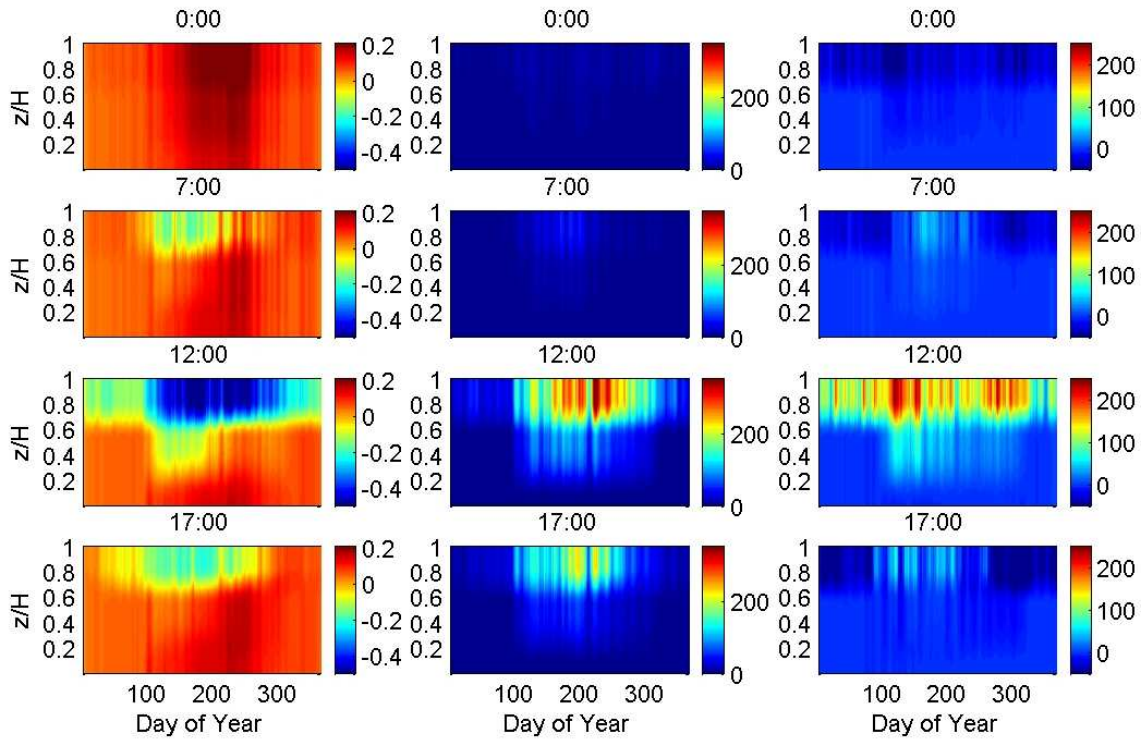

Figure 15: The time-depth distributions of CO_2 fluxes (mgC m^{-2} s^{-1}, left column), latent heat fluxes (W m^{-2}, middle column), and sensible heat fluxes (W m^{-2}, right column) at different times of day and different days of the year for 2005. All the results shown here use the second-order closure model with atmospheric stability corrections.

3.4.4 Comparison between different closure approximations

Figure 16 shows the ensemble-averaged profiles of mean air temperature, mean water vapor concentration, and mean CO_2 concentration within the canopy volume for different closure approximations and over different time periods in year 2005. The well-mixed assumption and the scalar profile measurements are also shown. The comparisons in Figure 16 demonstrate that second- and third-order closure schemes best agree with the profile measurements for all three scalars. Furthermore, the analysis here suggests that there is no gain in predictive skills by increasing the closure order from 2 to 3 as these two model results are almost indistinguishable. The main differences are between these two higher-order closure schemes and first-order closure calculations. Table 6 summarizes the relative standard deviation (RSD, in percentage) when comparing different closure approximation to measurements. This data – model comparison, shown in Figure 16, suggest that higher order closure approximations are needed if accurate mean scalar concentration distributions inside the canopy are desired. The question of whether predictive skills of modeling sources (or sinks) and fluxes significantly improve because we are realistically resolving the 2-way interaction by increasing the order of the closure scheme is explored next.

Figure 17 shows the ensemble-averaged hourly comparisons for sensible heat and latent heat fluxes, and CO_2 fluxes at the top of canopy for the hierarchy of closure models (in year 2005). The model results, derived from the well-mixed assumption, are shown along with the measurements. Differences in nocturnal fluxes are very close among the

models (and between the data and the models), but during daytime conditions, differences among the models (and data) become significant. The relative standard deviations in Table 6 demonstrate that higher-order closure schemes perform significantly better than zeroth- and first-order closure models, especially for sensible and latent heat fluxes. Note that the slope of the modeled sensible heat flux switches sign earlier in the afternoon when using the well-mixed assumption. This early sign-reversal can have significant impact on models of convective boundary layer height and triggers of convective rainfall [*Juang et al.*, 2007a; *Juang et al.*, 2007b]. We explore next whether such differences inject flux biases at annual time scales.

Table 6: The average relative standard deviation (in %) for all model results when compared with the half-hourly eddy covariance and canopy scalar profile measurements. 'With stability' refers to model results that resolve the effects of atmospheric stability within the canopy.

	1st-order closure	2nd-order closure		3rd-order closure	
		With Stability	Without Stability	With Stability	Without Stability
Air Temperature profiles	16.3%	11.8%	14.3%	11.3%	14.0%
Water vapor concentration profiles	10.1%	5.6%	7.2%	6.0%	7.7%
CO_2 concentration profiles	21.5%	14.0%	16.7%	13.6%	16.0%
Sensible heat flux at top of canopy	12.3%	7.4%	10.0%	7.8%	10.3%
Latent heat flux at top of canopy	16.7%	11.2%	15.8%	11.8%	16.1%
Carbon flux at top of canopy	23.0%	17.7%	20.2%	17.4%	19.8%

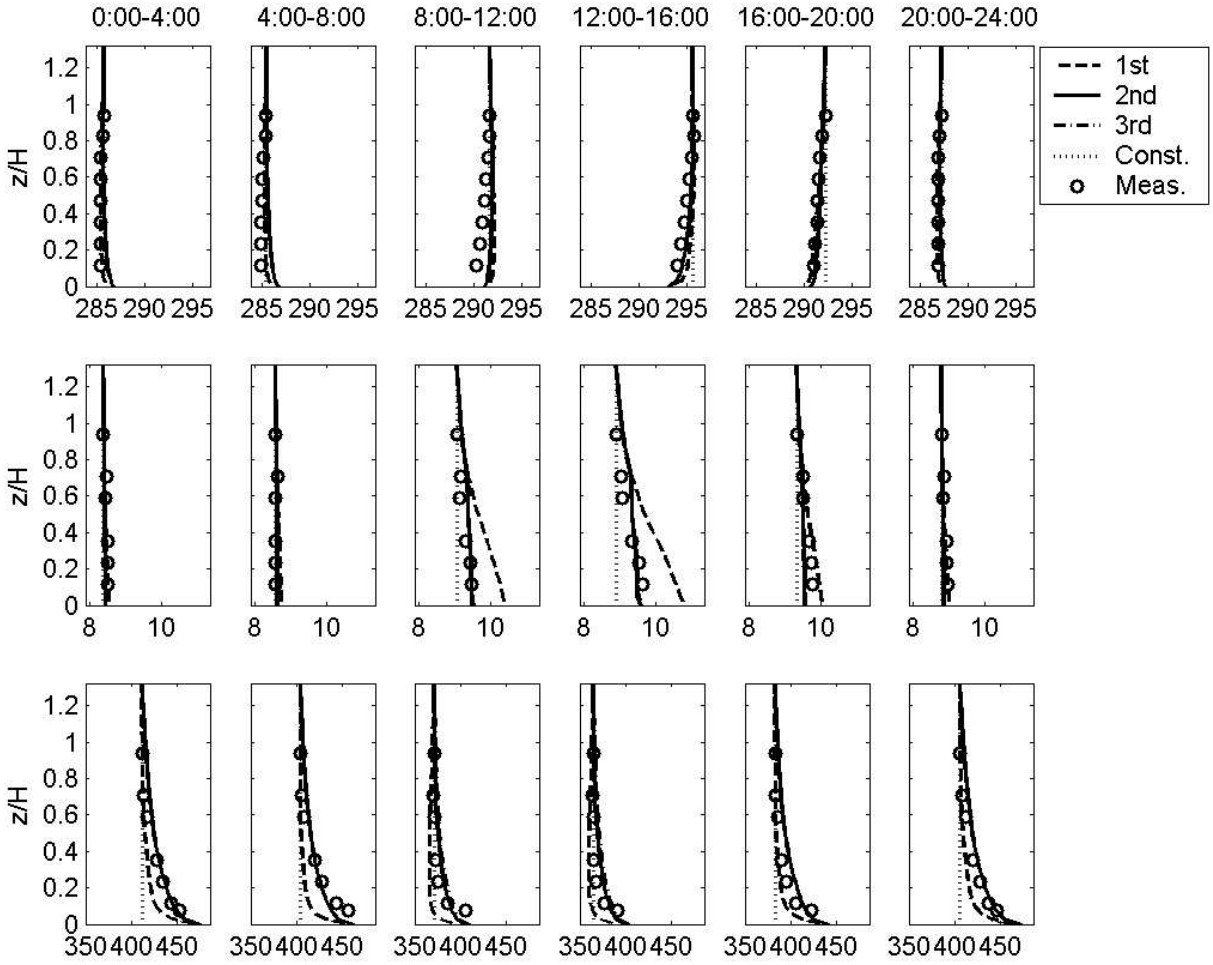

Figure 16: Ensemble-averaged profiles of mean air temperature (K, upper panel), mean water vapor concentration (g kg^{-1}, middle panel), and mean CO_2 concentration (ppm, lower panel) for different closure approximations over different times of day in 2005. All model results were derived using atmospheric stability corrections. Note that the model results for the second- and third-order closure are almost indistinguishable. Well-mixed conditions are shown as vertical dotted lines for reference.

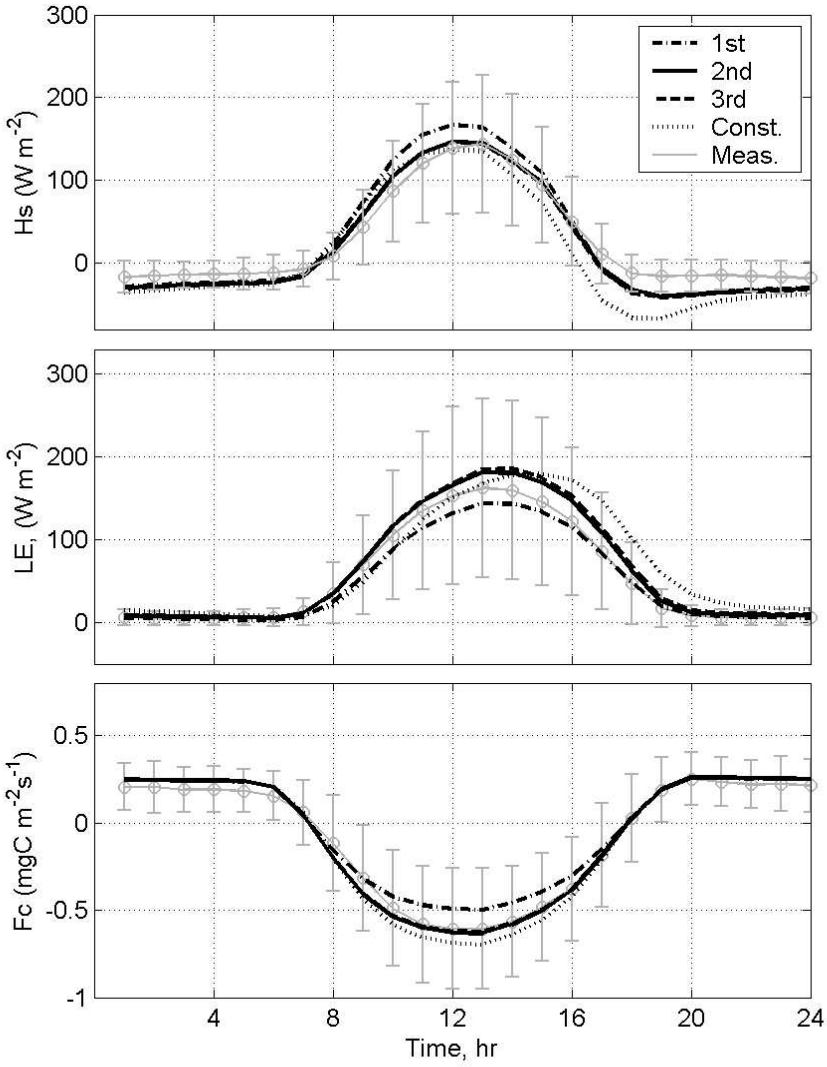

Figure 17: Comparisons between hourly ensemble-averaged measured (open circles) and modeled (lines) sensible heat flux (H_S), latent heat flux (LE) and carbon dioxide flux (F_C) at the top of the canopy in 2005. The model results were derived using different closure approximations (first-order to third-order) as well as the well-mixed assumption for scalars. Ensemble averaging was conduced across each hour of day in 2005. Vertical bars represent one standard deviation around the ensemble-averaged eddy covariance measurements.

3.4.5 Estimations of Annual NEE and ET

The main objective here was to explore how the 2-way interaction between leaves and their microenvironment affects ecosystem annual net ecosystem CO_2 exchange (NEE) and evapotranspiration (ET), and whether this 2-way interaction is as important as seasonality in key physiological parameters. From previous discussions, we showed that the second-order closure scheme optimally reproduces the mean scalar concentration (and temperature) profiles and fluxes; its predictive skills are also comparable to the computationally more-expensive third-order closure scheme. Hereafter, the second-order closure model with atmospheric stability corrections is used as a 'reference model' for the 2-way interaction between leaves and their microenvironment.

$V_{\mathrm{cmax},25}$ is known to vary for a number of reasons including temperature acclimation, and leaf nitrogen changes. Detailed leaf-level physiological measurements reported by Ellsworth (1999) and inverse-model calculations reported in Juang et al. (2006) suggest that seasonal variations in $V_{\mathrm{cmax},25}$ are approximately sinusoidal with an amplitude of 18 % . Thus

$$\frac{V_{\mathrm{cmax},25}}{\text{mean } V_{\mathrm{cmax},25}} = 0.18 \ \sin\left[2\pi\left(\frac{\text{day of a year-120}}{365}\right)\right], \tag{3-21}$$

well-approximates the seasonal variations at this site for the pine canopy. We compare the annual NEE (from 2001 to 2005) between the model results with 'static' $V_{\mathrm{cmax},25}$ (= to the mean value) and the sinusoidal-varying $V_{\mathrm{cmax},25}$ in Figure 18. Although

differences in annual NEE values between these two model results are small ($< 5\%$), some differences in the patterns at different times of year are discernable. For our purposes, the effect of non-stationarity in $V_{cmax,25}$ on annual NEE fluxes appears relatively small (because of partial cancellations) – at least when compared to biases introduced by using the well-mixed assumption.

Figure 18 also compares model results derived from the well-mixed assumption with the EC measurements for the years 2001-2005. While we show the comparisons for all 5 years, we limit our discussion to the wet years (2001, 2004, and 2005) and note again that year 2002 experienced a severe drought during the entire growing season (resulting in leaf area reduction in the pine stand), and the forest floor respiration in 2003 was dramatically different because of excess branches and litter from the ice storm in December of 2002. It suffices to say that annual NEE was overestimated in years 2002 and 2003 for these two reasons, as expected. However, because the forest floor evaporation is much less sensitive to increased respiring biomass in 2003, good agreement between ET predictions and EC measurements were observed, in contrast to the poor agreement between EC-measured and modeled NEE.

Figure 18 also suggests that (i) the zeroth-order model always predicted higher annual NEE (~6.6%) and ET (~8.3%) when compared to the second-order closure model, and this overestimation appears larger than the annual flux adjustments obtained by resolving the 18% amplitude variation in $V_{cmax,25}$.

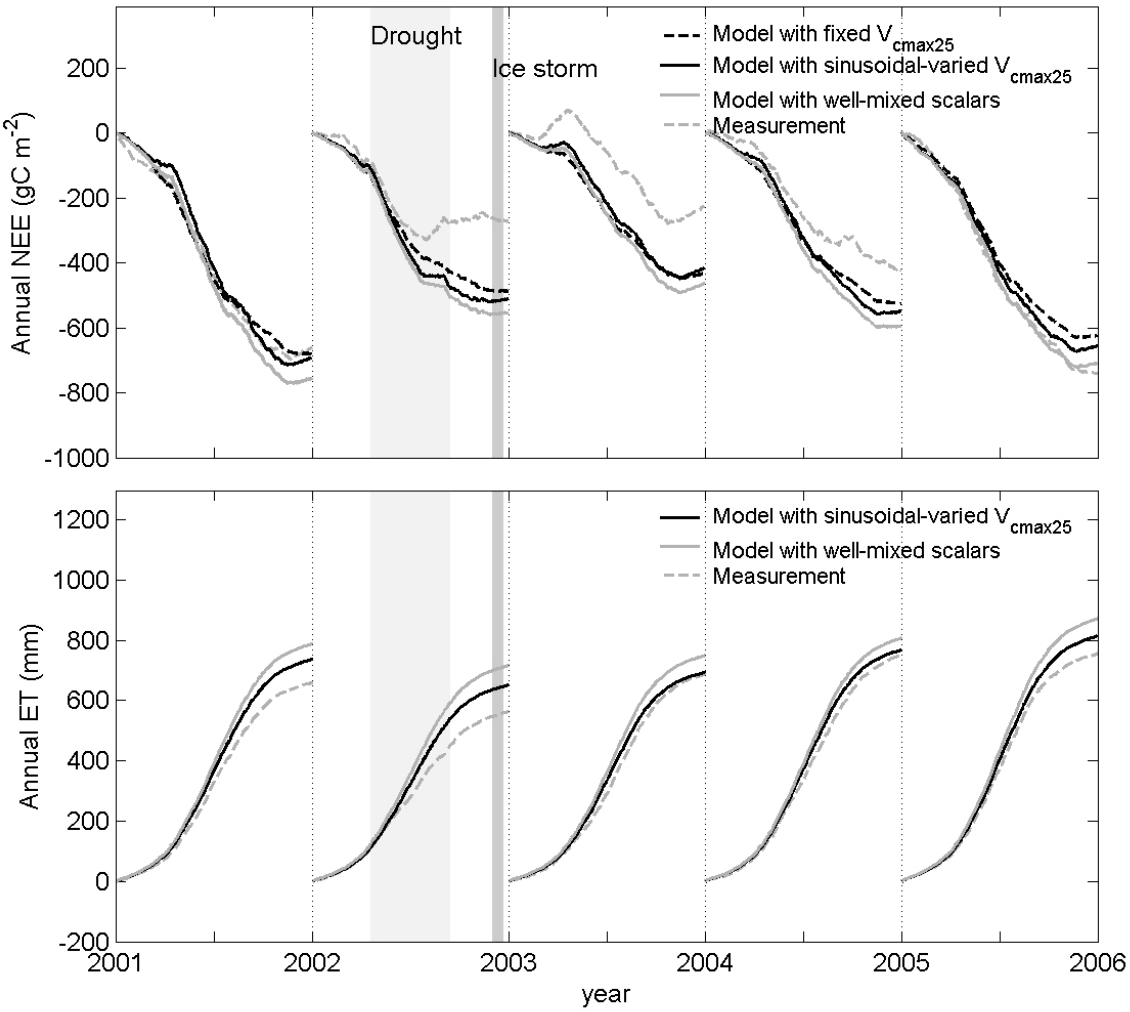

Figure 18: The comparisons of annual net ecosystem exchange (NEE, upper panel) and annual evapotranspiration (ET, lower panel) between the model results with fixed $V_{c\max,25}$, the model results with sinusoidal-varied $V_{c\max,25}$, the modeled results assuming well-mixed scalars inside the canopy, and the eddy-covariance measurement from 2001 to 2005. Note that the model assumes the canopy has adequate access to soil water and was not designed to capture the severe drought effects in 2002.

3.4.6 The effect of the atmospheric stability

Having demonstrated that the two-way coupling between the vegetation and its microenvironment is well reproduced by the second-order closure model, we explore next whether non-adiabatic simplifications to it may be sufficiently adequate. According to the field experiment in a deciduous forest at Camp Borden in Canada reported by Shaw et al. [1988], the effect of the thermal stratification on the flow statistics is as important as the effect of the leaf area index. Recall that resolving adiabatic conditions requires an iterative scheme for every 30-minute run because the velocity and scalar transfer equations must be simultaneously solved. A non-adiabatic simplification permits us to 'de-couple' the generation of the flow field from the scalar transfer calculations, as was done by Baldocchi [1992]; Baldocchi and Meyers [1998]; and Lai et al. [2000a; 2000b] in their Lagrangian simulations.

Table 6 summarizes the model-data comparisons when considering the effects of atmospheric stability and when neglecting them. Accounting for atmospheric stability improves the modeled relative standard deviations by 10% to 25% for mean scalar concentration (and temperature) profiles and turbulent fluxes at the top of the canopy. The effect of atmospheric stability on annual NEE and ET are also explored in Figure 19. The annual NEE comparisons suggest that assuming a neutral atmosphere degrades the modeled NEE by roughly 12 % to 15 %. For the annual ET, the model degradation is between 9 to 13 %. Hence, atmospheric stability corrections can improve model performance by about 10% or more, on average.

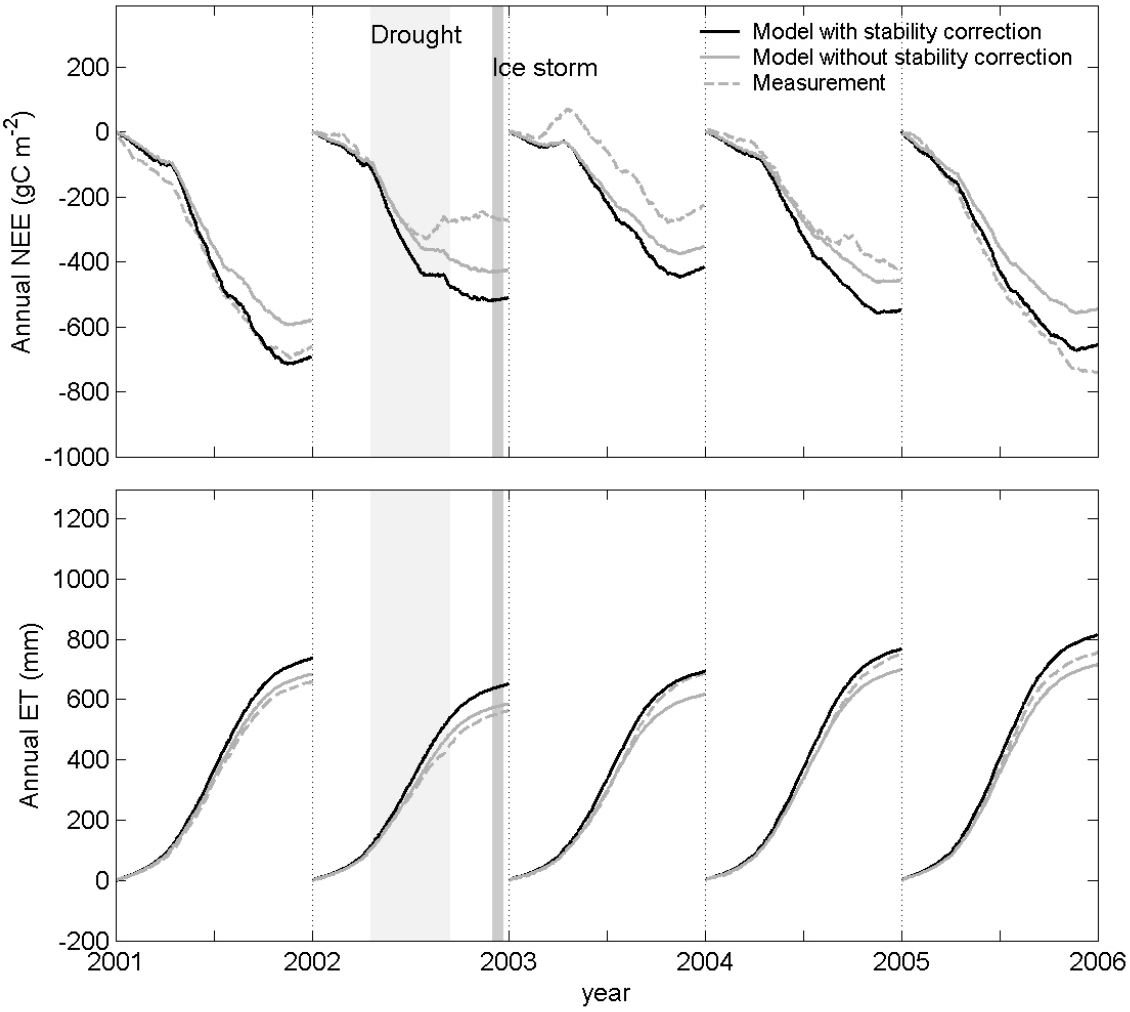

Figure 19: The comparisons of annual net ecosystem exchange (NEE, upper panel) and annual evapotranspiration (ET, lower panel) between the model results with stability corrections, model results without stability corrections, and the eddy-covariance measurements from 2001 to 2005.

3.5. Summary and Conclusions

The study objectives sought answers to two inter-related questions via model calculations and long-term measurements of mean scalar concentration and temperature profiles and eddy-covariance scalar fluxes above the canopy. These questions were (i) how detailed must the turbulent transport model be to resolve the 2-way interaction between leaves and their microclimate? and (ii) what were the predictive skills gained by resolving this 2-way interaction vis-à-vis correcting for seasonality in key physiological parameters (chosen here as $V_{cmax,25}$)? To address the first question, we used a hierarchy of turbulent models ranging from zeroth-order (well mixed assumption) to third-order closure. To address the second question, we conducted model calculations using a non-stationary $V_{cmax,25}$ and compared these model calculations with a constant $V_{cmax,25}$ case (though both cases have the same annual mean $V_{cmax,25}$). We found that:

(1) First-order closure modeling captured much of the scalar source-sink variations within the canopy as well as scalar fluxes above the canopy (to within 15%); however, second-order closure models were necessary to reproduce the mean scalar concentration (and temperature) profiles within the canopy (to within 8-15%).

(2) Third-order closure models perform no better than their second order counterparts in terms of overall predictive skills for scalar concentration profiles and fluxes, though they were computationally much more expensive.

(3) The flux most sensitive to the well-mixed assumption was sensible heat with a clear bias in the afternoon periods. This bias (and its timing) can have important consequences when modeling boundary-layer development and estimating triggers of convective rainfall (Juang et al., 2007a,b).

(4) The comparison between measured and modeled annual NEE and ET using static- and dynamic- $V_{cmax,25}$ do not show significant differences (~5%). However, for shorter integration periods (e.g., one month or one season), the CO_2 flux can be sensitive to variations in $V_{cmax,25}$. This conclusion may not be general for all forest species, but indicative that seasonal perturbations of *ca* 20% around the annual mean in physiological parameters do not bias mean annual fluxes; however, assuming a well-mixed concentration (and temperature) can bias annual fluxes in this forested ecosystem by more than 5%.

(5) Changes in near-surface atmospheric stability can have significant effects (10 to 20%) on the scalar concentration profile distributions and scalar flux estimates at the top of the canopy. The calculation of annual NEE and ET suggest that assuming a non-neutral atmosphere can be more important than resolving the 18% amplitude variation in $V_{cmax,25}$ for this ever-green forest, as long as the mean $V_{cmax,25}$ is not biased.

4. Hydrologic and Atmospheric Controls on Initiation of Convective Precipitation Events

4.1 Background and Introduction

The Southeastern United States (SE)[1] timberland ecosystems are among the most productive in North America and act as an important carbon sink within the continental United States [*Houghton et al.*, 1998; *Schimel*, 1995; *Tans and White*, 1998]. This high productivity is attributable to the moderate climate (mean annual temperature ~ 15.5 ^{o}C) and to the ample precipitation during the growing season (~ 95 mm month^{-1} from April to September). In a recent land-use assessment, the United States Department of Agriculture (USDA) estimated that the timberland cover of the SE ecosystems over the past half century (since 1953) experienced minor fluctuations (~ ±3.1% with a minimum of 793 thousand km^2 in 1989 and a maximum of 845 thousand km^2 in 1956), and currently represents ~ 48% of the SE landcover area [*Wear and Greis*, 2002]. However, the composition of the timberland cover is undergoing significant changes. For example, planted pine ecosystems comprised ~ 30% of the combined pine plantation and upland hardwood forest area in 1995, a ratio expected to increase to 50% in 2040 [*Wear and Greis*, 2002]. The precipitation mechanism likely to be impacted by such land cover change is convective precipitation because of its sensitivity to the local land-atmosphere heat and moisture exchange rates. To date, the implications of such projected land cover

[1] In this study, the SE includes the states of Alabama, Arkansas, Florida, Georgia, Louisiana, Mississippi, North Carolina, South Carolina, Tennessee, Virginia and the eastern part of Oklahoma and Texas. This definition is consistent with Findell and Eltahir [2003a; 2003b]. However, this region is classified as the "Southern Region" by United States Department of Agriculture (USDA) [*Wear and Greis*, 2002].

change on precipitation patterns in this region remain a vexing problem because of the numerous nonlinear feedback mechanisms between soil moisture content and the atmospheric state, though several model results and field experiments are beginning to offer preliminary clues [*Atlas et al.*, 1993; *D'Odorico and Porporato*, 2004; *Findell and Eltahir*, 2003a; *Giorgi et al.*, 1996; *Pan et al.*, 1996; *Trenberth and Guillemont*, 1996].

Using model simulations based on coupling the convective triggering potential index (CTP) with the low level humidity index (HI_{low}), Findell and Eltahir [2003a; 2003b] concluded that the feedback between soil moisture and subsequent convective precipitation in the SE region is positive, meaning that subsequent convective precipitation events are highly correlated to wet soil moisture states in the early morning hours and to high evapotranspiration during the morning and early afternoon.

Field experiments at a shallow-rooted SE planted loblolly pine forest suggest that pine ecosystems can be highly sensitive to episodic short-term droughts [*Oren et al.*, 1998]; long-term sap flow measurements in a loblolly pine plantation showed that a decrease in volumetric soil moisture content within the root-zone (θ) from 0.20 to 0.14 reduces their transpiration rate (T_r) by a factor of 3 [*Oren et al.*, 1998]. When this sensitivity of T_r to θ is placed within the context of the projected increase in pine-plantation area, the positive feedback alluded to in Findell and Eltahir [2003a; 2003b] may be significantly disrupted by episodic droughts.

A starting point to explore such interactions between soil and atmospheric water states is to investigate the interplay between the triggers of convective precipitation and environmental factors in a region whose T_r is known to be sensitive to θ. To characterize how this interplay could be altered by the land-use change, we conduct this investigation in a SE landscape that is composed of different land cover types yet experiences the same climatic, hydrologic, and edaphic conditions. The minimal environmental factors to be analyzed must involve θ, ambient atmospheric relative humidity (RH), and the physiological controls on land-surface energy budget (i.e., sensible/latent heat fluxes). We investigate this interplay by combining a long-term half-hourly precipitation record, measured sensible heat flux from eddy-covariance monitoring systems in this mosaic, ambient mean air temperature and relative humidity, and nearby early morning sounding profiles representing the upper atmospheric properties. Even within this restricted scope, numerous simplifications must be invoked to separate convective precipitation from other precipitation patterns and to track its dependence on antecedent θ and RH.

To accomplish this objective, we limited our analysis to periods spanning late spring to early fall (May to September, Julian day 121 to day 273), which is defined here as "summertime". This is roughly the period when the leaf area index (LAI) is either at or approaching its maximum value thereby providing some basis to investigate the effects of ecophysiological controls on convective precipitation events [*McCarthy et al.*, in preparation].

The analysis was organized as follows: we first developed a simplified model to stratify the long-term measured precipitation record into convective and non-convective conditions. We then analyzed the statistics of convective precipitation with respect to their non-convective counterpart to assess their overall contribution to growing-season precipitation during the study period. Next, the statistics of convective precipitation for different combination of θ and RH regimes are considered. Particular attention was devoted to whether the statistics of convective precipitation triggered by dry water states (low θ and low RH) differ from their moist counterparts. We restricted our research area to a local-scale SE mosaic landscape composed of three different vegetated land cover types, and the analysis was conducted using an effective area-averaged measurements. Hence, this analysis did not explicitly consider the heterogeneity or clustering of the vegetation within the landscape, which when it exits at sufficiently large scales (5-50 km), can alter the exchange of water between the surface and atmosphere and influence the onset of the fraction of low cloud cover, area-averaged cloud amount [*Wetzel*, 1990] and the precipitation patterns.

4.2 Experimental site and measurements

Much of the site and experimental setup are described elsewhere [*Novick et al.*, 2004; *Palmroth et al.*, 2005; *Stoy et al.*, 2005]; however, the salient points are repeated for completeness.

The data used here were collected at the Blackwood Division of the Duke Forest near Durham in North Carolina (35°58'N, 79°05'W, 163 m above sea level) as part of FluxNet, an on-going global long-term CO_2 flux monitoring initiative [*Baldocchi et al.*, 2001]. The local topographic variations are small (slope $< 0.5\%$) such that the effect of the complex terrain on the micrometeorological measurements can be ignored [*Siqueira et al.*, 2002]. The soil type is acidic Hapludalf with a clayey loam (Enon silt loam) in the upper 0.3 m above a clay layer, which extends to bedrock at ~ 0.7 m (Soil Survey of Orange County, North Carolina 1975). The saturated soil moisture content within the rooting zone is 0.54 m^3 m^{-3} [*Oren et al.*, 1998]. Using data collected from a nearby weather station (Chapel Hill 2 E, location: 35°55'N / 79°05'W, 156.1m above sea level), the long-term (from 1948 to 2004) mean annual precipitation is 1185 ± 177 mm, and the annual mean air temperature is 14.9 ± 0.9 °C.

This site comprises three different major land cover types: an abandoned old-field covered with grass and herbaceous species (OF), a 22-year-old (in 2005) maturing loblolly pine (*Pinus taeda*) forest (PP), and an 80 to 100-year-old mature oak-hickory (*Quercus* and *Carya* species) deciduous hardwood forest (HW). These three land cover

types represent a typical land-use sequence after abandonment of agricultural fields in the piedmont region of North Carolina [*Oosting*, 1942]. The OF and PP sites were established after a clear-cut and burn in 1979 and 1983, respectively. The OF site is mowed regularly every year to prevent the encroachment of woody species. At the PP site, the pine seedlings were planted at 2 m × 2.4 m spacing in 1983. The characteristics of the experimental site and each land cover are summarized in Table 7.

This region experienced a mild drought event in 2001 and a severe drought event in 2002 during the growing season. The 2001 to 2004 growing season precipitation records nearly covered the wettest and driest states within the past 57-year on record (see Figure 20a), thereby providing a wide range of soil moisture and air relative humidity conditions. Figure 20b shows the distributions of θ in each land cover from 2001 to 2004, and suggest that higher θ values were more frequently observed in the HW site than the other two ecosystems. In Figure 20b, the solid line shows the ensemble area-weighted (see discussion in Section 4) averaged distribution of θ from the three land covers, and the vertical line of $\theta = 0.2$ m^3 m^{-3} approximately represents the mode of this ensemble distribution for the dry soil condition.

Satellite multi-spectral data (IKONOS satellite, Space Imaging, Thornton, CO, USA) were acquired at 4 m × 4 m spatial resolution to analyze the composition of the land cover and to characterize the dominant vegetation in the vicinity of the study site. A 10 km × 10 km area (Figure 21) around the study site (red rectangular region in Figure 21) acquired on September 23rd in 2004 was chosen to determine the dominant land-cover

likely to impact triggers of convective precipitation. This area is sufficiently larger than a typical convective cell [*Stull*, 1988]. Applying the parallelepiped algorithm [*Detto et al.*, 2006; *Richards*, 1999], the normalized difference vegetation index (NDVI) was computed from surface reflectance averaged over the spectral wavelengths from visible red to near infrared regions, and the surface vegetation cover was then stratified. The color map in Figure 21 shows the spatial distribution of four different land covers in the 10 km $\times$ 10 km area around the study site. From this analysis, the fraction of pine forest, hardwood forest, grass, and other land cover types (e.g., road and residential areas) are 33.3 %, 41.6 %, 16.8 %, and 8.3%, respectively. This composition is used to derive area-weighted quantities of all the model parameters as described in Section 4.

The long-term environmental and land-surface flux data were sampled above each ecosystem (see Figure 21). The half-hourly tipping bucket precipitation, mean air temperature, mean air relative humidity, incident shortwave radiation, and eddy-covariance measured sensible and latent heat fluxes were all collected above each canopy type. The volumetric soil moisture content within the rooting-zone (the top 0.3 m region) was measured around each tower.

In addition to the long-term measurements collected at the Duke Forest, the upper atmospheric characteristics were determined from early morning sounding data sampled at a nearby airport and were used to determine the lapse rate needed to determine the boundary layer dynamics described next.

Table 7: The site description for each ecosystem and a summary of the setup at the Blackwood Division of the Duke Forest near Durham, North Carolina.

Site	PP	HW	OF
Land-cover type	Planted pine	Hardwood forest	Old-field grassland
Dominant Canopy Species	*Pinus taeda* L. with few *Liquidambar styraciflua* L.	Composed of *Liriodendron tulipifera* L., *Quercus alba* L., *Q. michauxii* Nutt., *Q. phellos* L., *L.styraciflua* L., and *Carya* ssp.	C_3 grass *Festuca arundinaria* Shreb with few other C_3 herbs and C_4 grass
Age / Management	22 years (since 1983)	80-100 years	Mowed once or twice per year (since the clear-cut in 1979)
Canopy height	18.0 m	25.0 m	0.1 to 1.0m
Leaf area index	2.5-5.5 m^3m^{-3}	0.2-7.0 m^3m^{-3}	1.0-3.0 m^3m^{-3}
Tower height	22.2 m	41.8 m	4.8 m
Eddy-Covariance system height	20.2 m	39.8 m	2.8 m
Soil moisture measurement	24 sensors	12 sensors	6 sensors

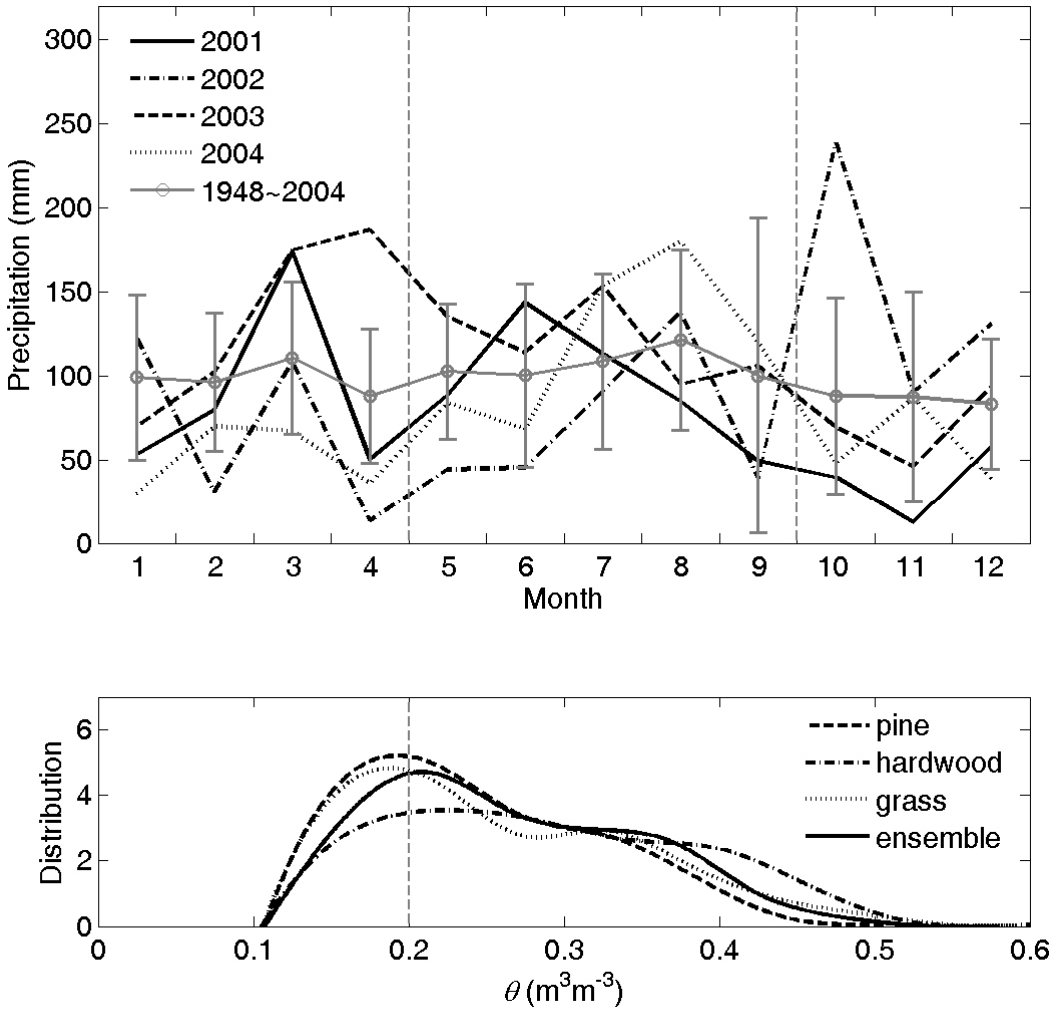

Figure 20: The time variation of ensemble-averaged monthly precipitation (upper panel) and the probability density function (pdf) of θ (lower panel) for each vegetation cover from 2001 to 2004. The area-weighted ensemble soil moisture PDF is also shown for reference.

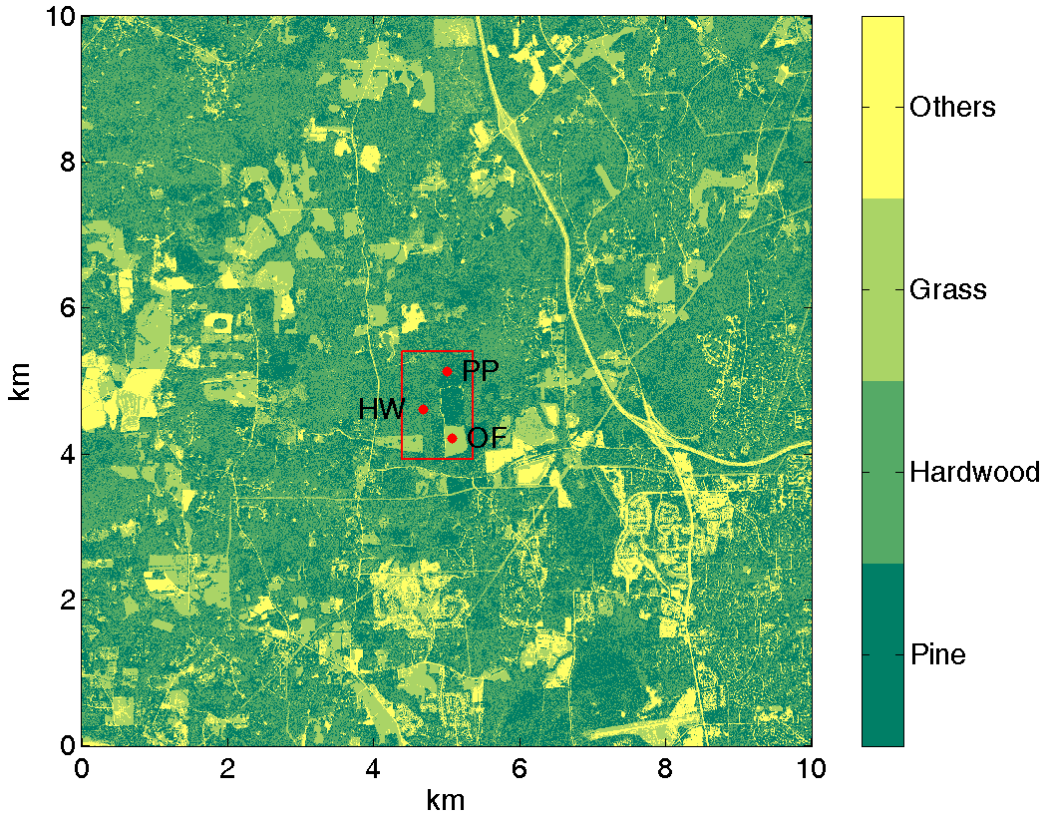

Figure 21: Composition of different vegetation cover from the IKONOS image (4 m × 4 m spatial resolution) in the vicinity of the Blackwood Division of Duke Forest (the area within the red rectangular region). The image was acquired on Sept. 23, 2004. The walkup towers with long-term monitoring systems at all 3 different ecosystems are marked as red dots.

4.3. Data Analysis

To address the study objective, we developed a methodology to conditionally sample summertime convective precipitation from the long-term precipitation record measured by a tipping bucket gauge. The conditional sampling scheme utilized a simple slab model to determine the evolution of both the mixed-layer height (z_i) and the lifting condensation level (H_{LCL}). The dynamics of z_i is mainly driven by the measured surface sensible heat flux, and the value of H_{LCL} is determined from the measured near-surface air temperature, air humidity, and atmosphere pressure. The convective precipitation events from the long-term record were identified by checking whether modeled z_i intersects modeled H_{LCL} just prior to the observed rainfall event (see Section 4) thereby marking this event as convective. Next, we briefly describe how z_i, H_{LCL}, and the identification scheme are implemented.

4.3.1 Mixed-layer height evolution

To determine the temporal evolution of the mixed-layer height (z_i), the entire mixed-layer is treated as a single slab that has a mean slab potential temperature $\overline{T_p}$, where over-bar represents the temporal averaging operator over turbulent fluctuation (30 min in this study). By ignoring the heat source/sink terms within the slab volume and

adopting a standard encroachment assumption [*Garc et al.*, 2002; *Stull*, 1976; 1988], the integrated one-dimensional continuity equation reduces to

$$\frac{dz_i}{dt} = \frac{\overline{w'T_p'}_s - \overline{w'T_p'}_{z_i}}{\gamma z_i}, \tag{4-1}$$

where $\overline{w'T_p'}_s$ and $\overline{w'T_p'}_{z_i}$ individually represent the turbulent sensible heat fluxes at the surface and at the top of the mixed-layer, γ is the local lapse rate of $\overline{T_p}$ just above z_i, and the primed quantities denote turbulent excursions around their time-averaged values.

As earlier stated, the surface sensible heat flux $\overline{w'T_p'}_s$ is directly measured from the eddy-covariance system for each land cover and then aggregated using an area-weighted scheme; however, the lapse rate γ and the entrainment flux $\overline{w'T_p'}_{z_i}$ are additional unknowns that require further parameterizations.

4.3.2 Determination of lapse rate (γ) and entrainment flux ($\overline{w'T_p'}_{z_i}$)

We used the daily upper-air sounding profiles at Piedmont Triad International Airport (GSO, 36°05'N, 79°57'W, 270 m above sea level and 79 km west of the Duke Forest) to estimate the value of γ. The sounding data is maintained by the Department of

Atmospheric Science at University of Wyoming, and is collected at 0000 UT (local time 0700 LT) and 1200 UT (local time 1900 LT) every day. We estimated the early morning lapse rate γ at the top of the mixed-layer from the mean value of the potential temperature profile at 0700 LT between the height of 50 m and 400 m from 2001 to 2004. Figure 22 shows the ensemble value of the sounding profiles and the resultant mean $\gamma = 11.6 \times 10^{-3}$ °C m^{-1}. This estimate is about 18% larger than the dry adiabatic lapse rate, given by $g / C_p = 9.76 \times 10^{-3}$ °C m^{-1}, where $g = 9.81$ m s^{-2} is the gravitational acceleration, and $C_p \sim 1005$ J Kg^{-1} °C^{-1} is the specific heat capacity of dry air at constant pressure.

As for the estimate of the entrainment flux from the top of the mixed-layer, $\overline{w'T_p'}_{z_i}$, we adopt the standard parameterization used in encroachment models: $\overline{w'T_p'}_{z_i} = -\beta \, \overline{w'T_p'}_{s}$ [*Tennekes*, 1973].

Although the value of β changes with time of day, several numerical studies and measurements suggest that β is constrained between 0.2 and 0.4 [*Betts et al.*, 1992; *Kim and Entekhabi*, 1998]. Here, we assumed the value of β to be 0.3 taken from *Kim and Entekhabi* [1998]. With $\beta = 0.3$ and $\gamma = 11.6 \times 10^{-3}$ °C m^{-1}, the dynamics of z_i can now be predicted only from the time series of measured surface sensible heat flux $\overline{w'T_p'}_{s}$.

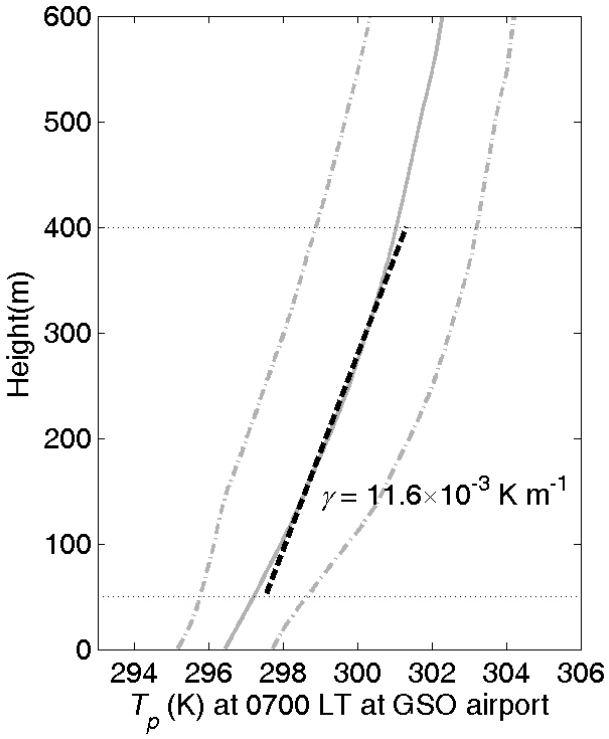

Figure 22: The ensemble profiles of potential temperature from 1998 to 2004 collected at the Piedmont Triad International Airport (GSO). The solid line shows the mean value, the dot-dashed lines are one standard deviation from the mean, and the bold dashed line is the mean lapse rate determined between 50 m and 400 m.

4.3.3 Lifting condensation level

The lifting condensation level is determined from,

$$H_{LCL} = \frac{R T_a}{M_a g} \log\left(\frac{P_s}{P_{LCL}}\right), \tag{4-2}$$

where $R = 8.314$ J mol^{-1} °C^{-1} is the universal gas constant, M_a is the molecular weight of the air (~ 29 g mol^{-1}), P_s (kPa) is the atmospheric pressure at the surface, and P_{LCL} (kPa) is the atmospheric pressure at H_{LCL}. The value of P_{LCL} can be approximately determined from the hydrostatic assumption, given by

$$P_{LCL} = P_s\left(\frac{T_{LCL}}{T_a}\right)^{3.5}, \tag{4-3}$$

where T_{LCL} (K) is the saturation point temperature at H_{LCL}. The quantity of T_{LCL} can be derived from the Clausius-Clapeyron equation [*Stull*, 1988] as,

$$T_{LCL} = \frac{2840}{3.5\ln(T_a) - \ln\left(\frac{P_s r}{0.622 + r}\right) - 7.108} + 55, \tag{4-4}$$

where r is the near-surface atmospheric water vapor mixing ratio calculated from the near-surface mean air relative humidity (RH), and the parameter 3.5 is given from the inverse of the Poisson constant.

4.3.4 Initial conditions

Numerical integration of Equation (4-1) commences at sunrise and is terminated at sunset or when the mixed-layer height intercepts the lifting condensation level (i.e. $H_{LCL} = z_i$). The sunrise (when $t = t_0$) and sunset are determined from the solar zenith angle, which vary with time of day and location.

The initial mixed-layer height $z_i(t_o)$ must also be specified each day. To derive this initial value, nighttime-averaged friction velocity $\langle \overline{u_*} \rangle$, and the nighttime-averaged surface sensible heat flux ($\langle \overline{w'T_p'}_s \rangle$) are employed in the equilibrium model by *Zilitinkevich* [1972]:

$$z_i(t_o) = 0.4\left(\frac{\langle \overline{u_*} \rangle}{f}\langle |L| \rangle\right)^{1/2}, \tag{4-5}$$

where the angle brackets represent the mean quantity averaged throughout the nighttime. The parameter 0.4 is a similarity constant [*Garratt*, 1992], f ~ 10^{-4} s^{-1} is the Coriolis parameter, and $\langle |L| \rangle$ is the average of the absolute value of the Obukhov length (L) derived from $\langle \overline{u_*} \rangle$ and $\langle \overline{w'T_p'}_s \rangle$:

$$\langle |L| \rangle = \frac{\langle \overline{T_a} \rangle \langle \overline{u_*} \rangle^3}{kg \langle \overline{w'T_p'}_s \rangle}, \tag{4-6}$$

Here, $z_i\left(t_o\right)$ is not permitted to drop below 40 m (arbitrarily chosen as double of the PP canopy height). We note that the model simulations are not overly sensitive to the choice of $z_i(t_o)$ because $z_i(t_o)$ is often <100 m while the mixed-layer height is expected to grow above 1000 m here.

4.4. Results and discussions

We used the 2001-2004 summertime (Julian days 121 to 273) record of sensible heat flux, soil moisture content, near surface air temperature, and near surface air relative humidity from each ecosystem to separate convective from non-convective precipitation. Because the region around the Duke Forest is composed of four major land-cover types (pine, hardwood, grassland, and others), yet the slab-model is zero-dimensional, a logical starting point is to consider an area-weighted contribution for each of the above variables to soil moisture and sensible heat flux. We ignored the contribution of the class "others" because it is a small fraction of the total area (~8.3%), and re-scaled the fractional cover of pine, hardwood and grassland to be 36 %, 46 %, and 18 %, respectively.

4.4.1 Identification of the convective precipitation events using the slab model

We conditionally sampled the days that are likely to induce convective precipitation events by considering periods that met the following four criteria:

1) The mean incident shortwave radiation R_i from 1100 LT to 1400 LT was greater than 600 W m^{-2} – a surrogate for eliminating days with large mid-day cloud cover

2) The area-averaged mean sensible heat flux $H_S = \rho C_p \overline{w' T_p{}'_s}$ (where ρ is the air density) from 1100 LT to 1400LT was greater than 100 W m^{-2} to ensure sufficient local heat is produced from the landscape

3) The atmospheric stability parameter $(-z/L)$ was large; namely $-z/L \geq 5$, for $z = z_i/2$ (i.e. set at the center of the slab volume) and is taken as the stability limit at which free convective turbulence dominates the mixed-layer volume under these conditions.

4) The slab model predicted the occurrence of convective precipitation events when $z_i = H_{LCL}$ during daytime conditions (i.e. between sunrise and sunset).

To assess the skill of the identification scheme at detecting convective precipitation events, we compared the time at which $z_i = H_{LCL}$ with the time at which the precipitation event was first detected by the tipping bucket gage. Figures 4a and 4b show an example of the dynamics of z_i, H_{LCL} and the corresponding time series of precipitation, RH and θ for moist (high RH and θ) and dry (low RH and θ) conditions, respectively. The effect of soil moisture content on the dynamics of z_i are evident: dry soil moisture content states induce a relatively deeper mixed-layer depth while moist soil moisture states induce shallow convective boundary layers. The comparison shown in Figure 23 also indicates that the model can predict the onset of convective precipitation reasonably well for a wide range of soil moisture states.

To quantify the overall slab-model 'detection' performance, we compared the predicted and measured convective precipitation timing for all the summertime convective precipitation events from 2001 to 2004 and found that this simple model predicted more than 92 % of the summertime convective precipitation events to occur within 1.5 hour of the observed precipitation timing (Figure 24, recall that the precipitation is measured at 30-minute intervals). Note that the pdf of the timing error is skewed toward the negative region. This indicates that the model tends to predict the onset of precipitation slightly earlier (the mean of the pdf curve in Figure 24 is –0.18 hours) than the observed timing. A plausible explanation is that after the mixed-layer height intersects the lifting condensation level, a few minutes to few hours may be required to form precipitation in some cases. Naturally, this condition $z_i = H_{LCL}$ predisposes, but does not necessarily lead to convective precipitation. When air parcels reach H_{LCL}, condensation forms in regions of negatively buoyant 'overshoots of mixed-layer thermals'. These thermals penetrate the capping inversion at z_i. If the overshoot is sufficiently strong to continue lifting the condensing air parcel, latent heat is released and its potential temperature becomes sufficiently warmer than its surroundings and it becomes positively buoyant. This height defines the 'level of free convection' (LFC). This parcel continues to buoyantly rise until it eventually becomes cooler than its surroundings at which point the 'limit of convective' rise (LOC) is attained. Any residual inertia in the parcel might propel it to continue rising further eventually stopping at the cloud top [*Emanuel et al.*, 1994; *Stull*, 1988]. Once clouds develop, condensation nuclei are required to allow rapid growth of water droplet. When these water droplets reach

sufficient size to precipitate and re-penetrate the unsaturated air below the cloud base without completely evaporating before reaching the ground surface, rainfall at the surface occurs. Roughly, after z_i intersects H_{LCL}, the entire process leading to precipitation detection at the ground may vary from minutes up to 2 hours [*Stull*, 1988]. This lag between the timing at which $z_i = H_{LCL}$ and the actual rainfall timing is a plausible explanation of the negative skewness shown in Figure 24. In fact, we did compare the relationship between H_{LCL} with the LFC under strong convective potential ($700 \text{ mb} < \text{LFC} < 850 \text{ mb}$) estimated from the sounding data at GSO airport for the years 2001 to 2004. The relationship suggests that the difference between LFC at GSO airport and the locally computed H_{LCL} is not large (difference = 34 ± 21 mb). This pressure difference is on the order of 150 m height that is likely to contribute to the skewness reported in Figure 24 assuming that the LFC at GSO airport is identical to the one above the study site.

We also examined the discriminatory skill of the model to distinguish between convective precipitation events (z_i intercepted by H_{LCL}) and non-precipitation conditions (z_i did not intersect H_{LCL}) when criteria (1)-(3) were applied (i.e. likely conditions to induce convective precipitation). The slab model correctly detected 86% of the non-precipitation conditions thereby lending confidence to our approach.

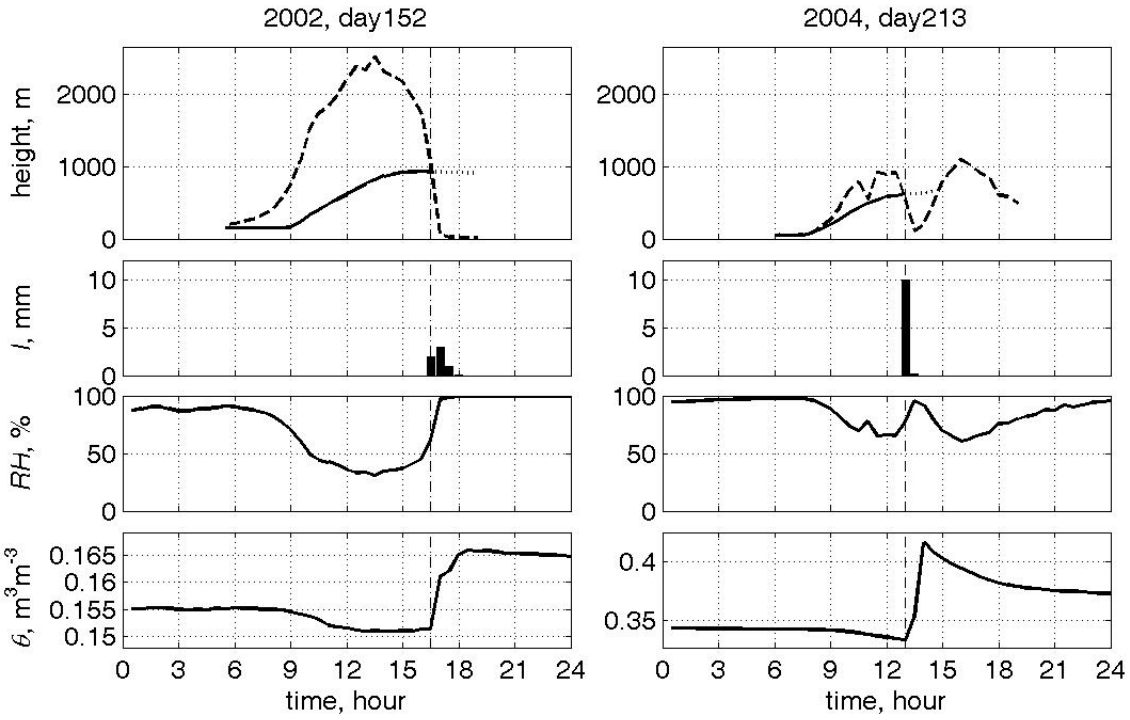

Figure 23: The modeled z_i (solid line) and H_{LCL} (dashed line), and the corresponding measured precipitation, RH and θ on day 152 of 2002 (left panel) and on day 231 of 2000 (right panels).

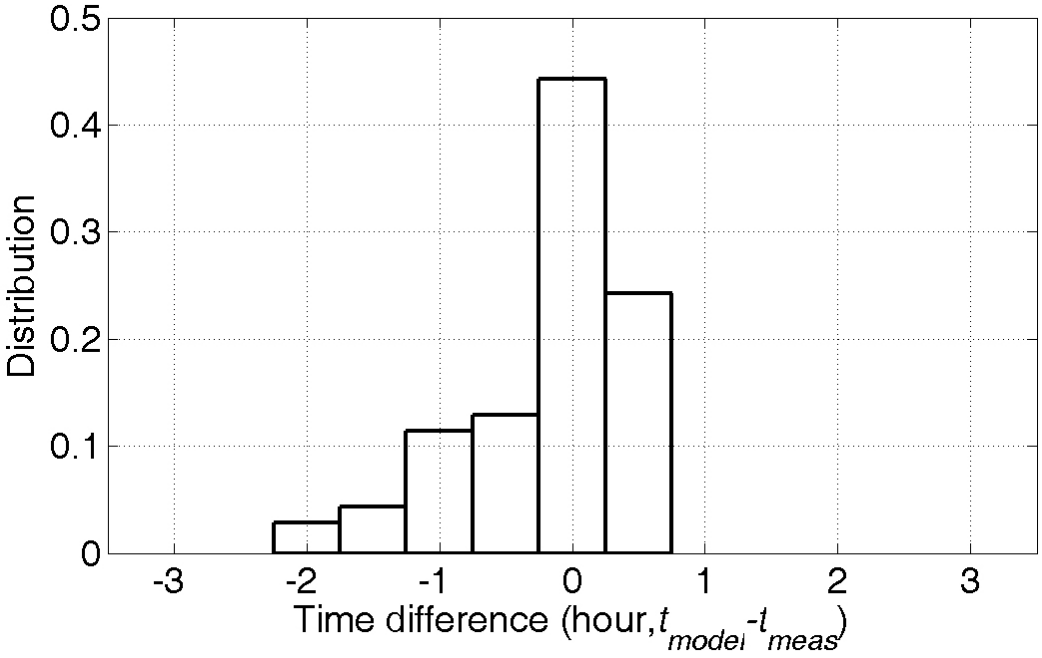

Figure 24: The probability density function of the onset time difference between modeled ($z_i = H_{LCL}$) and measured convective precipitation.

4.4.2 Statistics of convective vs. non-convective precipitation

Having identified the convective precipitation events in the precipitation time series, we analyzed their characteristics and contribution to summertime precipitation next. Specifically, we compared the probability density functions (pdf) of the half-hourly intensity for both convective and non-convective precipitation events (Figure 25).

The comparison shown in Figure 25 suggests that the convective precipitation events have heavier tails than the non-convective conditions. In fact, the precipitation intensity of the convective precipitation (mean $= 2.1$ mm per 30 min) is significantly larger than its non-convective counterpart (mean $= 1.1$ mm per 30 min). We also conducted a Kolmogorov-Smirnov significance test and found that these two pdf distributions in Figure 25 are statistically different at the 99 % confidence interval.

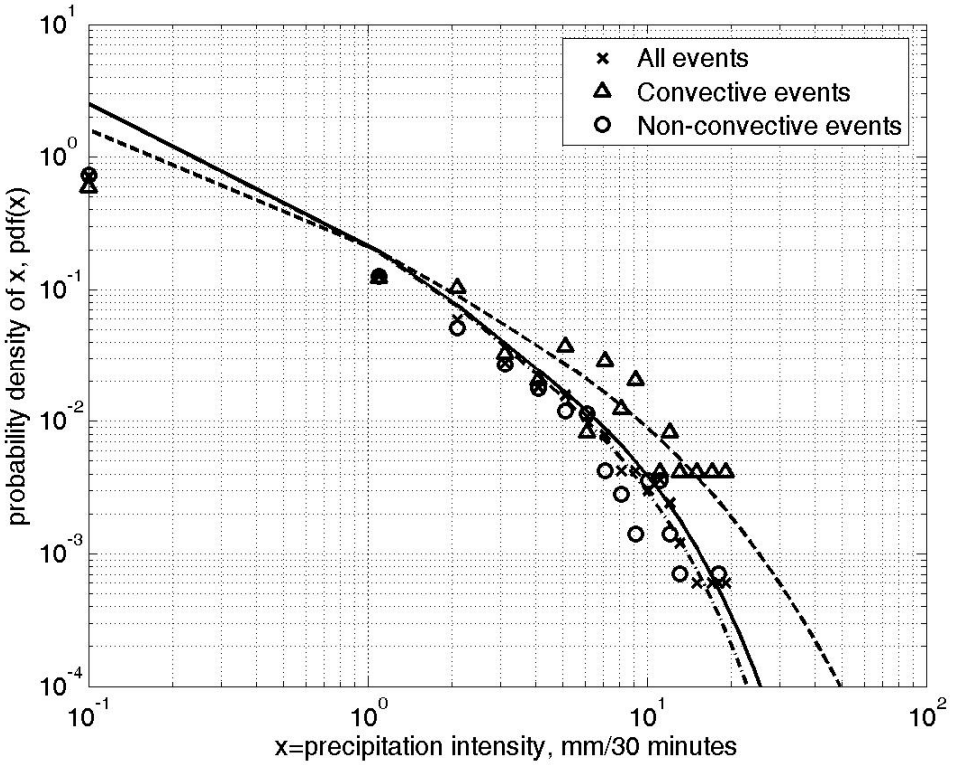

Figure 25: The probability density function of convective (triangles and dotted line) and non-convective (circles and dot-dashed line) precipitation events. The probability density function of all the sampled precipitation events (solid line) is shown for reference. The solid lines are best-fit regression to the data.

4.4.3 Soil-atmosphere water states and triggers of summertime convective precipitation

Now that properties for summertime convective precipitation events have been identified from the precipitation time series, we explore whether some preferential combination of water states both in the soil and the atmosphere could enhance the triggers of convective precipitation. Using the entire 4-year record, the area-averaged mean soil moisture content θ and the measured mean atmospheric relative humidity RH just prior to each convective precipitation event are shown in Figure 26. For reference, we also show the mean measured RH and θ between 1100 LT and 1500 LT from the entire 4-year record to show that the entire RH - θ plane is populated by climatic events. However, the dotted oblique line in Figure 26 represents a clear boundary below which convective precipitation was not observed and likely was not triggered given that the observation record included extremely moist and dry conditions in the region. The reason for the emergence of such 'excluded region' is that a relatively dry atmosphere results in very high H_{LCL} (up to 4000 m) while the relatively moist soil leads to lower sensible heat flux and lower mixed-layer heights. Hence, this 'excluded region' simply reflects the fact that the lifting condensation level in a dry atmosphere cannot intersect the top of the mixed-layer for moist soil conditions.

Applying a threshold $\theta = 0.20$ m^3 m^{-3} (dashed lines), the $RH - \theta$ plane shown in Figure 26 is further decomposed into two regions (moist and dry). The threshold $\theta = 0.20$ m^3 m^{-3} was chosen because it represents the 'dry' mode of the ensemble pdf of

θ shown in Figure 20b. The lower-left part of Figure 26 shows that conditions with dry soil moisture and dry atmosphere can induce convective precipitation events. An immediate consequence of the existence of precipitation events in the dry soil and dry atmosphere region is that negative feedbacks between soil moisture and subsequent precipitation in the SE region may exist.

To further investigate the characteristics for different soil water states, the pdf of the precipitation duration, maximum half-hourly intensity per event, total precipitation per event, and the mean precipitation intensity were compared separately for soil moisture content above and below $\theta > 0.20$ m^3 m^{-3} (Figure 27). Using the Kolmogorov-Smirnov test, we found that the distributions of precipitation duration of these two soil moisture condition are not significantly different from each other at the 95% confidence interval. However, the distributions of maximum intensity, total precipitation, and the mean intensity are statistically different at the 95 % confidence interval. In addition, this statistical comparison also shows that the moist soil condition tends to cause higher maximum intensity, total precipitation, and mean intensity than the dry soil condition in this region.

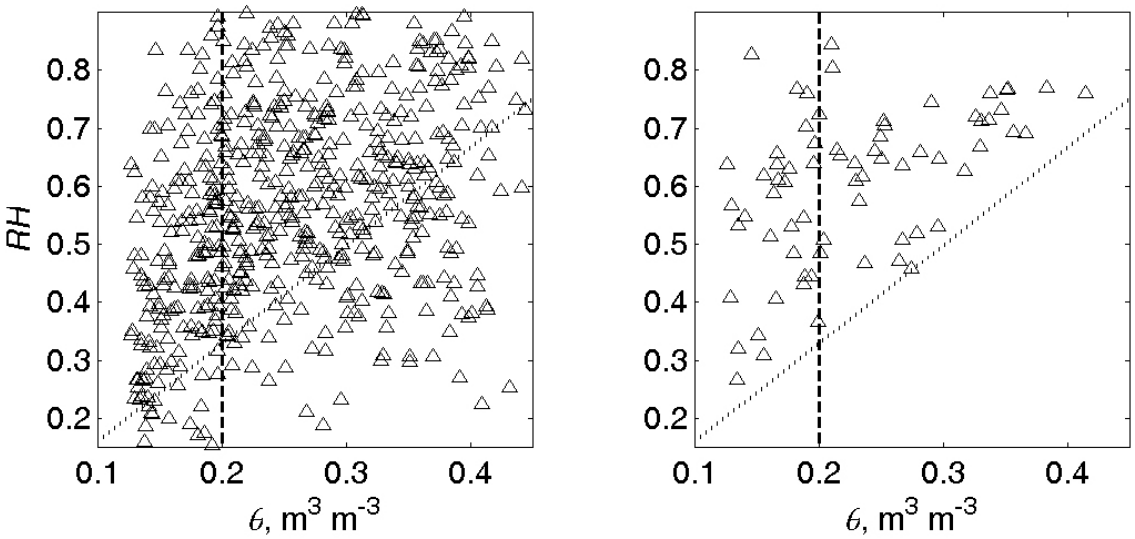

Figure 26: The mean measured *RH* and θ between 1100 LT and 1500 LT from all data points (left panel), and the measured *RH* and θ just before convective precipitation events (right panel). The $\theta = 0.2$ (vertical dashed line) is the mode of the 'dry-state' in Figure 20, and the dotted line is the boundary below which no precipitation event was observed in the record.

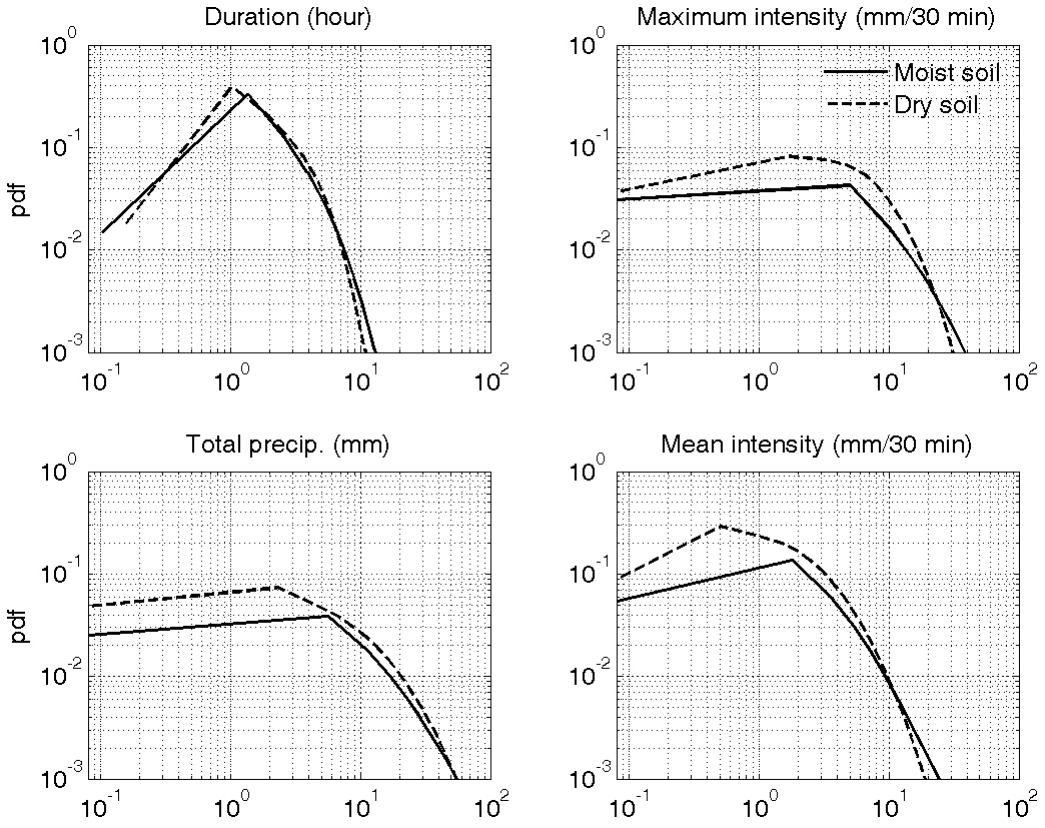

Figure 27: The comparison of precipitation statistics for the two soil water states (moist soil and dry soil conditions) shown in Figure 26.

4.5. Summary and Conclusions

Using a combination of long-term measurements, a simplified mixed-layer slab model, and conditional analysis, we demonstrated the following:

1) The proposed slab model can distinguish between convective and non-convective precipitation events and is shown to predict the timing of convective precipitation events reasonably well (~ 92.9 % within 1.5 hours).

2) The comparison between the probability density function of the identified convective and non-convective precipitation events suggests that convective events are significantly more intense (statistically different at the 99 % confidence interval).

3) From the RH-θ quadrant analysis, it was shown that the summertime convective precipitation events could be triggered by wet atmosphere and wet soil and by dry atmosphere and dry soil conditions. This suggests that a negative feedback between soil moisture states and convective precipitation may exist in this region.

4) The statistical comparisons of the precipitation characteristics for these two different soil moisture conditions shows that the moist soil conditions tend to induce higher maximum intensity and total precipitation than dry soil conditions. However, no statistical difference was detected in the duration.

The proposed approach here takes advantage of the measured sensible heat flux time series to estimate the growth of z_i and the intersection with H_{LCL} to 'mark'

convective precipitation events in point rainfall time series measurements. With the proliferation of FluxNet, a worldwide terrestrial network designed to measure energy and CO_2 fluxes along with climatic and environmental drivers [*Baldocchi et al.*, 2001], it is now possible to extend this methodology to investigate the hydrologic and physiological controls on the pathways to summertime convective precipitation across different climates and biomes. Many sites within FluxNet can now boast in excess of 5 years of measurements, including eddy-covariance sensible heat flux, mean air temperature, mean air relative humidity, root-zone soil moisture, and point rainfall at half-hourly time scales. The analysis here may also provide some clues about the interplay between triggers of convective rainfall and actual occurrences of convective rainfall events thereby offering at minimum a probabilistic framework for connecting the land-surface trigger to rainfall. For example, using the data set here, we found that during the 2001 to 2004 period, of the 612 growing season days (day 121 to day 273) 162 were 'marked' for a convective rainfall trigger and 70 days did register a convective rainfall event. Hence, the probability of 'realizing' a convective rainfall event knowing that a rainfall trigger did occur is about 45%. What is the relationship between this probability and aerosol loading; how stationary is this probability in light of rapid land-use or climatic changes are questions for future investigations that can be addressed with the availability of long-term data sets originating from FluxNet and land-cover data sets.

5. Eco-hydrological controls on summertime convective rainfall triggers

5.1 Background and Introduction

Quantitative analysis of rainfall-runoff relationships may be traced back to 1674, when Pierre Perrault published his seminal monograph *De l'origine des fontaines* (*On the Origin of Springs*) on the role of precipitation in sustaining stream flow in the Seine River. About four decades ago, some in the hydrology and climate communities argued that at sufficiently large scales watersheds can modify their own precipitation regimes, thereby marking a fundamental shift in the analysis of the hydrologic cycle [*Eagleson*, 1986]. Nevertheless, hydrological modeling has disproportionately focused on distributions and pathways of water within watersheds under the assumption that precipitation is an independent forcing term.

Recent studies have suggested that land cover change can significantly affect the Earth's climate from regional to global scales [*Chase et al.*, 2001; *Kanae et al.*, 2002; *Liston et al.*, 2002], with impacts potentially as large as from other anthropogenic factors (e.g. greenhouse gases and aerosols). For example, Baidya Roy et al [2003] utilized a numerical model to show that land cover change in the United States over the past 300 years significantly altered the climate in July. Focusing on the period from 1910 to 1990, they found that the increase in forested areas in the East Coast region of the U.S. resulted in lower surface temperature due to higher evapotranspiration (ET). Higher ET provided an important source of moisture thereby slightly enhancing precipitation in the region

[*Baidya Roy et al.*, 2003]. Recent studies further demonstrated that precipitation recycling via transpiration - and the control that soil moisture exerts on the partitioning of sensible and latent heat fluxes - can contribute to the feedback between the soil moisture state and convective precipitation [*D'Odorico and Porporato*, 2004; *Findell and Eltahir*, 2003a; b; *Freedman et al.*, 2001; *Wu and Dickinson*, 2005].

Present day changes in timberland composition, primarily from mature broadleaf-deciduous forest to pine plantations [*Wear and Greis*, 2002], are occurring at spatial scales that may be large enough to influence summertime precipitation regimes, particularly convective precipitation, in the Southeastern United States. Currently, about 60% of the forested area in this region is covered with hardwood forests. It is projected that by 2040, the total forested area will not be significantly altered but its composition will be 50% pine (primarily plantation) and 50% hardwood [*Wear and Greis*, 2002]. Because convective precipitation is the product of numerous interactions and non-linear feedbacks amongst many processes [*Eltahir and Pal*, 1996; *Findell and Eltahir*, 1999; 2003b], and is further affected by the spatial structure of vegetation and terrain, it has been difficult to assess the effect of such land-cover change on triggers of regional convective rainfall.

To simultaneously address all of the processes that trigger convective rainfall is well beyond the scope of a single study. Instead, we focus on the most elementary dynamical processes that control these triggers; namely land surface fluxes of heat and moisture, which in turn vary with the soil moisture content within the rooting-zone. The soil moisture strongly depends on soil-plant hydraulic properties and antecedent soil

moisture content [*Bohrer et al.*, 2005; *Katul et al.*, 2003; *Sperry*, 2000]. To progress even within this restricted framework, many of the governing processes must be simplified and parameterized.

The overall objective of this work is to assess how shifts in land-cover type modify convective rainfall triggers. To address this objective, we derive a simplified semi-analytical 'zero-dimensional' model that can explicitly propagate the nonlinear effects of vegetation sensitivity to soil moisture to conditions that predispose convective rainfall, while maintaining the key nonlinearities describing these interactions.

The study is organized as follows: we develop a semi-analytical solution for the growth of the convective boundary layer as a function of incident shortwave radiation and its partitioning to sensible heat flux, which depends on vegetation type and soil moisture state. Next, we explore the maximum soil moisture state that guarantees sufficient sensible heat flux for the mixed-layer depth to intersect the lifting condensation level, a condition necessary - although not sufficient - for convective rainfall events. We then assess the degree to which this predisposition to convective rainfall events differs among three vegetation types, and how it changes for each type in relation to soil moisture, by applying the model to long term (from 2001 to 2004) eddy covariance and meteorological data sets from an experimental study site with three adjacent ecosystems that experience the same climatic and edaphic conditions. The study site contains an abandoned old-field covered with grass and herbaceous species (OF), a 22-year-old (in 2005) maturing loblolly pine plantation (PP), and an 80- to 100-year-old mature oak-hickory hardwood forest (HW). We limit our analysis to periods spanning from late

spring to early fall (May to September, Julian day 121 to day 273), hereafter referred to as “summertime”. This is roughly the period in which leaf area index (LAI) is at or near its maximum [*McCarthy et al.*, submitted to Global Change Biology]. Removing periods of transient LAI from the analysis allow us to isolate the effects of soil moisture on ecophysiological controls of convective rainfall events during the period when convective rainfall most often occurs. After determining the parameters of the model, we indirectly validate the semi-analytical solution using point rainfall measurements. We then briefly discuss the relevance of this work to regional precipitation patterns in the context of projected land-cover changes.

5.2Methods and Materials

5.2.1 Experimental Site

The three adjacent vegetation types PP, HW, and OF are located within the Blackwood Division of the Duke Forest near Durham in North Carolina (35°58'N, 79°05'W, 163 m above sea level) and are part of FLUXNET, an on-going global long-term CO_2 flux monitoring initiative [*Baldocchi et al.*, 2001]. The soil type is acidic Hapludalf with a clayey loam (Enon silt loam) in the upper 0.3 m, and clay all the way down to bedrock (at ~ 0.7 m). The average saturated soil moisture content within the rooting-zone is 0.54 m^3 m^{-3} [*Oren et al.*, 1998]. The dominant rooting system depth at all three stands is about 0.3 m (Soil Survey of Orange County, North Carolina 1975).

At each ecosystem, a walkup tower is available to sample long-term environmental and near-surface eddy-covariance flux data. Detailed information about each site and experimental setup are described elsewhere (for OF site, see Novick et al. [2004]; for HW and PP sites, see Oren et al. [1998], Stoy et al. [2005], and Pataki & Oren [2003]). The precipitation, air temperature, relative humidity, radiation components (shortwave, longwave, and net radiation), and rooting-zone soil moisture content are sampled every second and averaged every 30 minutes. The turbulent sensible and latent heat fluxes are measured using eddy covariance systems with 10 Hz sampling frequency and 30 minutes averaging interval as described elsewhere [*Katul et al.*, 1997; *Stoy et al.*, 2005].

As for the hydrological properties, this region experienced a mild drought event in 2001 and a severe drought event in 2002 during the growing season. The 2001 to 2004 growing season precipitation nearly covered the wettest and driest states within the past 57-year on record, thereby providing a wide range of soil moisture and air relative humidity conditions. The probability density function (pdf) of θ for each ecosystem is shown in Figure 28 for the summer-time period. Higher θ values were more frequently observed at the HW site when compared to the other two ecosystems (Figure 28). Furthermore, at the PP site, the measured mode (θ = 0.19 m^3 m^{-3}) was below the critical soil moisture (θ = 0.20 m^3 m^{-3}) content known to induce reductions in transpiration with decreasing θ.

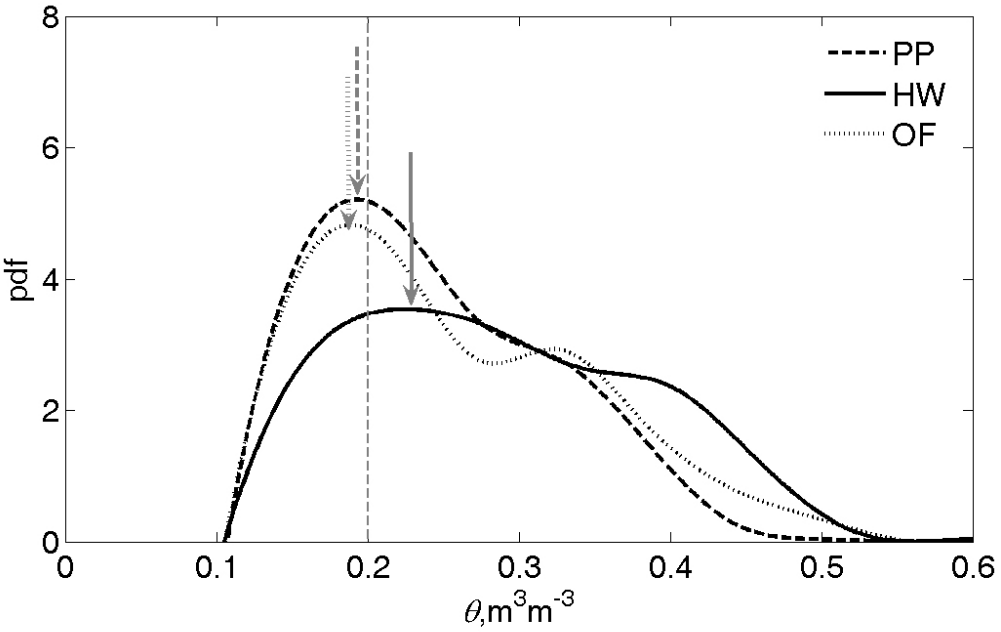

Figure 28: The probability density function (pdf) of θ for each ecosystem from 2001 to 2004 during the growing season. The gray arrows indicate the mode of the pdf for each ecosystem

5.2.2Methods

Assuming the entire mixed-layer depth is a single slab, the temporal dynamics of the mixed-layer height (z_i) can be derived using the standard budget equation for the mean slab potential temperature ($\overline{T_p}$) and the encroachment model closure [*Garc et al.*, 2002; *Stull*, 1976; 1988], given by

$$\frac{dz_i}{dt} = \frac{\overline{w'T_p'}_s - \overline{w'T_p'}_{z_i}}{\gamma z_i}, \tag{5-1}$$

where $\overline{w'T_p'}_s$ and $\overline{w'T_p'}_{z_i}$ represent the turbulent sensible heat fluxes above the land surface and at the top of the mixed-layer, respectively; γ is the lapse rate of potential temperature just above z_i, and t is time. Over-bars represent the time averaging operator, and primed quantities denote turbulent excursions around their time-averaged states. The value of γ is often approximated from sounding measurement profiles [*Eltahir and Pal*, 1996; *Findell and Eltahir*, 1999; 2003b]. Here we determined γ using all the summertime morning (0700 LT) sounding data from 2001 to 2004 at Piedmont Triad International Airport (GSO, 36°05'N, 79°57'W, 270 m above sea level and 79 km west of the Duke Forest site). The resulting ensemble-averaged $\gamma = 11.6\times10^{-3}$ °C m^{-1} is about 18 % larger than the dry adiabatic lapse rate; this is consistent with other research findings [*Haiden*, 1997].

For analytical tractability, the sensible heat flux at the top of the mixed-layer ($\overline{w'T_p'}_{z_i}$) is parameterized using standard encroachment closure schemes [*Garratt*, 1992]

$$\overline{w'T_p'}_{z_i} = -\beta(t)\,\overline{w'T_p'}_{s}, \tag{5-2}$$

where β is a similarity coefficient. Although the value of β changes with time of day, several numerical studies and measurements suggest that β is between 0.2 and 0.4 [*Betts et al.*, 1992; *Kim and Entekhabi*, 1998]. Here, we assumed a constant value of $\beta = 0.3$ based on findings from Kim & Entekhabi [1998].

To avoid the use of detailed physiological parameters to model transpiration and evaporation and then model sensible heat flux via energy balance partitioning, we account for the effect of θ using a dimensionless quantity $\alpha(\theta)$ given by the ratio H_s / R_i, where H_s is the surface sensible heat flux (W m^{-2}), given by $H_s = \rho C_p \overline{w'T_p'}_s$, where ρ is the mean air density, C_p is the specific heat of dry air at constant pressure, and R_i is the incident shortwave radiation (W m^{-2}) at the surface. Thus, the parameter α describes how much of the incident shortwave radiation is converted into sensible heat flux by the ecosystem. Naturally, a moist rooting-zone allow high rates of latent heat flux under high radiation loads, reducing the sensible heat flux, and resulting in a smaller $\alpha(\theta)$ when compared to a drier rooting-zone. Furthermore, $\alpha(\theta)$ is not likely to exceed 0.5 even for the driest soil moisture state because net radiation rarely exceeds 70 % of incident shortwave radiation and the half-hourly values of soil heat flux (or heat storage

within the canopy volume) are always finite during daytime conditions. This formulation effectively lumps all the physiological, aerodynamic, soil and plant radiative properties, and soil and plant hydraulic properties into one $\alpha(\theta)$ relationship so that the dynamics of the mixed-layer height is approximated as

$$\frac{dz_i}{dt} = \frac{\alpha(\theta)(1+\beta)R_i(t)}{\gamma z_i \rho C_p}. \tag{5-3}$$

For analytical tractability, we simply assume that diurnal variations of R_i may be approximated (for cloud-free conditions) by

$$R_i(t) = R_{\max} \sin\left[\omega(t-t_0)\right], \tag{5-4}$$

where $R_{\max}$ is the maximum incident shortwave radiation at a given day of year (and varies with site latitude and elevation), t is in hours, and $\omega = \pi/\tau$, where τ (hour) is the time span from sunrise ($t = t_0$) to sunset and also varies with the day of year.

Replacing all these simplifications into Equation (5-1) and integrating the outcome from sunrise ($t = t_o$) to the time when a convective precipitation event (if any) occurs ($t = t_R$), yields

$$z_i(t_R) = \sqrt{z_i^{\,2}(t_o) + 2\frac{\alpha(\theta)\times(1+\beta)}{\gamma\,\omega\,\rho\,C_p}\left(1-\cos[\omega(t_R-t_o)]\right)R_{\max}}, \tag{5-5}$$

where $z_i(t_o)$ is the antecedent depth of the stable boundary layer just before sunrise and can be estimated from dimensional analysis [*Zilitinkevich*, 1972]. Note that Equation (5-5) suggests that the growth of $z_i(t)$ can be analytically determined from the

soil moisture content through the value of $\alpha(\theta)$, which is primarily (but not exclusively) controlled by the sensitivity of the latent heat flux to soil moisture stress.

Also for analytical tractability, we assume that the intersection of z_i with the lifting condensation level (H_{LCL}) is a necessary condition for convective rainfall triggering. The quantity H_{LCL} varies with the surface mixing ratio ($r(t)$), mean air temperature ($T_a(t)$), and surface pressure (P_s) using

$$H_{LCL} = \frac{R T_a}{M_a g} \log\left(\frac{P_s}{P_{LCL}}\right), \tag{5-6}$$

where R is the universal gas constant (= 8.314 J mol^{-1} K^{-1}), M_a is the molecular weight of the air (~ 29 g mol^{-1}), P_s (kPa) is the local atmospheric pressure at the surface, and P_{LCL} (kPa) is the atmospheric pressure at H_{LCL}. The value of P_{LCL} can be approximately determined from a hydrostatic assumption using

$$P_{LCL} = P_s\left(\frac{T_{LCL}}{T_a}\right)^{3.5}, \tag{5-7}$$

where T_{LCL} (K) is the saturation point temperature at H_{LCL} and can be derived from the Clausius-Clapeyron equation given by [*Stull*, 1988]

$$T_{LCL} = \frac{2840}{3.5\ln(T_a) - \ln\left(\frac{P_s \cdot r}{0.622 + r} - 7.108\right)} + 55, \tag{5-8}$$

where r can be calculated from the near-surface relative humidity RH, and the parameter 3.5 is given from the inverse of the Poisson constant.

It directly follows from Equation (5-5) that for a specified atmospheric humidity and air temperature states, convective rainfall is primarily 'triggered' when the rooting-zone soil moisture leads to an α exceeding

$$\alpha(\theta) \geq \frac{\gamma \omega \rho C_p \left\{ \left[H_{LCL}(r, T_a, P_s) \right]^2 - \left[z_i(t_o) \right]^2 \right\}}{2(1+\beta)\left\{ 1 - \cos[\omega(t_R - t_o)] \right\} R_{\max}} \ . \tag{5-9}$$

Equation (5-9) defines the minimum α that is needed to ensure that sufficient sensible heat flux is available to increase z_i up to H_{LCL}. Naturally, this condition predisposes, but does not necessarily lead to, convective rainfall. When air parcels reach H_{LCL}, condensation forms in regions of negatively buoyant 'overshoots of mixed-layer thermals' [*Stull*, 1988]. These thermals penetrate the capping inversion at the top of z_i. If the overshoot is sufficiently strong to continue lifting the condensing air parcel, latent heat is released and its potential temperature becomes sufficiently warmer than the surrounding environment and it becomes positively buoyant. The height at which a cloudy air parcel becomes positively buoyant defines the 'level of free convection', LFC. This parcel continues to buoyantly rise until it eventually becomes cooler than its surrounding environment at which point the 'limit of convective' rise, LOC, is attained. Any residual inertia in the rising parcel might propel it to continue rising further eventually stopping at the cloud top [*Emanuel et al.*, 1994; *Stull*, 1988]. Several measures

of potential energies are available to quantify the cloud thickness, often defined between LFC and LOC, such as convective available potential energy (CAPE) and evaporative available potential energy (EAPE). Once clouds develop, condensation nuclei allow rapid growth of water droplet. When these water droplets reach sufficient size to precipitate and re-penetrate the unsaturated air below the cloud base without completely evaporating before reaching the ground surface, rainfall at the surface occurs. Roughly, after z_i intersects H_{LCL}, this entire process leading to precipitation detection at the ground may vary from minutes up to 2 hours [*Stull*, 1988]. Thus, Equation (5-9) must be viewed as a necessary - but not sufficient condition for convective rainfall events.

The presence of vegetation may impact the estimation of the lifting condensation level $H_{LCL}(t)$ because the measured air temperature $T_a(t)$ and mixing ratio $r(t)$ within or near the canopy sub-layer are known to differ among vegetation types. To assess the potential impact of vegetation types on H_{LCL} at the study site, and thus on our study, we compared H_{LCL} using the near surface measured $T_a(t)$ and $r(t)$ collected at OF, HW, and PP and found that H_{LCL} is robust to the underlying land-cover surface at this site (Figure 29). This finding is not entirely surprising because the temporal dynamics of $T_a(t)$ and $r(t)$ are often much larger than their spatial variability across these three ecosystems. Hence, in a first-order analysis, it is reasonable to assume that $H_{LCL}(t)$ is approximately the same at all three ecosystems.

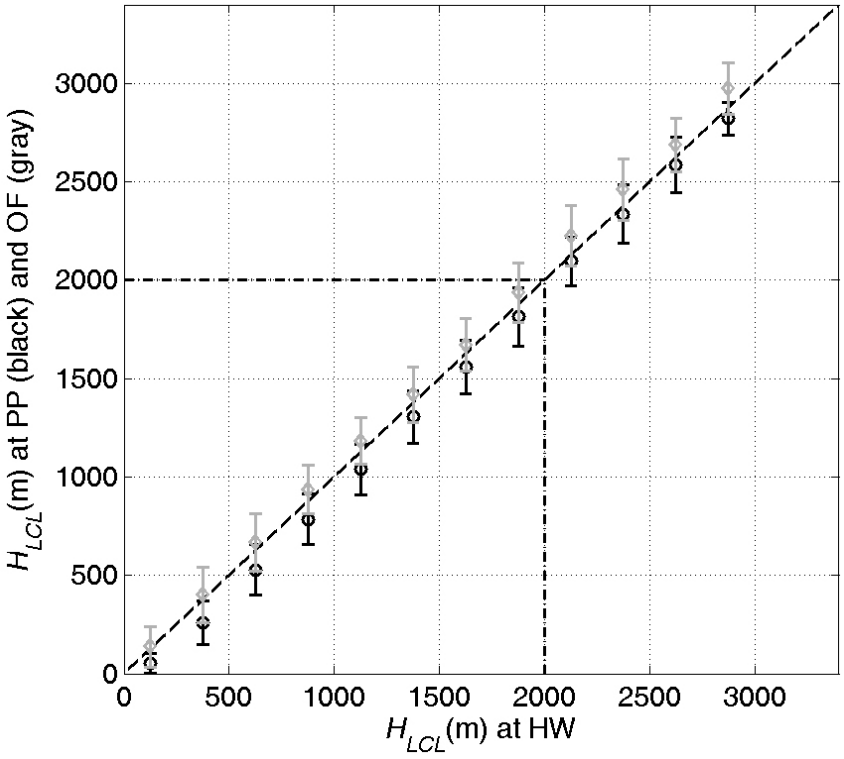

Figure 29: The lifting condensation level (H_{LCL}) derived using $r(t)$ and $T(t)$ measured at PP (error bars in black) and OF (error bars in gray) when compared to those measured from the HW ecosystem (the dominant land cover type in a 10 km by 10 km region around the site). The dash-dot lines at 2000 m represent the maximum mixed-layer depth in this region. The dots represent the ensemble average of all half-hourly runs and the vertical bar is 1 standard deviation around the ensemble average.

5.3 Results and Discussion

We now focus on the impact of vegetation on triggers of convective rainfall and present indirect but independent validation of the proposed semi-analytical model using point rainfall measurements.

5.3.1 Soil moisture and vegetation control on partitioning of surface fluxes

Figure 30 shows how θ, measured at each of the three ecosystems, affect the value of α. Here we discuss the convective rainfall disposition mechanism for two different soil moisture regimes.

(1) Regime 1, $\partial\alpha/\partial\theta \approx 0$:

This regime exists for relatively moist soil conditions at all three sites; however, the onset of this regime differs among the three sites. For the forested ecosystems here, the onset of this regime appears to be $\theta > 0.20$ m^3 m^{-3}. This onset is consistent with the threshold soil moisture known to regulate stomatal conductance [*Oren et al.*, 1998; *Oren and Pataki*, 2001]. For the OF site, the onset of this regime occurs at a much higher soil moisture state ($\theta > 0.30$ m^3 m^{-3}) suggesting that soil moisture controls on α are active over a much broader range of conditions during the growing season (see Figure 28 for the mode of θ).

(2) Regime 2, $\partial\alpha/\partial\theta < 0$:

In this regime, α increases with decreasing θ. As earlier stated, this increase reflects a number of processes, including soil moisture controls on transpiration, soil evaporation, and soil heat flux. The three ecosystems differ in both magnitude of $|\partial\alpha/\partial\theta|$ and its non-zero onset. In light of the pdfs in Figure 28, we emphasize that this regime occurs by far more frequently during summertime when compared to regime 1 at all three sites. For the forested ecosystems, we find that $|\partial\alpha/\partial\theta|$ for HW is much smaller than PP, suggesting that the convective rainfall dispositions at HW are the least sensitive to variations in soil moisture when compared to OF and PP. For PP, $|\partial\alpha/\partial\theta|$ rapidly increases when $\theta < 0.18$, even exceeding its OF counterpart for these dry states. When θ decreases to the driest condition observed in the data record (i.e. $\theta = 0.13$ m^3 m^{-3}, Figure 28), the value of α increases to ~ 0.33 at PP, ~ 0.29 at OF, and ~ 0.21 at HW. Hence, the highest α was, surprisingly, not at OF but at PP.

Interestingly, the comparison of α among different vegetation types for regime 1 suggests that α $(= 0.21)$ at PP remains significantly larger than the other two vegetation types ($\alpha = 0.15$ for HW and $\alpha = 0.16$ for OF). Given that these three vegetation types experience the same incident shortwave radiation and precipitation, we explored potential explanations for this pattern in observed minimum α using the corresponding frequency distributions of the energy budget components (net radiation R_n, sensible heat flux H_s, and latent heat flux LE), and the residuals (the difference between R_n and

$H_s + LE$). We restrict this analysis to near convective conditions over the entire four-year summertime record because they are more pertinent to triggers of convective rainfall (Figure 31). Here free convective conditions prevail when the atmospheric stability parameter (z/L) satisfies the condition $-z/L \geq 5$ [*Juang et al.*, in press], where $z = z_i/2$, and L is the Obukhov length, which is derived from the near surface friction velocity (u_*), $\overline{w'T_p'}_s$ and T_a.

While incident shortwave radiation is identical in all three ecosystems, R_n is not necessarily identical given differences among the vegetation types in albedo, surface emissivity, and skin temperature. This difference is most evident in Figure 31, which presents the modes of measured R_n distributions across the entire summertime period for the four-year record. OF has higher albedo and skin temperature and yields the smallest R_n mode, followed in turn by PP, and HW. Interestingly, for moist soil conditions, the modes in *LE* are comparable suggesting that evaporation, in addition to transpiration, should be significant at OF given the large differences in leaf area index (LAI). The frequency distribution of the combined storage and soil heat fluxes (i.e. the residuals of $R_n - (H_s + LE)$) show the largest residual for HW followed in turn by OF and PP. At HW, the storage flux can be significantly large due to the large canopy volume (maximum canopy height = 35 m); at the OF site, the soil heat flux is significant in the energy partitioning (at least when compared to PP). These two factors may account for higher H_s at PP when compared to HW and OF under moist soil conditions (see Figure

31). When the soil is dry, the modes of the LE fluxes diverge, but the modes of the combined storage and soil heat flux distributions retain their relative importance. This analysis clearly demonstrates that the role of soil heat flux, canopy heat storage, and soil evaporation must be considered when the mixed-layer height is modeled based on the energy budget.

Next, we illustrate the potential impact of the observed differences in $\alpha(\theta)$ among the three vegetation types on forecasting triggers for convective rainfall events. Before doing so, however, we test whether the sinusoidal approximation for the incidental shortwave radiation (Equation (5-4)) is reasonable here. Figure 32 suggests that this approximation is sufficiently accurate for clear sky conditions up to the formation of clouds. We also compared the ratio of maximum z_i derived at PP and OF to the maximum z_i computed at HW (the dominant species in the 10 km $\times$ 10 km area around the site) as a function of θ. Based on the model calculations, PP enhances convective rainfall triggers over HW by ~ 17% when soils are moist and ~ 25% during conditions in which the soil reaches its driest state (Figure 33). In contrast, when $\theta > 0.30$ m^3 m^{-3}, OF and HW generate a similar enhancement of convective rainfall triggers; however as the soil dries, the enhancement of convective rainfall triggers by OF increases relative to that by HW, reaching an 18 % greater trigger potential at $\theta = 0.13$ m^3 m^{-3}.

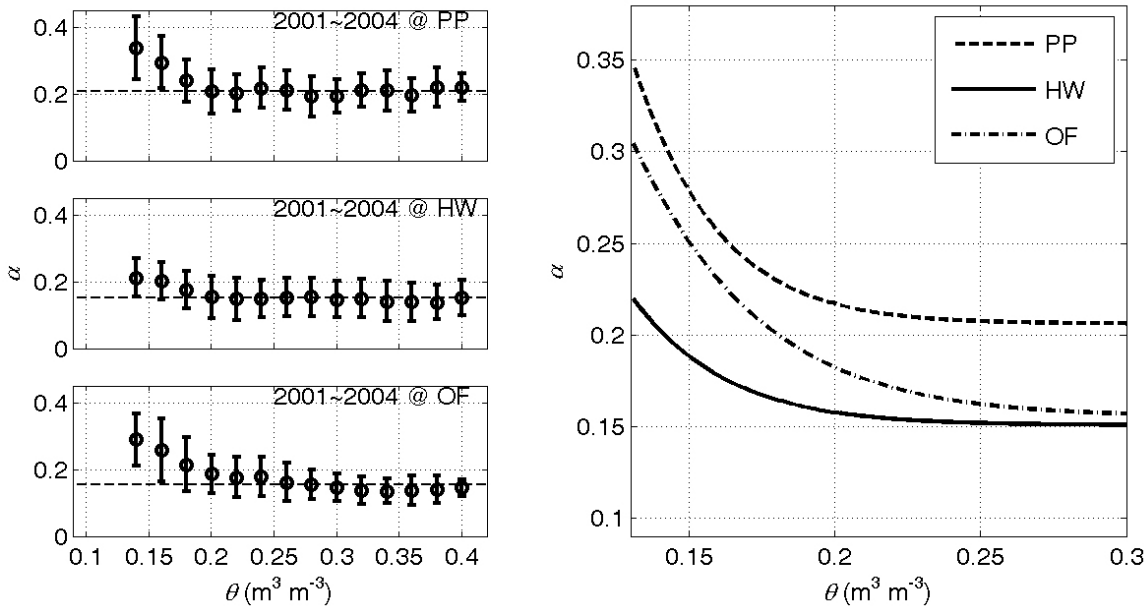

Figure 30: Relationship between measured local θ and measured ensemble averaged α (H_s normalized by R_i) for each ecosystem (left panel). The regression curves to these data are also shown for comparisons (right panel)

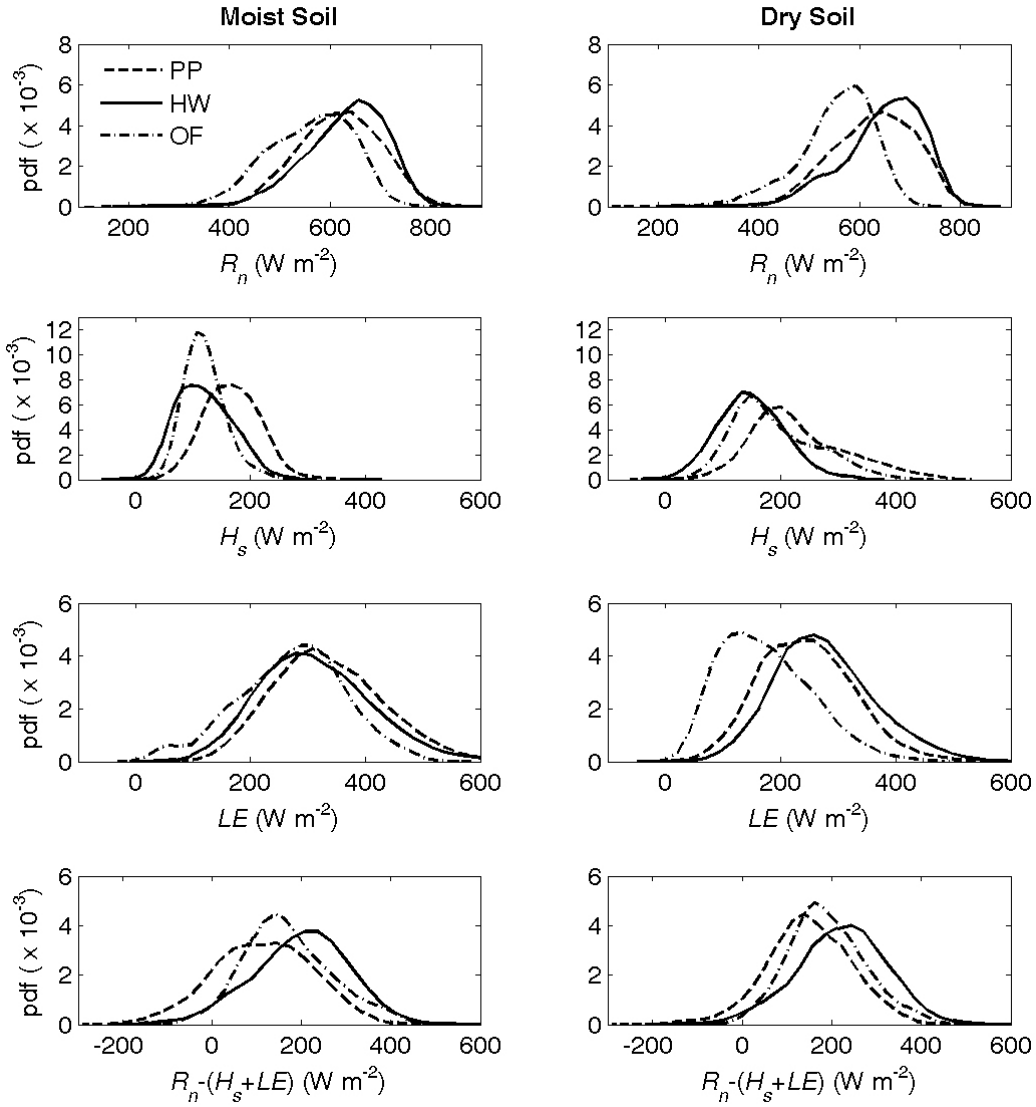

Figure 31: The frequency distribution of measured net radiation (R_n), sensible heat flux (H_s), latent heat flux (LE), and the residuals at PP, HW, and OF for both moist ($\theta \geq 0.2$ m^3 m^{-3}) and dry soil ($\theta < 0.2$ m^3 m^{-3}) conditions. The data represent midday (1100 LT-1400 LT) condition from day 121 to day 273 in 2001 to 2004.

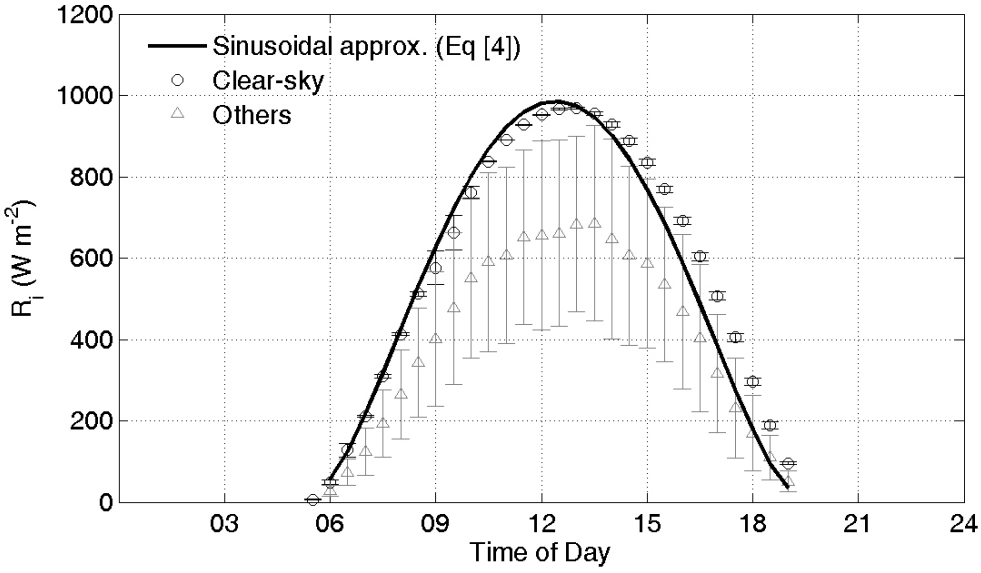

Figure 32: The temporal variation of incident shortwave radiation (R_i) from the measurements and the sinusoidal approximation (Equation (5-4)). The condition "others" refers to days that are not cloud-free.

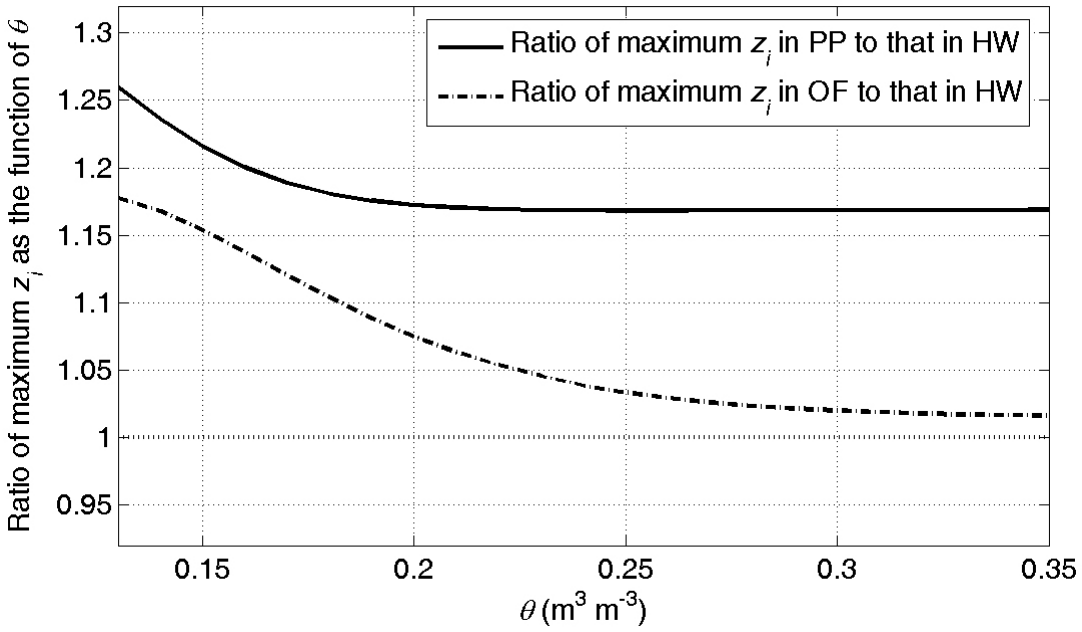

Figure 33: The modeled ratio of maximum z_i at PP (dashed line) and maximum z_i at OF (solid line) to the maximum z_i at HW as a function of local soil moisture content (θ).

5.3.2 Testing the Model using Point Rainfall Measurements

Although it is not possible to directly test the model, some indirect tests can be conducted to assess whether the semi-analytical model captures the 'canonical attributes' of convective rainfall triggers. However, before presenting these tests, it is necessary to discuss the spatial 'scale' of convective rainfall triggers in the context of this experiment.

Convective rainfall cells extend a few kilometers horizontally, and the land-surface 'footprint' impacting this trigger is at least 10 km × 10 km. Using a supervised land cover classification scheme on a multi-spectral image (IKONOS satellite, Space Imaging, Thornton, CO, USA) collected on September 19 of 2004, we determined that PP-, HW-, OF-type ecosystems and 'other' land covers (mainly residential area and roads) cover 33.3%, 41.6%, 16.8% and 8.3% of the 10 km × 10 km area surrounding the study site, respectively [*Juang et al.*, in press]. We re-assigned the 'other' land cover types to OF. Using the measured sensible heat flux at OF, PP, and HW and applying an area-weighted average, we determined the overall sensible heat flux responsible for mixed-layer growth at this spatial scale [*Juang et al.*, in press]. Similarly, we computed the area-averaged soil moisture content, area-averaged α, and H_{LCL} (although we showed earlier the latter does not vary spatially). Using the time series of the area-averaged sensible heat flux, we numerically solved for z_i using Equation (5-1) and compared these numerical results with the semi-analytical model in Equation (5-5) for all the growing season days

within the four-year record. The semi-analytical model was forced with the area-averaged θ and assumes a sinusoidal R_s. This comparison, shown in Figure 34, suggests that z_i estimated from the semi-analytical expression over-estimates the numerically derived z_i by about 350 m. This overestimation is expected because Equation (5-5) assumes clear sky conditions while the numerical model in Equation (5-1) was forced by the measured H_s thereby accounting for cloud effects on surface heating. When only clear sky days are used in this comparison, the agreement between the semi-analytical and the numerical models is remarkably good (± 8%). The relationship shown in Figure 34 suggests that Equation (5-5) can reasonably describe the dynamics in z_i for clear-sky conditions. Note that in Equation (5-5), when all the environmental factors ($R_{\max}$, ρ, γ, and $z_i(t_0)$) are specified, the value of $z_i(t_R)$ is strictly a function of α and t. Hence, the errors incurred in determining the spatially averaged θ propagate to $z_i(t_R)$ in Equation (5-5).

We also compare how well the semi-analytical and numerical models predict t_R, namely the timing of convective rainfall detected by the tipping bucket gauge (e.g., Figure 35). We find that both models reproduced t_R reasonably well. In the computations of t_R, H_{LCL} was forced by the area-averaged $r(t)$ and $T_a(t)$. This agreement in t_R supports the argument that under clear sky conditions both–analytical and numerical models can predict well the convective rainfall triggers. However, the semi-analytical expression produces an error distribution in the timing that has a heavier tail in the negative region (Figure 35). By assuming cloud-free conditions in the semi-analytical

expression, greater mixed-layer height is induced with earlier intersection between z_i and H_{LCL}. The mode of the 'timing error' histogram is -0.60 hours for the semi-analytical model and -0.18 hours for the numerical model. Noting that the tipping bucket gauge is a point rainfall measure summed every 0.5 hours, and noting that convective rainfall does not occur instantly when the lifting condensation level intersects the boundary layer depth, a –0.6 hour timing error should not be a primary cause for concern.

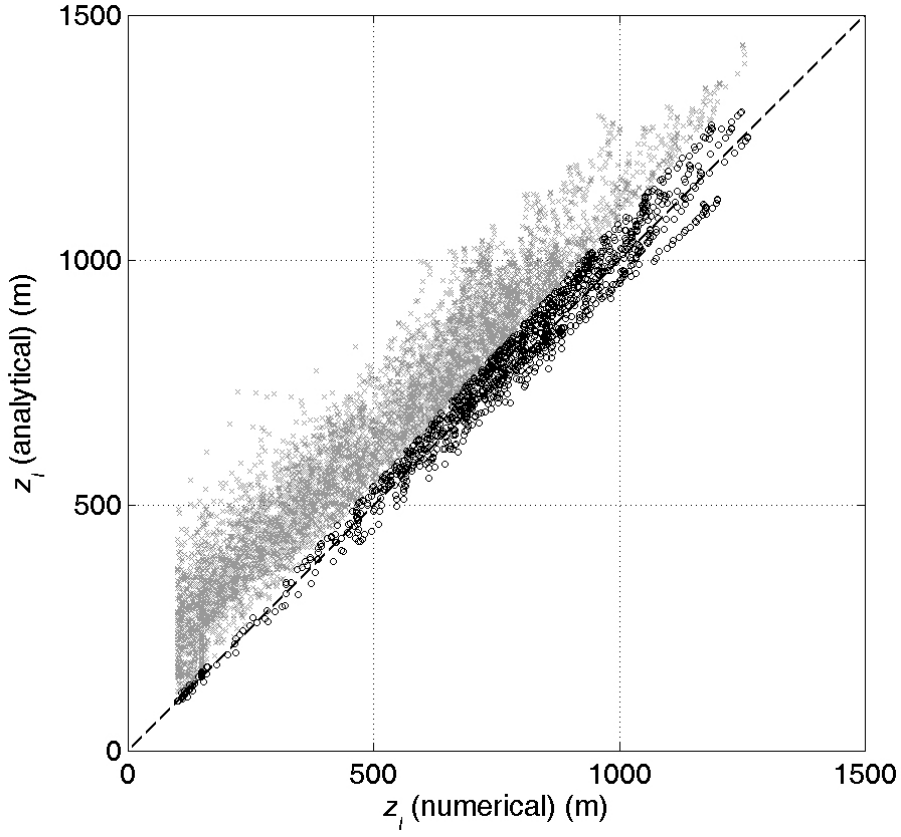

Figure 34: A comparison of z_i derived with the analytical expression and the numerical method. The gray points include all runs while the dark open circles are for clear-sky conditions. The 1:1 line is also shown for reference.

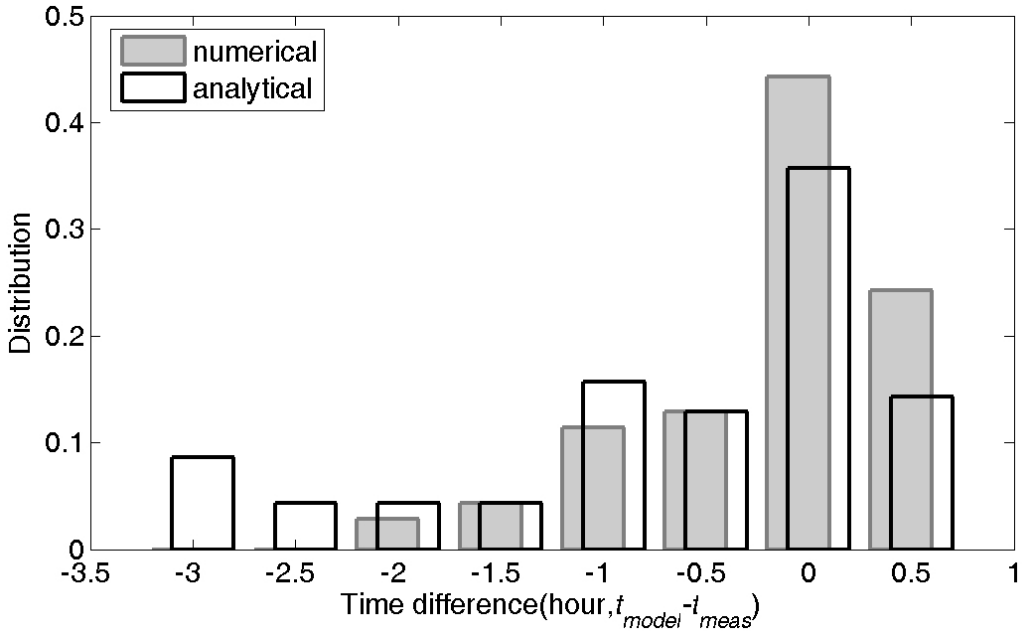

Figure 35: The frequency distribution of the timing error between tipping bucket precipitation measured with rain gauges and modeled (i.e., when $z_i = H_{LCL}$) using the analytical and numerical approaches

5.4 Conclusions and Broader Impacts

This study demonstrated that for clear sky conditions, a simple semi-analytical expression that links the soil moisture state within the root zone to the mixed-layer depth has remarkable skills in predicting the timing of convective precipitation when other necessary conditions cause it to occur. While the analytical model proposed here makes several assumptions about the convective boundary depth dynamics, recent advances in ceilometers may offer a platform where this depth can be routinely measured in the near future [*Emeis et al.*, 2004]. The broader impact of this work lies in its relevance to assessing how shifts in land cover types might impact summertime convective rainfall. For example, over the past half century, the timberland area in the SE experienced little fluctuation (~ ±3.1% with a minimum of 793 thousand km^2 in 1989 and a maximum of 845 thousand km^2 in 1956) [*Juang et al.*, in press; *Wear and Greis*, 2002]; however, the composition of the timberland area has been significantly changing. The proportion of planted pine forests to the total timberland area in the SE region has dramatically increased from under 1.0 % in the early 1950s to about 16.9 % in 1999. Furthermore, based on economic and land-use projections, the proportions of planted pine is expected to increase up to 30.5 % by year 2040 [*Wear and Greis*, 2002]. Such dramatic land cover change may significantly alter the pattern of summertime convective precipitation. Our analysis suggests that increasing coverage of pine plantation may lead to increased convective rainfall trigger activity during the summertime. At the regional scale, this may also mean that the pines, the most drought sensitive among the forest types, may produce

conditions predisposing the atmosphere to produce rains, thus reducing, on average, the effect of droughts.

6. Separating the effects of albedo from eco-physiological changes on surface temperature along a successional chronosequence in the Southeastern US

6.1. Background and Introduction

Radiative perturbations due to land-cover changes are considered among the strongest climate forcing mechanisms at global and regional scales (e.g. *Cess* [1978], *Charney et al* [1977], and *Otterman* [1977]). Small changes in surface albedo (α_s), even below detection limits of existing satellite-derived products, can lead to global temperature changes equivalent to any of the enhanced green house gases [*Charlson et al.,* 2005]. Regionally, modeling studies have already documented that the positive forcing induced by decreased α_s in boreal forests can be sufficiently large to offset the negative forcing expected from increased carbon sequestration by these forests [*Betts*, 2000]. Other studies also found that historical land-cover conversion in mid-latitude agricultural regions may have decreased air temperatures by 1° to 2°C primarily due to the role of α_s [*Feddema et al.*, 2005].

In the Southeastern U.S. (SE), conversion of abandoned agricultural land to forested ecosystems is progressing at an unprecedented rate, though few attempts have been made to quantify its potential impact on air temperature (T_a) changes. Over the next 40 years, the area of land populated by pine plantations within the SE is projected to increase from 0.13 to 0.22 million km^2, with concomitant declines in upland hardwood

forested area from 0.27 to 0.23 million km^2, and agricultural land from 0.40 to 0.26 million km^2 [*Wear and Greis*, 2002]. Given the large incident shortwave radiation in this region, minor albedo changes ($\delta\alpha_s$) due to such ecosystem conversion can result in significant change in air temperature (δT_a). However, land-cover change is not restricted to albedo alterations but also impacts bulk canopy (g_b) conductance and surface emissivity (ε_s). The relative importance of these effects on δT_a, in relation to α_s, must be jointly explored. At regional scales, following such projected land-cover change, the maximum δT_a occurs when all changes in surface temperature (δT_s) translate to air temperature (i.e., $\delta T_s \approx$ maximum δT_a). Hence, by locally (i.e. at the field scale) exploring how land use change influence δT_s through $\delta\alpha_s$, $\delta\varepsilon_s$, and δg_b, we can constrain the upper limits in expected δT_a following such anticipated land-cover change. As a necessary first step towards progressing on this objective, δT_s is measured and modeled from $\delta\alpha_s$, $\delta\varepsilon_s$, and δg_b using data collected from three adjacent ecosystems representing the two end-members and an intermediate stage of a successional gradient in the SE as shown in Figure 36. The study ecosystems, all experiencing similar climatic and edaphic conditions, include an abandoned agricultural old-field (OF) grass site, an early successional planted pine forest (PP), and a late-successional hardwood forest (HW). Here, we report on $\delta\alpha_s$, $\delta\varepsilon_s$, and δg_b estimated from heat flux and radiation measurements across these three sites and explore the relative importance of albedo vis-à-vis the remaining factors on observed annual δT_s.

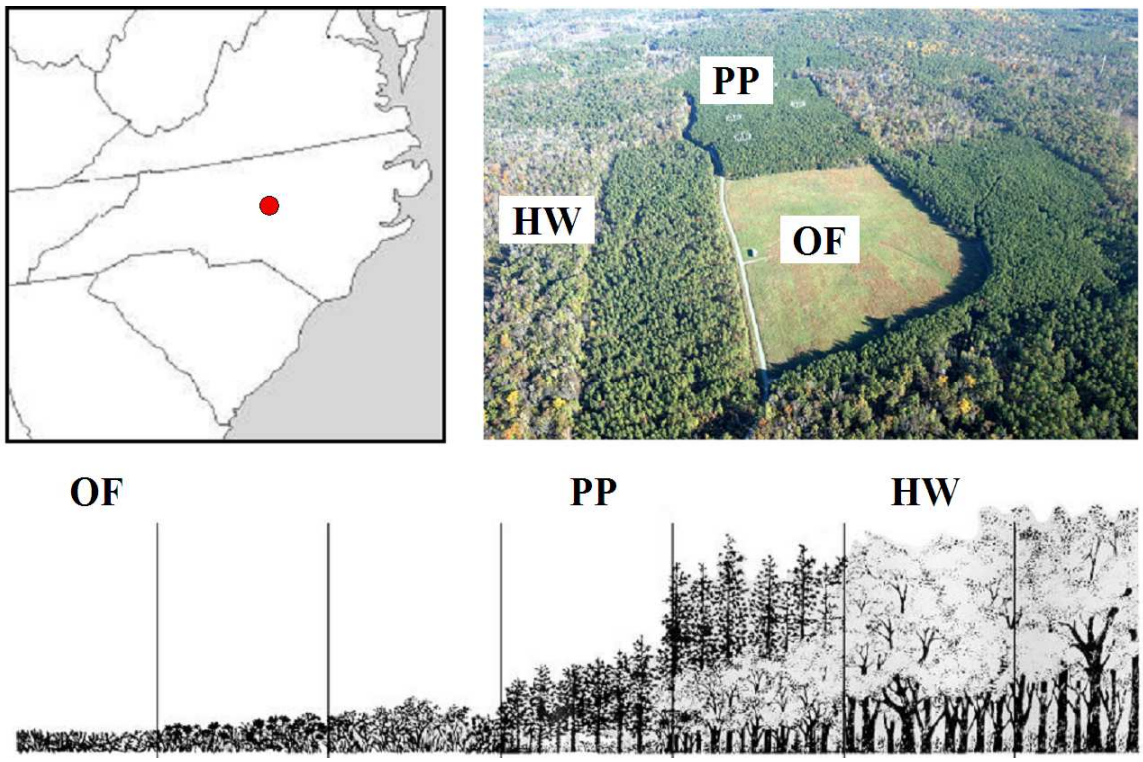

Figure 36: Upper panel: The location of the three AmeriFlux sites at the Blackwood Division of Duke Forest, near Durham, North Carolina (left); an aerial photograph of the three sites in Autumn showing the brighter land-cover of the OF relative to HW and PP (right). Lower panel: A typical succession in the SE after agricultural fields are abandoned.

6.2 Study Site

The three adjacent ecosystems - OF, PP, and HW are located within the Blackwood Division of the Duke Forest near Durham in North Carolina (35°58'N, 79°05'W, 163 m above sea level, see Figure 36) and are part of FLUXNET, an on-going global long-term micrometeorological monitoring initiative [*Baldocchi et al.*, 2001]. The long-term mean annual precipitation is 1185 ± 177 mm, and the annual mean air temperature is 14.9 ± 0.9 °C. The local topographic variations in the vicinity are small (slope $< 5\%$) enough to ignore the effects of complex terrain on the flow statistics [*Siqueira et al.*, 2002].

In each ecosystem, a meteorological tower is available to sample long-term environmental and near surface eddy-covariance (EC) fluxes. The turbulent sensible heat (H) and latent heat (LE) fluxes were measured above the canopy using an EC system comprised of a LI-7500 open-path CO_2/H_2O gas analyzer (Li-Cor Inc., Lincoln, NE, USA) and a CSAT3 tri-axial sonic anemometer (Campbell Scientific Inc., Logan, UT, USA). The net radiation (R_n), and long- and short-wave radiation (incoming and outgoing) were sampled using a Kipp & Zonen CNR1 net radiometer (Kipp & Zonen USA Inc., Bohemia, NY, USA) since 2004. Details about each site, the experimental setup (for OF site, see *Novick et al.* [2004]; for HW and PP sites, see *Oren et al.* [1998], *Stoy et al.* [2005], and *Pataki and Oren* [2003]), and the data processing are described elsewhere [*Katul et al.*, 1997; *Stoy et al.*, 2005].

6.3. Theory

The energy and radiation balance at the land-surface are given by

$$R_n = (1-\alpha_s)R_{si} - \varepsilon_s \sigma T_s^4 + R_{li} = LE + H + G_s, \quad (6\text{-}1)$$

where R_{si} and R_{li} are the incident shortwave radiation and the downward longwave radiation, respectively; σ is the Stefan-Boltzmann constant ($=5.67\times10^{-8}$ J K^{-4} m^{-2} s^{-1}), and G_s is the combined soil and storage heat fluxes. In Equation (6-1), the α_s is defined as the ratio of outgoing to incident short-wave radiation. Because these three ecosystems are within 1 km of each other, they experience almost identical R_{si} and R_{li} at least on annual time scales.

Since this region is sufficiently humid, the latent heat flux may be modeled from a Priestley-Taylor like equation [*Priestley and Taylor*, 1972]:

$$LE = \alpha \frac{\Delta}{\Delta + \gamma}(Q_n), \quad (6\text{-}2)$$

where $Q_n = R_n - G_s$, Δ is the slope of the saturation vapor pressure- temperature curve, γ is the psychrometric constant (the ratio of specific heat of moist air at constant pressure C_p to the latent heat of vaporization of water L_v), and α is the Priestley-Taylor parameter. For short vegetation (or bare soil), $\alpha = 1.26$ as was determined for well-watered conditions [*Parlange and Katul*, 1992; *Stull*, 1988]. For tall-forested ecosystems,

$\alpha < 1$ due to the added hydraulic resistance along the long pathway from the soil to the atmosphere even for well-watered soil moisture conditions. The H can be expressed as

$$H = Q_n \left(1 - \alpha \frac{\Delta}{\Delta + \gamma}\right) = \rho C_p g_a (T_s - T_a), \tag{6-3}$$

where ρ is the mean air density, and g_a is the bulk aerodynamic conductance. Let

$$\eta = \frac{\rho C_p g_a}{1 - \alpha \frac{\Delta}{\Delta + \gamma}} = \frac{Q_n}{(T_s - T_a)},$$

then T_s is given by the solution to the following algebraic equation:

$$\varepsilon_s \sigma T_s^4 + \eta T_s = (1 - \alpha_s) R_{si} + R_{li} + \eta T_a - G_s. \tag{6-4}$$

The left-hand side (LHS) of Equation (6-4) is a function of T_s, η, and ε_s, while the right-hand side (RHS) is a function of α_s, η, and G_s. Our objectives are to examine how land-cover changes, quantified by changes in α_s, η, and G_s, impact T_s. Defining these as

$$\begin{aligned} \text{LHS} &= f_1(\eta, T_s, \varepsilon_s) = \varepsilon_s \sigma T_s^4 + \eta T_s \\ \text{RHS} &= f_2(\eta, \alpha_s, G_s) = (1 - \alpha_s) R_{si} + R_{li} + \eta T_a - G_s \end{aligned},$$

and considering only the first-order terms in the total derivative expansions results in

$$df_1 = \left(\frac{\partial f_1}{\partial T_s} \delta T_s + \frac{\partial f_1}{\partial \eta} \delta \eta + \frac{\partial f_1}{\partial \varepsilon_s} \delta \varepsilon_s\right) = df_2 = \left(\frac{\partial f_2}{\partial \eta} \delta \eta + \frac{\partial f_2}{\partial \alpha_s} \delta \alpha_s + \frac{\partial f_2}{\partial G_s} \delta G_s\right).$$

Hence, land-cover change yields a concomitant surface temperature change given by

$$\delta T_s = \frac{\left(\frac{\partial f_2}{\partial \eta} - \frac{\partial f_1}{\partial \eta}\right)\delta\eta + \frac{\partial f_2}{\partial \alpha_s}\delta\alpha_s + \frac{\partial f_2}{\partial G_s}\delta G_s - \frac{\partial f_1}{\partial \varepsilon_s}\delta\varepsilon_s}{\frac{\partial f_1}{\partial T_s}}.$$

After evaluating all the partial derivatives, we obtain the following expression for surface temperature changes:

$$\delta T_s = \frac{1}{4\sigma\varepsilon_s T_s^3 + \eta}\underbrace{\left[\left(T_a - T_s\right)\delta\eta}_{\text{I}} \underbrace{- R_{Si}\delta\alpha_s}_{\text{II}} \underbrace{- \delta G_s}_{\text{III}} \underbrace{- \sigma T_s^4 \delta\varepsilon_s}_{\text{IV}}\right]. \qquad (6\text{-}5)$$

Equation (6-5) shows that four major factors affect surface temperature following land-cover changes: Term I, an eco-physiological component, term II, an albedo component, term III, a heat storage change (expected to be small), and finally, term IV a thermal emissivity component. Below, the relative importance of these four terms are explored for a land-cover conversion from (a) OF to PP and (b) OF to HW.

6.4 Results and Discussion

The upper panel in Figure 37 presents the relationship between ensemble measured α_s and the solar zenith angle (ψ, in cosine) in all three ecosystems. As evidenced by Figure 37, the α_s in OF is generally higher than PP and HW and increases gradually as ψ increases. The forested ecosystems maintained a near-constant α_s for small ψ (*i.e.* $\cos\psi > 0.5$). The lower panel of Figure 37 shows monthly ensemble averaged α_s at mid-day (11:00 to 14:00 LT) over the two-year period. As expected, OF appeared 'brighter' than the two forested ecosystems and exhibited strong seasonal variation in α_s. The α_s remained almost constant (~0.1) over the entire two year period for PP as expected for this evergreen forest. The α_s tracked reasonably well the seasonality in leaf area index (LAI) at HW, also shown in Figure 37.

The 'measured' T_s in each ecosystem was determined using the CNR-1 measured emitted long-wave radiation (R_{lo}) using $R_{lo} = \sigma \varepsilon_s T_s^4$, where ε_s can vary across different ecosystems and exhibit seasonal variations within a given ecosystem due to seasonal changes in surface characteristics. Because no precise measurements were locally available for ε_s, we derived an empirical relationship between literature reported α_s and ε_s for crops and forests in temperate regions ($\varepsilon_s = -0.48\alpha_s + 1.04$, $R^2 = 0.97$), and used this derived expression to model seasonal variations in ε_s from measured variations in α_s. We then used these ε_s to compute T_s for each ecosystem. As we show later, even

when considering such changes in ε_s, their overall contribution to δT_s remains small when compared to albedo changes. The measured δT_s reported in Figure 38 suggests a cooling effect if OF is completely converted to PP or HW. Note that the cooling effect by converting OF to PP is roughly double the cooling effect obtained by converting OF to HW (-2.59 ^{o}C versus -1.24 ^{o}C in annual averages).

In Equation (6-5), terms II through IV can be determined from the flux measurements. However, the η in Term I must be calculated separately from α and g_a. The variations in α are shown in Figure 38 for each ecosystem. Here, α varied from ~0.45-0.50 during the winter seasons but increased up to 0.9-1.0 during the summer months. Also, g_a was computed from measured H and $(T_s - T_a)$ at each ecosystem (not shown) and then used, along with α, in the calculation of η. Once all the components in Equation (6-5) are resolved, we examine how land-cover changes, quantified by changes in η, α_s, G_s and ε_s in Equation (6-5), impact δT_s.

Figure 39 shows the calculated seasonal variation in each of these four components from 2004 to 2005 for both land cover conversions. It is clear that both - the surface heat flux component (term III) and the thermal emissivity component (term IV) remain smaller than the other two components. Furthermore, these two components act in opposite directions and almost tend to cancel each other so that their sum may be neglected on annual time scales, at least when compared to the albedo effect. Hence, it is safe to say from Figure 39 that δT_s is primarily dominated by the interplay between the

two larger yet competing effects: albedo (term II) and the physiology/aerodynamics (term I).

As for the albedo component (term II), it is the major warming factor for both land-cover conversions. We found that the warming effects due to albedo reduction following a conversion from OF to PP or OF to HW is much stronger in winter seasons when compared to summer seasons because albedo in OF is much higher than the two forested vegetations. The changes in albedo alone can warm the surface annually by 0.68 ^{o}C for an OF to PP conversion, and by 0.5 ^{o}C for an OF to HW conversion. As for the eco-physiological/aerodynamics component (term I), it is the major cooling factor for both land-cover changes. The long-term cooling effects, estimated from Figure 39, are about -3.27 ^{o}C for OF to PP conversion and -1.73 ^{o}C for OF to HW conversion (see Table 8 for summary).

In conclusion, converting OF to PP or HW results in a surface cooling effect on annual time scales. Furthermore, unlike the Boreal ecosystem study by *Betts* [2000], this cooling pattern is accompanied by increased CO_2 sequestration as evidenced by the EC based net ecosystem CO_2 exchange comparisons reported in *Stoy et al*.[2006].

Table 8: Comparisons of the two-year averaged δT_s (^{o}C) for the two land cover conversions: OF to PP and OF to HW. The contributions from the 4 components in the model (Equation (6-5)) on δT_s are presented. Here, OF is abandoned old field, PP is the pine plantation, and HW is the second-growth hardwood forest.

δT_s (^{o}C)	From OF to PP	From OF to HW
δT_s from longwave	-2.59	-1.24
δT_s from model	-2.22	-1.38
(i) Ecophysiological	-3.27	-1.73
(2) Surface albedo	0.68	0.50
(3) Surface heat flux	0.22	0.15
(4) Emissivity	-0.22	-0.16

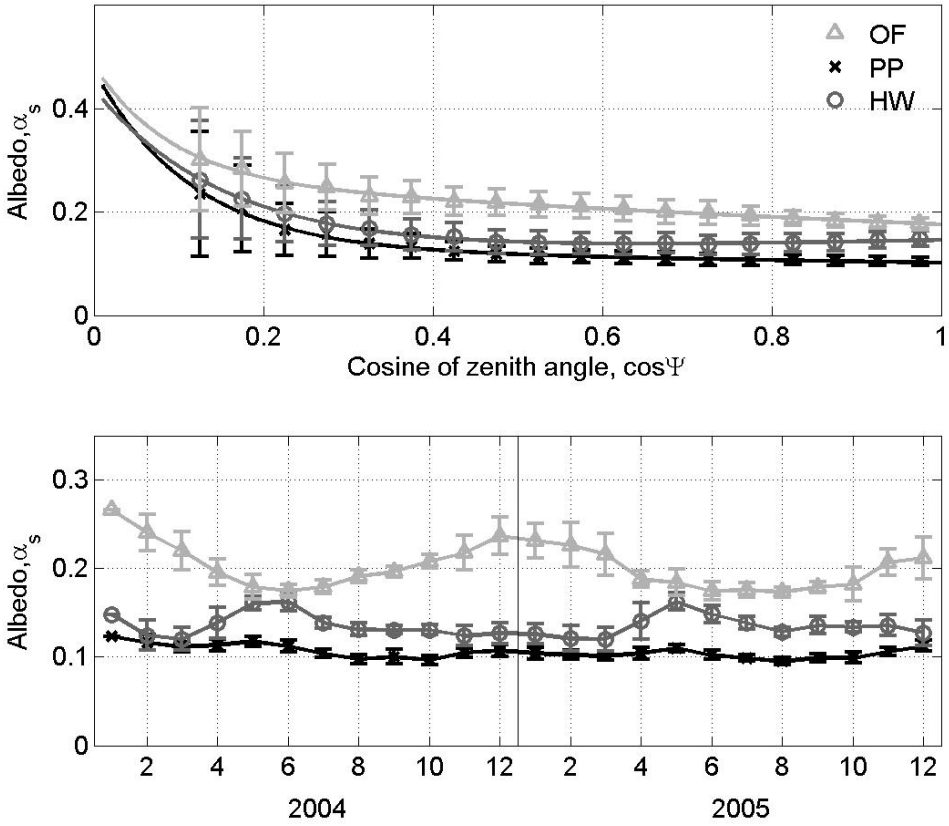

Figure 37: The relationship between ensemble-averaged albedo and cosine of the zenith angle for the three ecosystems (upper panel), and the mid-day (1100LT to 1400LT) monthly ensemble-averaged albedo from 2004 to 2005 in the three ecosystems (lower panel). Vertical bars are one standard deviation around the ensemble averages.

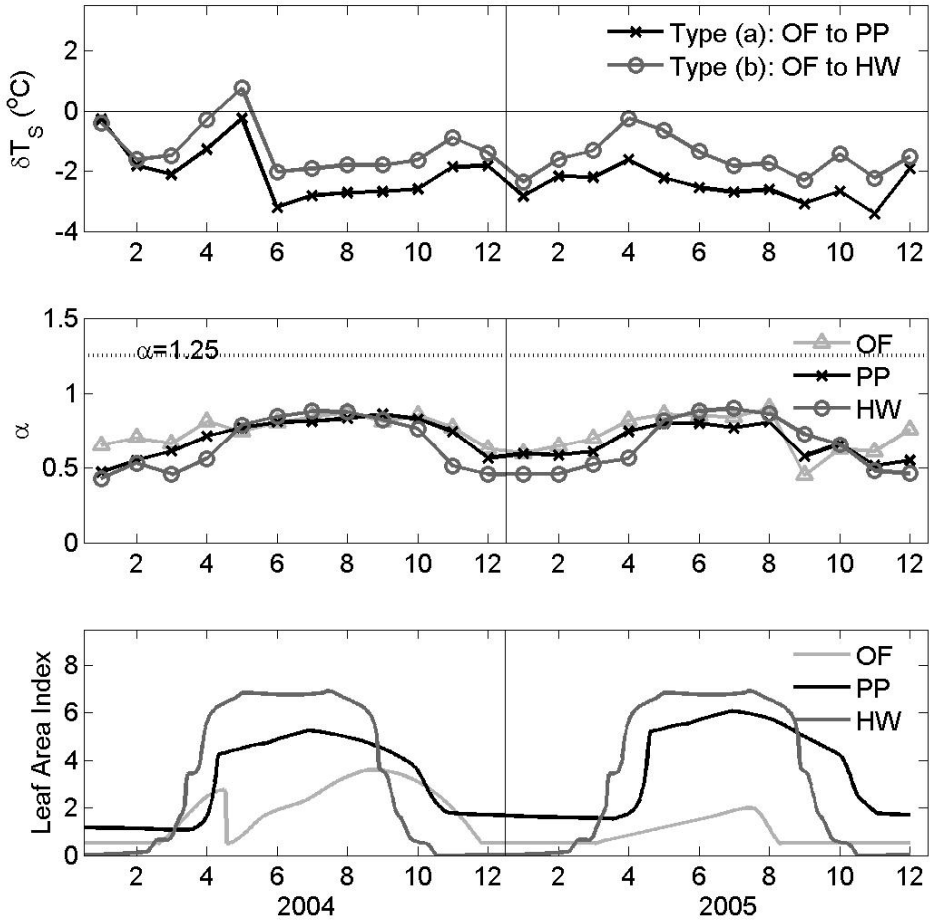

Figure 38: Upper Panel: Monthly averaged changes in surface temperature estimated from the longwave radiation measurements for both land-cover changes (OF to PP and OF to HW). Middle: the variation of the Priestley-Taylor α in different ecosystems. The maximum value of $\alpha = 1.26$ is shown as a reference. Lower Panel: the variation in measured leaf area index (LAI, m^2 m^{-2}) at the three ecosystems. The large LAI excursions in OF are due to annual mowing for hay and to check woody encroachment.

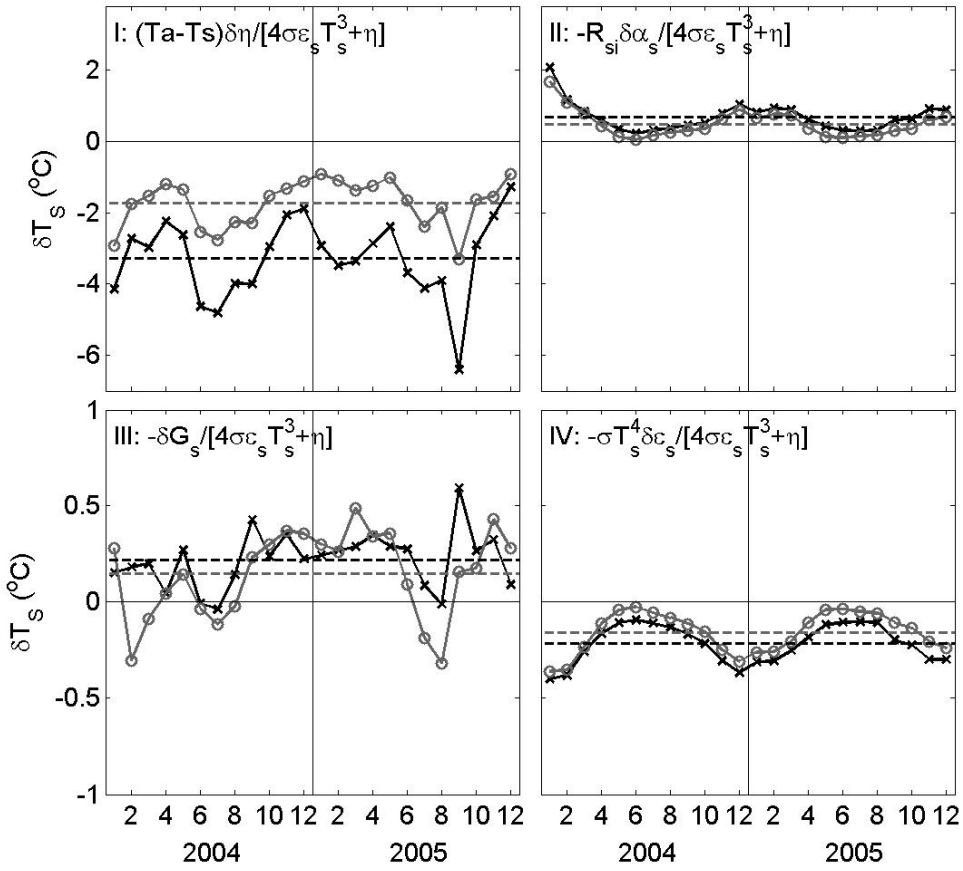

Figure 39: The contribution of each of the four components in Equation (6-5) to δT_s. The black lines and dark gray lines refer to an OF to PP conversion and an OF to HW conversion, respectively, and the dashed lines represent long-term averages.

7. Conclusion

Major conclusions for each research topic discussed in Chapters 2 to 6 are summarized as follows:

(1) In Chapter 2, annual forest floor efflux modeled with CSO_E averaged 111 gCm^{-2} less than that estimated using chambers during these years of study (2001: 1224 v. 1328 gCm^{-2}; 2002: 1127 v. 1230 gCm^{-2}; 2003: 1473 v. 1599 gCm^{-2}). The modeled ecosystem respiration exceeded estimates from eddy-covariance measurements (uncorrected for storage fluxes) by at least 25%, even at high friction velocities. In addition, this study showed that the CSO_E annual nighttime respiration values agree well with independent estimates derived from the intercept of the ecosystem light-response curve from daytime eddy covariance CO_2 flux measurements.

(2) In Chapter 3, the study concluded that (i) sensible heat flux predictions were most biased with respect to eddy-covariance measurements when using the well-mixed scalar assumption (WMA), (ii) first-order closure schemes are sufficient for reproducing the seasonal to inter-annual variations in scalar fluxes provided the canonical length scale of turbulence is properly specified, (iii) second-order closure models best agree with measured mean scalar concentration (and temperature) profiles inside the canopy as well as scalar fluxes above the canopy, (iv) there were no clear gains in predictive skills when using third-order closure schemes over their second-order closure counterpart. At inter-annual time scales, we showed that biases in modeled scalar fluxes incurred by using the WMA

exceed those incurred when correcting for the seasonal amplitude in the maximum carboxylation capacity ($V_{cmax,25}$) provided its mean value is properly specified. The role of local thermal stratification inside the canopy and possible simplifications in decoupling scalar transfer from the generation of the flow statistics are also discussed.

(3) In Chapter 4, it was demonstrated via data analysis that convective precipitation events have significantly larger intensities (mean = 2.1 mm per 30 min) when compared to their non-convective counterparts (mean = 1.1 mm per 30 min). Interestingly, the statistics of convective precipitation events, including total precipitation, mean intensity, and maximum intensity, are statistically different when convective precipitation is triggered by moist and dry soil conditions, but are robust to the triggering mechanism in duration. Using the data, we also showed that a 'boundary line' emerges such that for a given soil moisture state, air relative humidity must exceed a defined minimum threshold before convective precipitation is realized.

(4) In Chapter 5, the study found that the sensitivity of PP to soil moisture deficit enhances the trigger of convective rainfall relative to HW and OF, with enhancements of about 25 % and 30 % for dry moisture states, and 5 % and 15 % for moist soil moisture states, respectively. We discuss the broader implications of these findings on potential modulations of convective rainfall triggers induced by projected large-scale changes in timberland composition within the Southeastern United States.

(5) In Chapter 6, it was shown that changes in albedo alone can *warm* the surface by 0.68 ^{o}C for an old-field to pine plantation (OF to PP) conversion, and by 0.5 ^{o}C for an OF to a hardwood forest (HW) conversion on annual time scales. However, over the same period, changes in eco-physiological/aerodynamics attributes alone can *cool* the surface by about 3.27 ^{o}C for an OF to PP conversion and 1.73 ^{o}C for an OF to HW conversion. Both simplified model calculations and measurements suggest an over-all surface temperature change that is roughly -2.2 ^{o}C when OF is converted to PP and -1.3 ^{o}C when OF is converted to HW. Furthermore, unlike Boreal ecosystems, such a land use conversion not only resulted in surface cooling but was accompanied by increased CO_2 sequestration.

Much of the work here has focused on static vegetation structure (even when exploring one land cover to another), planar homogeneous ecosystems, and 1-dimensional treatment of atmospheric models. Logical extensions of this work include:

(1) the incorporation of complex topopgraphy

(2) accounting for heterogeneous canopies, including dynamic phases of the land-cover changes (e.g. woody encroachment).

(3) coupling the integrated ecosystem function (i.e. fluxes) with ecosystem structure (biomass, height, leaf-area) so as to resolve this 2-way interaction.

(4) Adding soil-plant hydrodynamics and plant stress

Appendix

Appendix A: Second-order Closure approximation

A.1 Momentum and Reynolds stress budget equations

Wilson and Shaw [1977] proposed a set of higher order closure approximations to parameterize each term in the momentum $\overline{u_i}$ equations, and utilized a method similar to *Mellor* [1973] for the closure the Reynolds stress $\overline{u_i' u_j'}$ equations. For higher-order closure approximation schemes, the gradient diffusion approximation introduced by *Mellor* [1973] and *Donaldson* [1973] is employed to close each term in the governing equations of fluxes.

Katul and Albertson [1998] simplified *Wilson and Shaw* [1977] model by assuming horizontal homogeneity and steady state conditions and obtained the following closure approximation equations to describe the full budget of the longitudinal wind velocity component and corresponding Reynolds stresses.

$$\frac{\partial \overline{u}}{\partial t} = 0 = -C_d \cdot a \cdot \overline{u}^2 - \frac{\partial \overline{u' w'}}{\partial z} \tag{A1a}$$

$$\frac{\partial \overline{u' w'}}{\partial t} = 0 = -\overline{w' w'} \frac{\partial \overline{u}}{\partial z} - \frac{Q \overline{u' w'}}{3\lambda_2} + C_w Q^2 \frac{\partial \overline{u}}{\partial z} - \frac{\partial \overline{w' u' w'}}{\partial z} \tag{A1b}$$

$$\frac{\partial \overline{u' u'}}{\partial t} = 0 = -2\left(\overline{u' w'} \frac{\partial \overline{u}}{\partial z} + \overline{u} \frac{\partial \overline{u' w'}}{\partial z} \right) - \frac{Q}{3\lambda_2} \left(\overline{u' u'} - \frac{Q^2}{3} \right) - \frac{2}{3} \frac{Q^3}{\lambda_3} - \frac{\partial \overline{w' u' u'}}{\partial z} \tag{A1c}$$

$$\frac{\partial \overline{v'v'}}{\partial t} = 0 = -\frac{Q}{3\lambda_2}\left(\overline{v'v'} - \frac{Q^2}{3}\right) - \frac{2}{3}\frac{Q^3}{\lambda_3} - \frac{\partial \overline{w'v'v'}}{\partial z} \qquad \text{(A1}d\text{)}$$

$$\frac{\partial \overline{w'w'}}{\partial t} = 0 = -\frac{Q}{3\lambda_2}\left(\overline{w'w'} - \frac{Q^2}{3}\right) - \frac{2}{3}\frac{Q^3}{\lambda_3} + \frac{2g}{\overline{T}}\overline{w'T'} - \frac{\partial \overline{w'w'w'}}{\partial z} \qquad \text{(A1}e\text{)}$$

where Q is the characteristic turbulent velocity (square root of the mean turbulent kinetic energy $\sqrt{\overline{u_i'u_i'}}$), and C_d is the drag coefficient. Parameters λ_1, λ_2, and λ_3 are the characteristic length scales as discussed in *section 2.1*. These three length scales are determined from the mixing length, $L(z)$ ($\lambda_i = a_i \times L$, where i = 1,2,3), where a_i and C_w are the constants to be determined in *Appendix A.2*.

In equation (A1), the closure approximations of all the triple correlation terms are described in *Appendix A.3*.

A.2 Determination of closure constants and the stability-dependency

Applying the linear relationship between σ_{u_i} and u^* above the canopy in the neutral surface layer results in:

$$\begin{aligned}
\sigma_u &= A_u \cdot u^* \\
\sigma_v &= A_v \cdot u^* \\
\sigma_w &= A_w \cdot u^* \\
Q &= \sqrt{A_u^2 + A_v^2 + A_w^2} \cdot u^* = A_Q \cdot u^*
\end{aligned} \qquad \text{(A2)}$$

where A_u, A_v, and A_w could be obtained from the eddy covariance measurement [*Katul and Albertson*, 1998; *Shaw*, 1977].

To derive the relationship between A_w and atmospheric stability, we used the EC data from 2001 to 2003 and plotted A_w against the stability ($\zeta = {(h-d)}/{L}$, where d is the zero-plane displacement derived from $\overline{u'w'}$ profiles[*Katul and Albertson*, 1998]), as shown in Figure A1. The fitted curve is

$$A_w = 1.15 + 0.23 \cdot \zeta^{0.6} \qquad \text{(A3}a\text{)}$$

and is employed to quantify A_w for different atmospheric stability conditions. The number 1.15 in equation (A3*a*) is the mean value of A_w at neutral stability. The variations of A_u and A_v for different stability conditions were obtained using the same procedure:

$$A_u = 1.96 + 0.49 \cdot \zeta^{0.5} \qquad \text{(A3}b\text{)}$$

$$A_v = 1.94 + 0.47 \cdot \zeta^{0.5} \qquad \text{(A3}c\text{)}$$

The corresponding value of A_Q then can be derived from A_u, A_v and A_w.

To quantify the effect of canopy structure and atmospheric stability on the momentum component profiles, we present the vertical distributions of modeled σ_w/u^* and Q/u^* for two distinct plant area density distributions and for both neutral ($|\zeta| \le 0.05$) and stable ($\zeta = 1.2$) stability conditions in Figure A.2. From the figure, we found that atmospheric stability is much more important than the variations of PAD.

By using the parameters derived above, *Katul and Albertson* [1998] summarize the following equations,

$$
\begin{aligned}
&a_2^{-1}\left(A_w^2-\frac{A_Q^2}{3}\right)+a_3^{-1}\left(2A_Q^2\right)+C(0)=0\\
&a_2^{-1}\left(A_u^2-\frac{A_Q^2}{3}\right)+a_3^{-1}\left(2A_Q^2\right)+C(0)=\frac{6}{A_Q}\\
&a_2^{-1}\left(\frac{1}{3A_Q^2}\right)+a_3^{-1}(0)+C(1)=\left(\frac{A_w}{A_Q}\right)^2
\end{aligned}
\tag{A4}
$$

to determine the value of closure constant a_2, a_3 and C_w. The value of a_1 is determined by the equation $a_1 = {}^{1}\!/_{A_Q}$ [*Katul and Albertson*, 1998; *Shaw et al.*, 1974]

A.3 Second-order closure parameterization for triple correlations

For the triple velocity correlation components, the general form of the second-order closure model parameterizations are [*Katul and Albertson*, 1998; *Mellor*, 1973]:

$$
\overline{u_i' u_j' u_k'} = -Q\lambda_1\left(\frac{\partial\overline{u_i' u_j'}}{\partial x_k}+\frac{\partial\overline{u_j' u_k'}}{\partial x_i}+\frac{\partial\overline{u_k' u_i'}}{\partial x_j}\right) \tag{A5}
$$

The one-dimensional closure approximation for the transport of scalar fluxes and buoyant terms can be express as follows:

$$
\begin{aligned}
&\overline{w' w' C'} = -Q\lambda_1\left(\frac{\partial\overline{F}}{\partial z}\right)\\
&\overline{w' w' T'} = -Q\lambda_1\left(\frac{\partial\overline{F_T}}{\partial z}\right)
\end{aligned}
\tag{A6}
$$

and

$$\overline{w'T'C'} = -Q\lambda_1\left(\frac{\partial\overline{T'C'}}{\partial z}\right)$$
$$\overline{w'T'T'} = -Q\lambda_1\left(\frac{\partial\overline{T'T'}}{\partial z}\right) \qquad \text{(A7)}$$

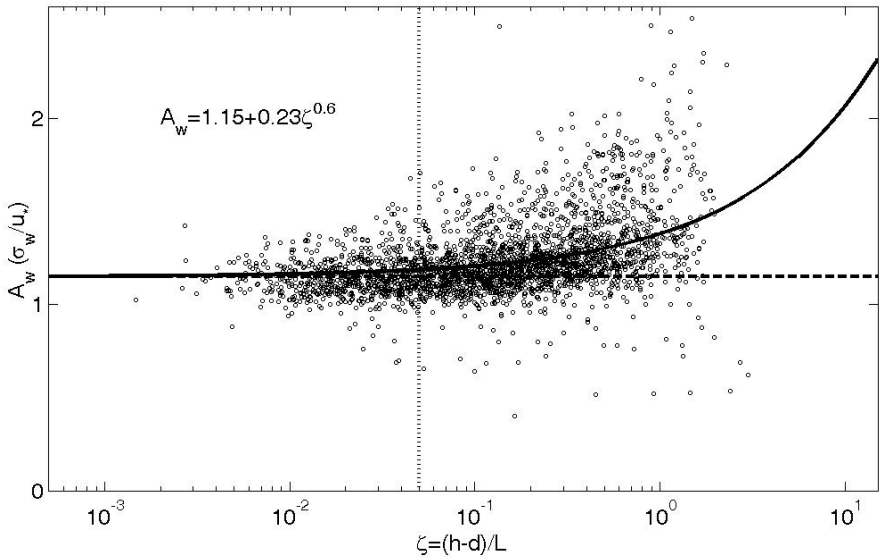

Figure 40: The relationship between A_w and atmospheric stability parameter ζ. All the data points are from EC measurements above the canopy from 2001 to 2003. Neutral atmospheric stability conditions are defined when the absolute value of ζ is less than 0.05 (the dotted vertical line shown in the figure) [*Siqueira and Katul*, 2002]. The dashed line represents the mean value (1.15) of A_w under neutral atmospheric stability, and the solid line is the fitted curve.

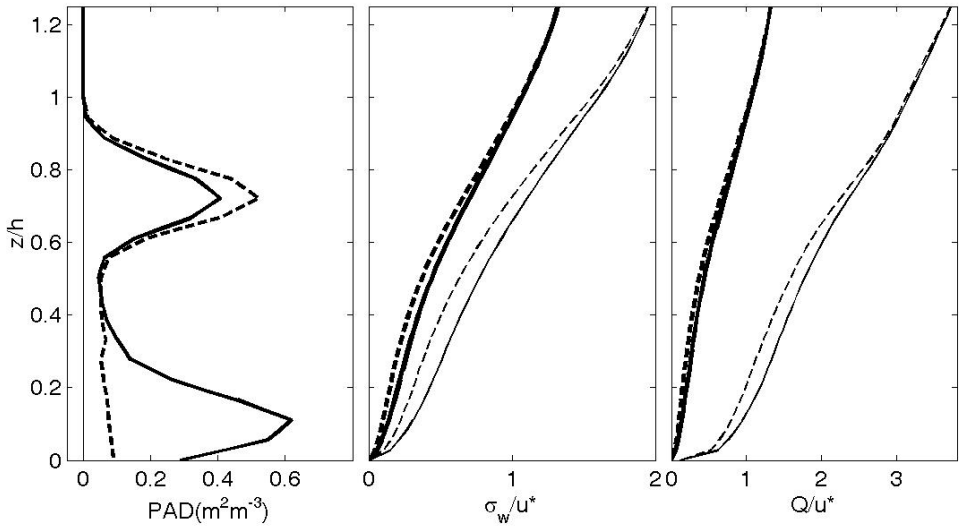

Figure 41: Sensitivity of plant area density (PAD) and atmospheric stability to closure model predictions. The left panel shows the two end members of the measured PAD profiles (solid line for day 124 and dashed line for day 329). The bold lines and thin lines in the middle and right panels respectively represent neutral ($|\zeta| \leq 0.05$) and stable ($\zeta = 1.2$) atmospheric stability conditions for $\sigma_w/u*$ and $Q/u*$. The solid lines and dashed lines in the middle and right panels correspond to the PAD profiles shown in the left panel.

Appendix B: Theoretical and practical issues for estimating storage flux at a single tower

The u^* thresholds are often employed for multiple reasons:

1) To eliminate non-turbulent conditions. For example, [*Cava et al.*, 2004] showed how canopy waves are generated and how they can transport significant CO_2 inside to outside and outside to inside the canopy and over periods that if not properly captured by the averaging interval can lead to negative CO_2 fluxes (i.e. photosynthesis like) at night. Employing a u^* threshold is primarily to ensure that runs collected under such non-turbulent conditions are removed.
2) To reduce high frequency losses. Eddy-covariance fluxes themselves suffer from high-frequency co-spectral losses under moderately stable and very stable atmospheric conditions due to instrument separation distances, limited sampling frequency, and path length averaging by instruments. So, filtering by u^* eliminates those runs. There are ways to correct for some of those losses using temperature time series data – but the similarity between CO_2 and temperature breaks down even at high frequency for very stable conditions (see *Katul and Parlange* [1994]).
3) To minimize the effect of storage flux on the estimate of ecosystem respiration from eddy-covariance data. The difficulty in estimating the storage flux that is most consistent with the scalar continuity equation can be demonstrated as follows: the depth-integrated 1-D continuity equation:

$$\int_0^h \frac{\partial \overline{C}}{\partial t} dz = -F(h) + \left[F(0) + \int_0^h \overline{S} dz \right]$$

and this equation is a spatially averaged equation. The term in parentheses is the desired ecosystem respiration (R_E) (spatially-averaged). The origin of the term $\int_0^h S dz$ arises because of spatially averaging (after temporally averaging say over ½ hour) the point equations. Now, to correctly estimate the spatially averaged R_E, one must determine the spatially averaged $\int_0^h \frac{\partial \overline{C}}{\partial t} dz$. Estimating this quantity from a single tower at ½ hourly time step assumes that we have sampled all the volume within the averaging domain numerous times (to ensure sufficient sample size for the purposes of statistical averaging stability). For low winds inside the canopy – this convergence is problematic. For stronger winds (or higher u^* above the canopy), one is likely to sample, at the tower, fluid parcels originating from further distances – thereby ensuring that a bigger volume has been sampled over a 30 minute period at a given point. This is primarily the ergodic hypothesis (in space) – likely to be more accurate at higher u^* than lower u^*. Alternatively, one can construct an ensemble of $\int_0^h \frac{\partial \overline{C}}{\partial t} dz$ for similar u^* and temperature and average those ensemble values assuming that the ensemble average better represents the spatial at the tower when compared to an individual ½ hour run. In all cases, a major

uncertainty remains in the determination of $\int_0^h \frac{\partial \overline{C}}{\partial t} dz$ from a single tower, exasperated by low u^* conditions. This was the main reason for choosing a 14-day ensemble average – to ensure that the spatial average is estimated from ensemble averages rather than ½ hour rums. The 14-day period was chosen because the respiring biomass did not drastically change. There is another practical advantage to using ensemble averages vis-à-vis single runs – which is a reduction in the random error known to contaminate CO_2 concentration samples.

Appendix C: Closure approximation

C.1 Second-order closure parameterization for triple correlations

The triple correlation terms of the turbulent velocity components for the second-order closure model are represented as [*Katul and Albertson*, 1998; *Mellor*, 1973]:

$$\left\langle \overline{u_i' u_j' u_k'} \right\rangle = -Q\lambda_1 \left(\frac{\partial \left\langle \overline{u_i' u_j'} \right\rangle}{\partial x_k} + \frac{\partial \left\langle \overline{u_j' u_k'} \right\rangle}{\partial x_i} + \frac{\partial \left\langle \overline{u_k' u_i'} \right\rangle}{\partial x_j} \right), \tag{C1}$$

Similarly, the second-order closure approximation for the turbulent transport of scalar fluxes and buoyant terms then can be expressed as

$$\begin{aligned} \left\langle \overline{u_i' u_j' \zeta'} \right\rangle &= -Q\lambda_1 \left(\frac{\partial \left\langle \overline{u_j' \zeta'} \right\rangle}{\partial x_i} + \frac{\partial \left\langle \overline{u_i' \zeta'} \right\rangle}{\partial x_j} \right) \\ \left\langle \overline{u_i' T' \zeta'} \right\rangle &= -Q\lambda_1 \left(\frac{\partial \left\langle \overline{T' \zeta'} \right\rangle}{\partial x_i} \right) \end{aligned} . \tag{C2}$$

C.2 Third-order closure parameterization

The closure expression for the triple correlation terms in equation (12) is derived from a simplified steady-state budget described in Meyers and Paw U [1986]:

$$\frac{\partial\left\langle\overline{u_i'u_j'w'}\right\rangle}{\partial t}=-\left\langle\overline{u_i'w'w'}\right\rangle\frac{\partial\left\langle\overline{u_j}\right\rangle}{\partial z}-\left\langle\overline{u_j'w'w'}\right\rangle\frac{\partial\left\langle\overline{u_i}\right\rangle}{\partial z}-\left\langle\overline{w'w'}\right\rangle\frac{\partial\left\langle\overline{u_i'u_j'}\right\rangle}{\partial z}$$
$$-\left\langle\overline{u_i'w'}\right\rangle\frac{\partial\left\langle\overline{w'u_j'}\right\rangle}{\partial z}-\left\langle\overline{u_j'w'}\right\rangle\frac{\partial\left\langle\overline{w'u_i'}\right\rangle}{\partial z}-\left\langle\overline{u_i'u_j'\frac{\partial p'}{\partial z}}\right\rangle-\left\langle\overline{u_i'w'\frac{\partial p'}{\partial z}}\right\rangle \quad , \qquad \text{(C3)}$$
$$-\left\langle\overline{u_j'w'\frac{\partial p'}{\partial z}}\right\rangle-\left\langle\overline{u_i'w'}\right\rangle\left\langle\overline{\frac{\partial p'}{\partial x_j}}\right\rangle-\left\langle\overline{u_j'w'}\right\rangle\left\langle\overline{\frac{\partial p'}{\partial x_i}}\right\rangle-M_{ij3}=0$$

where M_{ij3} is the dissipation rate and is expressed as:

$$M_{ij3}=2\nu\left\langle w'\overline{\frac{\partial u_i'}{\partial x_k}\frac{\partial u_j'}{\partial x_k}}+u_i'\overline{\frac{\partial w'}{\partial x_k}\frac{\partial u_j'}{\partial x_k}}+u_j'\overline{\frac{\partial u_i'}{\partial x_k}\frac{\partial w'}{\partial x_k}}\right\rangle. \qquad \text{(C4)}$$

A simplified return-to-isotropic model introduced by Andre et al. [1981] is applied to parameterize the pressure and molecular terms in equation (C3)

$$\left\langle\overline{u_i'u_j'\frac{\partial p'}{\partial z}}\right\rangle+\left\langle\overline{u_i'w'\frac{\partial p'}{\partial z}}\right\rangle+\left\langle\overline{u_j'w'\frac{\partial p'}{\partial z}}\right\rangle+M_{ij3}=\frac{C_8\left\langle\overline{u_i'u_j'w'}\right\rangle}{\tau}. \qquad \text{(C5)}$$

As a result, after rearranging equations (C3) and (C5), the general form of the triple correlation terms then can be represented as:

$$\left\langle\overline{u_i'u_j'w'}\right\rangle=-\frac{\tau}{C_8}\left(\left\langle\overline{u_i'w'w'}\right\rangle\frac{\partial\left\langle\overline{u_j}\right\rangle}{\partial z}+\left\langle\overline{u_j'w'w'}\right\rangle\frac{\partial\left\langle\overline{u_i}\right\rangle}{\partial z}\right.$$
$$\left.+\left\langle\overline{w'w'}\right\rangle\frac{\partial\left\langle\overline{u_i'u_j'}\right\rangle}{\partial z}+\left\langle\overline{u_i'w'}\right\rangle\frac{\partial\left\langle\overline{w'u_j'}\right\rangle}{\partial z}+\left\langle\overline{u_j'w'}\right\rangle\frac{\partial\left\langle\overline{w'u_i'}\right\rangle}{\partial z}\right). \qquad \text{(C6)}$$

Likewise, the steady-state expression for the triple correlation terms involved in the scalar term and temperature fluctuation that can be derived following the same procedure described in Meyers and Paw U [1987]:

$$\left\langle \overline{u_i' u_j' \zeta'} \right\rangle = -\frac{\tau}{C_8}\left(\left\langle \overline{u_i' u_j' w'} \right\rangle \frac{\partial \left\langle \overline{\zeta} \right\rangle}{\partial z} + \left\langle \overline{w' u_j' \zeta'} \right\rangle \frac{\partial \left\langle \overline{u_i} \right\rangle}{\partial z} + \left\langle \overline{w' u_i' \zeta'} \right\rangle \frac{\partial \left\langle \overline{u_j} \right\rangle}{\partial z} + \left\langle \overline{w' u_i'} \right\rangle \frac{\partial \left\langle \overline{u_j' \zeta'} \right\rangle}{\partial z} + \left\langle \overline{w' u_j'} \right\rangle \frac{\partial \left\langle \overline{u_i' \zeta'} \right\rangle}{\partial z} + \left\langle \overline{w' \zeta'} \right\rangle \frac{\partial \left\langle \overline{u_i' u_j'} \right\rangle}{\partial z} \right) \tag{C7}$$

and

$$\left\langle \overline{u_i' T' \zeta'} \right\rangle = -\frac{\tau}{C_8}\left(\left\langle \overline{w' u_i' \zeta'} \right\rangle \frac{\partial \left\langle \overline{T} \right\rangle}{\partial z} + \left\langle \overline{w' u_i' T'} \right\rangle \frac{\partial \left\langle \overline{\zeta} \right\rangle}{\partial z} + \left\langle \overline{w' T' \zeta'} \right\rangle \frac{\partial \left\langle \overline{u_i} \right\rangle}{\partial z} + \left\langle \overline{w' u_i'} \right\rangle \frac{\partial \left\langle \overline{T' \zeta'} \right\rangle}{\partial z} + \left\langle \overline{w' T'} \right\rangle \frac{\partial \left\langle \overline{u_i' \zeta'} \right\rangle}{\partial z} + \left\langle \overline{w' \zeta'} \right\rangle \frac{\partial \left\langle \overline{u_i' T'} \right\rangle}{\partial z} \right) . \tag{C8}$$

Appendix D: Light attenuation model

D.1 Partitioning of incoming shortwave radiation

The incoming shortwave radiation received by the surface is composed of two portions: beam S_{b0} and diffuse S_{d0} components. To quantify the partitions of S_{b0} and S_{d0}, the atmospheric transmissivity (or clearness index) K_a needs to be determined and was estimated as

$$K_a = \frac{S_0}{S_{sc} \sin\beta}, \tag{D1}$$

where S_0 is the measured incident radiation on the surface, S_{sc} is the solar radiative flux density normal to the solar beam outside the atmosphere, and $\sin\beta$ is the solar elevation. [*Erbs et al.*, 1982; *Goudriaan and van Laar*, 1994; *Leuning et al.*, 1995]:

Once K_a is determined from S_0, the fraction of diffuse component $f_d = S_{d0} / S_0$ can be quantified based on the experimental relationship by Erbs et al. (1982):

$$\begin{cases} f_d = 1.0 - 0.09K_a & \text{if } K_a \le 0.22 \\ f_d = 0.95 - 0.16K_a + 4.38K_a^{\,2} - 16.63K_a^{\,3} + 12.33K_a^{\,4} & \text{if } 0.22 < K_a \le 0.8 \\ f_d = 0.16 & \text{if } K_a > 0.8 \end{cases}. \tag{D2}$$

Then S_{b0} and S_{d0} on the top of the canopy is calculated from f_d using:

$$\begin{cases} S_{b0} = S_0 \cdot (1 - f_d) \\ S_{d0} = S_0 \cdot f_d \end{cases}. \tag{D3}$$

D.2 Radiation attenuation calculation

Beam component

The extinction coefficient of the beam component, K_b, for an ellipsoidal leaf distribution can be determined as [*Campbell*, 1986; *Campbell and Norman*, 1998]:

$$K_b(\psi) = \frac{(x^2 + \tan^2\psi)^{0.5}}{x + 1.774(x + 1.182)^{-0.733}}, \quad \text{(D4)}$$

where ψ is the solar zenith angle; x is the leaf angle distribution index, assumed unity for spherical leaf angle distribution, which is reasonable for the coniferous foliage [*Schafer et al.*, 2003]. The fraction (τ_b, or transmission coefficient) for incoming beam from a given ψ at different levels is given as:

$$\tau_b(\psi) = \exp\left[-K_b(\psi)\, L_t(z)\, \Pi\right], \quad \text{(D5)}$$

where $L_t(z)$ is the cumulative PAD above the z, and Π is the clumping factor due to the shading effect by other leaves [*Stenberg*, 1998]. The direct beam absorbed at level z can be expressed as:

$$S_{abs,b}(z) = S_{bo}\, K_b\, \alpha, \quad \text{(D6)}$$

where α is the absorptivity of the leaves for a given radiative waveband, which is ~ 0.2 for VIS, and ~ 0.8 for NIR [*Campbell and Norman*, 1998].

Diffuse component

To determine the extinction coefficient of diffuse radiation (K_d) we approximated the fitted curve as a function of $L_t(z)$ for $x=1$ after Campbell and Norman [1998]:

$$\begin{cases} K_d(L_t) = -0.035 \cdot \log_{10}{}^2 L_t(z) - 0.16 \cdot \log_{10} L_t(z) + 0.82 & \text{if } L_t > 0.01 \\ K_d(L_t) = 1 & \text{if } L_t \le 0.01 \end{cases}. \quad \text{(D7)}$$

The absorbed diffuse radiation $S_{abs,d}(z)$ can be expressed as:

$$S_{abs,d}(z) = S_{do} \cdot \alpha^{0.5} \cdot K_d \cdot (1-\rho_{cd}) \cdot \tau_d ,$$

(D8)

where ρ_{cd} is the canopy reflection coefficient for diffuse component, and τ_d is the transmission coefficient for the diffuse component and is given as:

$$\tau_d = \exp\left[-\alpha^{0.5} \cdot K_d(L_t) \cdot L_t(z)\right]. \quad \text{(D9)}$$

Scattered component inside the canopy

The total beam transmitted and scattered through the canopy to a given depth $L_t(z)$ can be derived using the beam extinction coefficient (equation (D2)):

$$\tau_s(\psi) = \exp\left[-\alpha^{0.5} K_{be}(\psi) L_t(z) \Pi\right]. \quad \text{(D10)}$$

Therefore, the absorbed transmitted/scattered radiation at a given depth $L_t(z)$ can be expressed as:

$$S_{abs,s}(z) = S_{b0} \cdot \left[\alpha^{0.5} K_b (1-\rho_{cb}) \tau_s - K_b \alpha \tau_b\right]. \quad \text{(D11)}$$

D.3 Long-wave radiation inside the canopy volume

The isothermal net long-wave radiation [*Leuning et al.*, 1995] at the top of the canopy can be represented as:

$$R_{L0} = \left(\varepsilon_c - \varepsilon_{atm}\right)\sigma T_0^{\,4}, \tag{D12}$$

where ε_c (~ 0.97) is the bulk canopy emissivity, σ is the Stephan Boltzmann constant, T_0 is the air temperature at the canopy top, and ε_{atm} is the sky emissivity empirically given by [*Brutsaert*, 1975]:

$$\varepsilon_{atm} = 0.642 \cdot \left(e_0 / T_0\right)^{1/7}, \tag{D13}$$

where e_0 is water vapor pressure at the top of the canopy.

Once R_{L0} is obtained, the isothermal net long-wave radiation through the canopy volume is estimated as [*Leuning et al.*, 1995]:

$$R_L\left(z\right) = R_{L0} \cdot K_d \exp\left[-K_d\, L_t(z)\right]. \tag{D14}$$

Appendix E: Forest Floor Boundary Conditions

For the mean velocity, the no-slip boundary condition was imposed at the forest floor. For all higher order flow statistics, a free-slip condition was assumed (i.e. $\partial(.)/\partial z = 0$). As for CO_2, the forest floor efflux (F_{ff}), derived by fitting chamber respiration measurements to soil temperature (T_{soil}, in ^{o}C) and soil moisture (θ, in $m^3\ m^{-3}$) was used [*Palmroth et al.*, 2005]. The canonical form of the regression equation used to fit the chamber measurements is:

$$F_{ff}(T_{soil}, \theta) = R_b e^{a_1 T_{soil}} \left[1 - e^{(-b\theta + c)}\right] \quad \text{(E1)}$$

where R_b is the base respiration, a_1 is the temperature sensitivity ($Q_{10} = e^{a_1 \times 10}$) when soil moisture content is not limiting, and the constants b and c are soil moisture reduction parameters. The respiration parameters for 2001 to 2003 were given in Palmroth et al. [2005] and summarized by Juang et al. [2006]. For 2004-2005, these parameters were $R_b = 0.817$, $a_1 = 0.103$, $b = -31.121$, $c = 4.628$ for 2004, and $R_b = 0.548$, $a_1 = 0.118$, $b = -29.511$, $c = 3.301$ for 2005.

As for the latent heat flux from the forest floor (LE_{ff}), it is expressed as a function of the Bowen ratio β_o, and given by

$$LE_{ff} = \frac{1}{1 + \beta_o}\left(R_{n,0} - G\right) \quad \text{(E2)}$$

where $R_{n,0}$ is the forest floor net radiation estimated from the radiative attenuation model in section **3.3** and **Appendix D**, and G is the soil heat flux simply

calculated from the measured soil temperature T_{soil} at 10 cm, air temperature just above the ground, and the mean thermal conductivity for soil (~0.5 W m^{-2} K^{-1}). Because the soil heat flux is small, we did not correct for the heat storage in the upper soil layer. The value of β_o was computed from the surface gradients of air temperature ($\left(\partial\overline{T}/\partial z\right)_s$ and humidity $\left(\partial\overline{q}/\partial z\right)_s$) using

$$\beta_o = \frac{C_p}{L_v}\frac{\left(\partial\overline{T}/\partial z\right)_s + \Gamma_d}{\left(\partial\overline{q}/\partial z\right)_s}, \tag{E3}$$

where Γ_d is the dry adiabatic lapse rate. The surface gradients above were extrapolated from the measured mean water vapor concentration and temperature data. After LE_{ff} is determined, the forest floor sensible heat flux (H_{Sff}) can be estimated as a residual using $H_{Sff} = R_{n,0} - G - LE_{ff}$.

References

Aber, J. D., P. B. Reich, and M. L. Goulden (1996), Extrapolating leaf CO_2 exchange to the canopy: A generalized model of forest photosynthesis compared with measurements by eddy correlation, *Oecologia*, *106*, 257-265.

Andre, J. C., P. Lacarrere, and K. Traore (1981), Pressure effects on triple correlations in turbulent convective flows, in *Turbulent Shear Flows III*, edited, pp. 243-252, Springer-Verlag, Berlin.

Andrews, J. A., K. G. Harrison, R. Matemala, and W. H. Schlesinger (1999), Separation of root respiration from total soil respiration using ^{13}C labeling during Free-Air-CO_2 Enrichment (FACE), *Soil Science Society of America Journal*, *63*, 1429-1435.

Atlas, R., N. Wolfson, and J. Terry (1993), The effect of SST and soil moisture anomalies on the GLA model simulations of the 1988 U.S. summer drought, *Journal of Climate*, *6*, 2034-2048.

Baidya Roy, S., G. C. Hurtt, C. P. Weaver, and S. W. Pacala (2003), Impact of historical land cover change on the July climate of the United States, *Journal of Geophysical Research-Atmospheres*, *108(D24)*, 4793-4806.

Baldocchi, D. (1992), A Lagrangian random-walk model for simulating water vapour, CO_2 and sensible heat flux densities and scalar profiles over and within a soybean canopy, *Boundary-Layer Meteorology*, *61*, 113-144.

Baldocchi, D., C. A.Vogel, and B. Hall (1997), Seasonal variation of carbon dioxide exchange rates above and below a boreal jack pine forest, *Agricultural and Forest Meteorology*, *83*, 147-170.

Baldocchi, D., and T. Meyers (1998), On using eco-physiological, micrometeorological and biogeochemical theory to evaluate carbon dioxide, water vapor and trace gas fluxes over vegetation: a perspetive, *Agricultural and Forest Meteorology*, *90*, 1-25.

Baldocchi, D. D., R. Valentini, S. Running, W. Oechel, and R. Dahlman (1996), Strategies for measuring and modelling carbon dioxide and water vapour fluxes over terrestrial ecosystems, *Global Change Biology*, *2*, 159-168.

Baldocchi, D. D., E. Falge, L. Gu, R. Olson, D. Hollinger, S. Running, P. Anthoni, C. Bernhofer, K. Davis, J. Fuentes, A. Goldstein, G. Katul, B. Law, X. Lee, Y. Malhi, T.

Meyers, J. W. Munger, W. Oechel, K. Pilegaard, H. P. Schmid, R. Valentini, S. Verma, T. Vesala, K. Wilson, and S. Wofsy (2001), FLUXNET: A new tool to study the temporal and spatial variability of ecosystem-scale carbon dioxide, water vapor and energy flux densities, *Bulletin of the American Meteorological Society, 82*, 2415-2435.

Ball, J. T., I. E. Woodrow, and J. A. Berry (1987), A model predicting stomatal conductance and its contribution to the control of photosynthesis under different environmental conditions, in *Progress in Photosynthesis Research*, edited, pp. 221-224, Martinus Nijhoff, Amsterdam, Netherlands.

Battle, M., M. L. Bender, P. P. Tans, J. W. C. White, J. T. Ellis, T. Conway, and R. J. Francey (2000), Global carbon sinks and their variability Inferred from atmospheric O_2 and ^{13}C, *Science, 287*, 2467-2470.

Betts, A. K., R. L. Desjardins, and J. MacPherson (1992), Budget analysis of the boundary layer grid flights during FIFE 1987, *Journal of Geophysical Research-Atmospheres, 97*, 18533-18546.

Betts, R. A. (2000), Offset of the potential carbon sink from boreal forestation by decreases in surface albedo, *Nature, 408*, 187-190.

Bohrer, G., H. Mourad, T. A. Laursen, D. Drewry, R. Avissar, D. Poggi, R. Oren, and G. G. Katul (2005), Finite element tree crown hydrodynamics model (FETCH) using porous media flow within branching elements: A new representation of tree hydrodynamics, *Water Resources Research, 41*(11), W11404.

Bousquet, P., P. Peylin, P. Ciais, C. L. Quere, P. Friedlingstein, and P. P. Tans (2000), Regional changes in carbon dioxide fluxes of land and oceans since 1980, *Science, 290*, 1342-1346.

Brutsaert, W. (1975), On a derivable formula for long-wave radiation from clear skies, *Water Resources Research, 11*, 742-744.

Butnor, J. R., K. H. Johnsen, and R. Oren (2003), Reduction of forest floor respiration by fertilization on both carbon dioxide-enriched and reference 17-year-old loblolly pine stands, *Global Change Biology, 9*, 849-861.

Butnor, J. R., and K. H. Johnsen (2004), Calibrating soil respiration measures with a dynamic flux apparatus using artificial soil media of varying porosity, *European Journal of Soil Science, 55*, 639-647.

Campbell, G. S. (1986), Extinction coefficients for radiation in plant canopies calculated using an ellipsoidal inclination angle distribution, *Agricultural and Forest Meteorology, 36*, 317-321.

Campbell, G. S., and J. M. Norman (1998), in *An Introduction to Environmental Biophysics*, edited, Springer-Verlag, New York, NY.

Cava, D., U. Giostra, M. Siqueira, and G. G. Katul (2004), Organized motion and radiative perturbations in the nocturnal canopy sublayer above an even-aged pine forest, *Boundary-Layer Meteorology*, *112*, 129-157.

Cess, R. D. (1978), Biosphere-albedo feedback and climate modeling, *Journal of the Atmospheric Sciences*, *35*(9), 1765-1768.

Charlson, R. J., F. P. J.Valero, and J. H. Seinfeld (2005), In search of balance, *Science*, *308*, 806-807.

Charney, J., W. J. Quirk, S.-H. Chow, and J. Kornfield (1977), A comparative study of the effects of albedo change on drought in semi-arid regions, *Journal of the Atmospheric Sciences*, *34*, 1366-1385.

Chase, T. N. S., T. G. F. Kittel, M. Zhao, A. J. Pitman, S. W. Running, and R. R. Nemani (2001), Relative climatic effects of landcover change and elevated carbon dioxide combined with aerosols: A comparison of model results and observations, *Journal of Geophysical Research-Atmospheres*, *106(D23)*, 31685-31692.

Clark, K. L., H. L. Gholz, J. B. Moncrieff, F. Cropley, and H. W. Loescher (1999), Environmental controls over net exchanges of carbon dioxide from contrasting Florida ecosystems, *Ecological Applications*, *9*, 936-948.

Collatz, G. J., J. T. Ball, C. Crivet, and J. A. Berry (1991), Physiological and environmental regulation of stomatal conductance, photosynthesis and transpiration: a model that Includes a laminar boundary layer, *Agricultural and Forest Meteorology*, *54*, 107-136.

Corrsin, S. (1974), Limitations of gradient transport models in random walks and in turbulence, *Advances in Geophysics*, *18A*, 25-60

D'Odorico, P., and A. Porporato (2004), Preferential states in soil moisture and climate dynamics, *Proceedings of the National Academy of Sciences of the United States of America*, *101*, 8848–8851.

De Bruin, H. A. R., W. Kohsiek, and B. J. J. M. van den Hurk (1993), A verification of some methods to determine the fluxes of momentum, sensible heat, and water vapor using standard deviation and structure parameter of scalar meteorological quantities, *Boundary-Layer Meteorology*, *63*, 231-257.

De Pury, D. G. G., and G. D. Farquhar (1997), Simple scaling of photosynthesis from leaves to canopies without the errors of big-leaf models, *Plant Cell and Environment*, *20*, 537-557.

Deardorff, J. W. (1972), Numerical investigation of neutral and unstable planetary boundary layers, *Journal of the Atmospheric Sciences*, *29*, 91-115.

Deardorff, J. W. (1978), Closure of second and third moment rate equations for diffusion in homogeneous turbulence, *Physics of Fluids*, *21*, 525-530.

Denmead, O. T., and E. F. Bradley (1985), Flux-gradient relationships in a forest canopy, in *The Forest-Atmosphere Interaction*, edited by B. A. Hutchison and B. B. Hicks, pp. 421-442, D. Reidel Publishing, Dordrecht, The Netherlands.

Detto, M., and G. G. Katul (2006), Simplified expressions for adjusting higher order turbulent statistics obtained from open path gas analyzers, *Boundary-Layer Meteorology*.

Detto, M., N. Montaldo, J. D. Albertson, M. Mancini, and G. G. Katul (2006), Soil moisture and vegetation controls on evapotranspiration in an heterogeneous Mediterranean ecosystem on Sardinia, Italy, *Water Resources Research*, in press.

Donaldson, C. d. (1973), Construction of a dynamic model of the production of atmospheric turbulence and the dispersal of atmospheric pollutants, paper presented at Workshop on Micrometeorology, American Meteorological Society, Boston.

Eagleson, P. S. (1986), The emergence of global-scale hydrology, *Water Resources Research*, *22 (9)*, 6-14.

Ellsworth, D. S. (1999), CO_2 Enrichment in a maturing pine forest: are CO_2 exchange and water status in the canopy affected?, *Plant Cell and Environment*, *22*, 461-472.

Ellsworth, D. S. (2000), Seasonal CO_2 assimilation and stomatal limitations in a *Pinus taeda* canopy, *Tree Physiology*, *20*, 435-445.

Eltahir, E. A. B., and J. S. Pal (1996), Relationship between surface conditions and subsequent rainfall in convective storms, *Journal of Geophysical Research-Atmospheres*, *101 (D21)*, 26237-26246.

Emanuel, L. A., J. D. Neelin, and C. S. Bretherton (1994), On large-scale circulations in convecting atmospheres, *Quarterly Journal of the Royal Meteorological Society*, *120*(519), 1111-1143 Part B.

Emeis, S., C. Munkel, S. Vogt, W. J. Mullerd, and K. Schafer (2004), Atmospheric boundary-layer structure from simultaneous SODAR, RASS, and ceilometer measurements, *Atmospheric Environment*, *38*, 273-286.

Erbs, D. G., S. A. Klein, and J. A. Duffie (1982), Estimation of the diffuse radiation fraction for hourly, daily and monthly average global radiation, *Solar Energy*, *28*, 293.

Fan, S., M. Gloor, J. Mahlman, S. Pacala, J. Sarmiento, T. Takahashi, and P. Tans (1998), A large terrestrial carbon sink in North America Implied by atmospheric and oceanic carbon dioxide data and models, *Science*, *282*, 442-446.

Fang, C., and J. B. Moncrieff (1999), A model for soil CO_2 production and transport 1: Model development., *Agricultural and Forest Meteorology*, *95*, 225-236.

Farquhar, G. D., S. Von Caemmerer, and J. A. Berry (1980), A biochemical model of photosynthetic CO_2 assimilation in leaves of C_3 species, *Planta*, *149*, 79-90.

Feddema, J. J., K. W. Oleson, G. B. Bonan, L. O. Mearns, L. E. Buja, G. A. Meehl, and W. M. Washington (2005), The importance of land-cover change in simulating future climates, *Science*, *310*, 1674-1678.

Findell, K. L., and E. A. B. Eltahir (1999), Analysis of the pathways relating soil moisture and subsequent rainfall in Illinois, *Journal of Geophysical Research-Atmospheres*, *104 (D24)*, 31565-31574.

Findell, K. L., and E. A. B. Eltahir (2003a), Atmospheric controls on soil moisture-boundary layer Interactions. Part II: feedbacks within the continental United States, *Journal of Hydrometeorology*, *4*, 570-583.

Findell, K. L., and E. A. B. Eltahir (2003b), Atmospheric controls on soil moisture-boundary layer Interactions. Part I: framework development, *Journal of Hydrometeorology*, *4*, 552-569.

Finnigan, J. J. (1985), Turbulent transport in plant canopies, in *The Forest-Atmosphere Interaction*, edited by B. A. Hutchison and B. B. Hicks, pp. 443-480, D. Reidel Publishing, Dordrecht, The Netherlands.

Freedman, J. M., D. R. Fitzjarrald, K. E. Moore, and R. K. Sakai (2001), Boundary layer clouds and vegetation–atmosphere feedbacks, *Journal of Climate*, *14*(2), 180-197.

Garc, J. A., M. L. Cancillo, and J. L. Cano (2002), A case study of the morning evolution of the convective boundary layer depth, *Journal of Applied Meteorology*, *2002*, 1053-1059.

Garratt, J. R. (1992), *The atmospheric boundary layer*, Cambridge University Press, Cambridge, England.

Giorgi, F., L. O. Mearns, C. Shields, and L. Mayer (1996), A regional model study of the importance of local versus remote controls of the 1988 drought and 1993 flood over the central United States, *Journal of Climate*, *9*, 1150-1162.

Goudriaan, J., and H. H. van Laar (1994), *Modelling potential crop growth processes*, Kluwer Academic Publishers, Dordrecht, Netherlands.

Goulden, M. L., J. W. Munger, S.-M. Fan, B. C. Daube, and S. C. Wofsy (1996), Exchange of carbon dioxide by a deciduous forest: response to interannual climate variability, *Science*, *271*, 1576-1578.

Haiden, T. (1997), An analytical study of cumulus onset *Quarterly Journal of the Royal Meteorological Society*, *123 (543), Part A*, 1945-1960.

Hamilton, J. G., E. H. DeLucia, K. George, N. S. L., A. C. Finzi , and W. H. Schlesinger (2002), Forest carbon balance under elevated CO_2, *Oecologia*, *131*, 250-260.

Holland, E. A., S. Brown, C. S. Potter, S. A. Klooster, S. Fan, M. Gloor, J. Mahlman, S. Pacala, J. Sarmiento, T. Takahashi, and P. Tans (1999), North American carbon sink, *Science*, *283*, 1815.

Houghton, R. A., E. A. Davidson, and G. M. Woodwell (1998), Missing sinks, feedbacks, and understanding the role of terrestrial ecosystems in the global carbon balance, *Global Biogeochemical Cycles*, *12*, 25-34.

Houghton, R. A. (2000), Interannual variability in the global carbon cycle, *Journal of Geophysical Research-Atmospheres*, *105*, 20121-20130.

Hsieh, C. I., M. Siqueira, G. G. Katul, and C. R. Chu (2003), Predicting scalar source-sink and flux distribution withins within a forest canopy using 2-D Lagrangian Stochastic Model, *Boundary-Layer Meteorology*, *109*, 113-138.

Jackson, P. S. (1981), On the displacement height in the logarithmic velocity profile, *Journal of Fluid Mechanics*, *111*, 15-25.

Juang, J.-Y., G. G. Katul, A. Porporato, P. C. Stoy, M. Siqueira, M. Detto, H.-S. Kim, and R. Oren (2007a), Eco-hydrological controls on summertime convective rainfall triggers, *Global Change Biology*, in press.

Juang, J.-Y., A. Porporato, P. C. Stoy, M. B. S. Siqueira, O. C. A, M. Detto, H.-S. Kim, and G. G. Katul (2007b), Hydrologic and atmospheric controls on Initiation of convective precipitation events, *Water Resources Research*, in press.

Juang, J.-Y., A. Porporato, P. C. Stoy, M. B. S. Siqueira, O. C. A, M. Detto, H.-S. Kim, and G. G. Katul (in press), Hydrologic and Atmospheric Controls on Initiation of Convective Precipitation Events, *Water Resources Research*.

Juang, J., G. G. Katul, M. B. S. Siqueira, P. C. Stoy, S. Palmroth, H. R. McCarthy, H. Kim, and R. Oren (2006), Modeling nighttime ecosystem respiration from measured CO_2 concentration and air temperature profiles using inverse methods, *Journal of Geophysical Research-Atmospheres*, *111*, D08S05.

Kaimal, J. C., and J. E. Gaynor (1991), Another look at sonic thermometry, *Boundary-Layer Meteorology*, *56*, 401-410.

Kaimal, J. C., and J. J. Finnigan (1994), in *Atmospheric Boundary Layer Flows: Their Structure and Measurements*, edited, p. 289, Oxford University Press.

Kanae, S., T. Oki, and K. Musiake (2002), Impact of deforestation on regional precipitation over the Indochina Peninsula, *Journal of Hydrometeorology*, *2*, 51-70.

Katul, G., R. Leuning, and R. Oren (2003), Relationship between plant hydraulic and biochemical properties derived from a steady-state coupled water and carbon transport model, *Plant Cell and Environment*, *26*, 339-350.

Katul, G. G., and M. B. Parlange (1994), On the active role of temperature in surface layer turbulence, *Journal of the Atmospheric Science*, *51*, 2181-2195.

Katul, G. G., R. Oren, D. S. Ellsworth, C. I. Hsieh, N. Phillips, and K. Lewin (1997), A Lagrangian dispersion model for predicting CO_2 sources, sinks, and fluxes in a uniform loblolly pine (*Pinus taeda L.*) stand, *Journal of Geophysical Research-Atmospheres*, *102*, 9309-9321.

Katul, G. G., and J. D. Albertson (1998), An investigation of higher-order closure model for a forested canopy, *Boundary-Layer Meteorology*, *89*, 47-74.

Katul, G. G., and J. D. Albertson (1999), Modeling CO_2 sources, sinks, and fluxes within a forest canopy, *Journal of Geophysical Research-Atmospheres*, *104*(D6), 6081-6091.

Katul, G. G., D. Ellsworth, and C.-T. Lai (2000), Modeling assimilation and intercellular CO_2 from measured conductance: A synthesis of approaches, *Plant Cell and Environment*, *23*, 1313-1328.

Katul, G. G., L. Mahrt, D. Poggi, and C. Sanz (2004), One and two equation models for canopy turbulence, *Boundary-Layer Meteorology*, *113*, 91-109.

Keeling, C. D., J. F. S. Chin, and T. P. Whorf (1996), Increased activity of northern vegetation inferred from atmospheric CO_2 measurements, *Nature*, *382*, 146-149.

Kim, C. P., and D. Entekhabi (1998), Feedbacks in the land-surface and mixed-layer energy budgets, *Boundary-Layer Meteorology*, *88*, 1-21.

Kirschbaum, M. U. F., M. Küppers, H. G. C. Schneider, and S. Noe (1998), Modelling photosynthesis in fluctuating light with inclusion of stomatal conductance, biochemical activation and pools of key photosynthetic intermediates, *Planta*, *204*, 16-26.

Lai, C.-T., G. G. Katul, D. Ellsworth, and R. Oren (2000a), Modelling vegetation-atmosphere CO_2 exchange by a coupled Eulerian-Langrangian approach, *Boundary-Layer Meteorology*, *95*, 91-122.

Lai, C.-T., G. G. Katul, R. Oren, D. Ellsworth, and K. Schafer (2000b), Modeling CO_2 and water vapor turbulent flux distributions within a forest canopy, *Journal of Geophysical Research-Atmospheres*, *105*(D21), 26333-26351.

Lai, C.-T., G. G. Katul, J. Butnor, D. Ellsworth, and R. Oren (2002a), Modelling night-time ecosystem respiration by a constrained source optimization method, *Global Change Biology*, *8*, 124-141.

Lai, C.-T., G. G. Katul, J. R. Butnor, M. Siqueira, D. S. Ellsworth, C. Maier, K. H. Johnsen, S. McKeand, and R. Oren (2002b), Modeling the limits on the response of net carbon exchange to fertilization in a southeastern pine forest, *Plant Cell and Environment*, *25*, 1095-1119.

Law, B. E., D. D. Baldocchi, and P. M. Anthoni (1999a), Below-canopy and soil CO_2 fluxes in a ponderosa pine forest, *Agricultural and Forest Meteorology*, *94*, 171-188.

Law, B. E., M. G. Ryan, and P. M. Anthoni (1999b), Seasonal and annual respiration of a ponderosa pine ecosystem, *Global Change Biology*, *5*, 169-182.

Lee, X. H., J. D. Fuentes, R. M. Staebler, and H. H. Neumann (1999), Long-term observation of the atmospheric exchange of CO_2 with a temperate deciduous forest in southern Ontario, Canada, , *Journal of Geophysical Research-Atmospheres*(104), 15975-15984.

Leuning, R., F. M. Kelliher, D. G. G. De Pury, and E.-D. Schulze (1995), Leaf nitrogen, photosynthesis, conductance and transpiration: scaling from leaves to canopies, *Plant Cell and Environment*, *18*, 1183-1200.

Leuning, R., and M. J. Judd (1996), The propagation of errors in long term measurements of land atmosphere fluxes of carbon and water, *Global Change Biology*, *2*, 231-240.

Leuning, R. (2000), Estimation of scalar sources/sink distributions in plant canopies using Lagrangian dispersion analysis: corrections for atmospheric stability and comparison with a multilayer canopy model, *Boundary-Layer Meteorology*, *96*, 293-314.

Lindroth, A., A. Grelle, and A.-S. Morén (1998), Long-term measurements of boreal forest carbon balance reveal large temperature sensitivity, *Global Change Biology*, *4*, 443-450.

Liston, G. E., J. P. Mcfadden, M. Sturm, and R. A. Pielke (2002), Modelled changes in arctic tundra snow, energy and moisture fluxes due to increased shrubs, *Global Change Biology*, *8*, 17-32.

Liu, J., T. A. Black, and M. D. Novak (1996), E-epsilon modeling of turbulent air flow downwind of a model forest edge, *Boundary-Layer Meteorology*, *77*, 21-44.

Luo, Y., B. Medlyn, D. Hui, D. S. Ellsworth, J. F. Reynolds, and G. Katul (2001), Gross primary productivity in the Duke Forest: Modeling synthesis of the free-air CO_2 enrichment experiment and eddy-covariance measurements, *Ecological Applications*, *11*, 239-252.

Malhi, Y., A. D. Nobre, J. Grace, B. Kruijt, M. G. P. Pereira, A. Culf, and S. Scott (1998), Carbon dioxide transfer over a Central Amazonian rain forest, *Journal of Geophysical Research-Atmospheres*, *103*, 31593-31612.

Massman, W. J., and J. C. Weil (1999), An analytical one-dimensional second-order closure model of turbulence statistics and the Lagrangian time scale within and above plant canopies of arbitrary structure, *Boundary-Layer Meteorology*, *91*, 81 –107.

Massman, W. J. (2000), A simple method for estimating frequency response corrections for eddy covariance systems, *Agricultural and Forest Meteorology*, *104*, 185-198.

McCarthy, H. R., R. Oren, A. C. Finzi, and K. H. Johnsen (2006a), Canopy leaf area constrains [CO_2]-induced enhancement of productivity and partitioning among aboveground carbon pools., *Proceedings of the National Academy of Sciences of the United States of America*, *103*, 19356-19361.

McCarthy, H. R., R. Oren, H.-S. Kim, K. H. Johnsen, C. Maier, S. G. Pritchard, and M. A. Davis (2006b), Interaction of ice storms and management practices on current carbon sequestration in forests with potential mitigation under future CO_2 atmosphere, *Journal of Geophysical Research-Atmospheres*, *111*, D15103.

McCarthy, H. R., R. Oren, A. C. Finzi , D. S. Ellsworth, H.-S. Kim, K. H. Johnsen, and B. Millar (in preparation), Temporal dynamics and spatial variability in the enhancement of canopy leaf area under elevated CO_2.

McCarthy, H. R., R. Oren, A. C. Finzi , D. S. Ellsworth, H.-S. Kim, K. H. Johnsen, and B. Millar (submitted to Global Change Biology), Temporal dynamics and spatial variability in the enhancement of canopy leaf area under elevated CO_2.

Mellor, G. (1973), Analytic prediction of the properties of stratified planetary boundary layer, *Journal of the Atmospheric Sciences, 30*, 1061-1069.

Mellor, G., and T. Yamada (1974), A hierarchy of turbulence closure models for plenstary boundary layers, *Journal of the Atmospheric Sciences, 31*, 1791-1806.

Meyers, T., and K. T. Paw U (1986), Testing of a higher-order closure model for modeling airflow within and above plant canopies, *Boundary-Layer Meteorology, 37*, 297-311.

Meyers, T., and K. T. Paw U (1987), Modeling the plant canopy micrometeorology with higher-order closure principles, *Agricultural and Forest Meteorology*, *41*, 143-163.

Moncrieff, J. B., Y. Malhi, and R. Leuning (1996), The propagation of errors in long-term measurements of land atmosphere fluxes of carbon and water *Global Change Biology, 2*, 231-240.

Mortazavi, B., J. P. Chanton, J. L. Prater, A. C. Oishi, R. Oren, and G. G. Katul (2005), Temporal variability in ^{13}C of respired CO_2 in a pine and a hardwood forest subject to similar climatic conditions, *Oecologia, 142*, 57-69.

Naumburg, E., and D. S. Ellsworth (2000), Photosynthetic sunfleck utilization potential of understory saplings growing under elevated CO_2 in FACE, *Oecologia*, *122*, 163-174.

Naumburg, E., D. S. Ellsworth, and G. G. Katul (2001), Modeling daily understory photosynthesis of species with differing photosynthetic light dynamics in ambient and elevated CO_2, *Oecologia, 126*, 487-499.

Novick, K. A., P. C. Stoy, G. G. Katul, D. Ellsworth, M. B. S. Siqueira, J.-Y. Juang, and R. Oren (2004), Carbon dioxide and water vapor exchange in a warm temperate grassland, *Oecologia*, *138*, 259-274.

Oosting, H. J. (1942), An ecological analysis of the plant communities of Piedmont, North Carolina, *American Midland Naturalist*, *28*, 1-126.

Oren, R., B. Ewers, P. Todd, N. Phillips, and G. G. Katul (1998), Water balance delineates the soil layer in which moisture affects canopy conductance, *Ecological Applications*, *8*, 990-1002.

Oren, R., and D. E. Pataki (2001), Transpiration in response to variation in microclimate and soil moisture in southeastern deciduous forests, *Oecologia*, *127*(4), 549-559.

Otterman, J. (1977), Anthropogenic impact on the albedo of the Earth, *Climatic Change*, *1*, 137-157.

Palmroth, S., C. A. Maier, H. R. McCarthy, A. C. Oishi, H.-S. Kim, K. H. Johnsen, G. G. Katul, and R. Oren (2005), Contrasting responses to drought of forest floor CO_2 efflux in a loblolly pine plantation and a nearby oak-hickory forest, *Global Change Biology*, *11*, 1-14.

Pan, Z., E. Takle, M. Segal, and R. Turner (1996), Influences of model parameterization schemes on the response of rainfall to soil moisture in the central United States, *Monthly Weather Review*, *124*, 1786-1802.

Parlange, M. B., and G. G. Katul (1992), Estimation of the diurnal variation of potential evaporation from a wet bare soil surface, *Journal of Hydrology*, *132*, 71-89.

Pataki, D. E., R. Oren, and D. Tissue (1998), Elevated carbon dioxide does not affect average canopy stomatal conductance of *Pinus taeda L.*, *Oecologia*, *127*, 549-559.

Pataki, D. E., and R. Oren (2003), Species differences in stomatal control of water loss at the canopy scale in a mature bottomland deciduous forest, *Advances in Water Resources*, *26*(12), 1267-1278.

Penman, H. L. (1948), Natural evaporation from open water, bare soil and grass, *Proceedings of the Royal Society of London Series A-Mathematical and Physical Sciences*, *193*, 120-146.

Poggi, D., G. G. Katul, and J. D. Albertson (2004), Momentum transfer and turbulent kinetic energy budgets within a dense model canopy, *Boundary-Layer Meteorology*, *111*, 589–614.

Priestley, C. H. B., and R. J. Taylor (1972), On the assessment of surface heat flux and evaporation using large scale parameters, *Monthly Weather Review*, *100*, 81-92.

Raupach, M. R. (1988), Canopy transport processes, in *Flow and Transport in the Natural Environment: Advances and Applications*, edited by W. L. Steffen and O. T. Denmead, pp. 95-127, Springer-Verlag, New York.

Raupach, M. R. (1989a), A practical Lagrangian method for relating scalar concentrations to source distributions in vegetation canopies, *Quarterly Journal of the Royal Meteorological Society, 115*, 609-632.

Raupach, M. R. (1989b), Applying Lagrangian fluid mechanics to infer scalar source distributions from concentration profiles in plant canopies, *Agricultural and Forest Meteorology, 47*, 85-108.

Richards, J. A. (1999), *Remote sensing digital image analysis*, Springer-Verlag, Berlin, German.

Schafer, K. V. R., R. Oren, D. S. Ellsworth, C.-T. Lai, J. D. Herrick, A. C. Finzi, D. D. Richter, and G. G. Katul (2003), Exposure to an enriched CO_2 atmosphere alters carbon assimilation and allocation in a pine forest ecosystem, *Global Change Biology, 9*, 1378–1400.

Schimel, D. S. (1995), Terrestrial ecosystems and the carbon cycle, *Global Change Biology, 1*, 77-91.

Schmid, H.-P., C. Susan, B. Grimmond, F. Cropley, B. Offerle, and H.-B. Su (2000), Measurements of CO_2 and energy fluxes over a mixed hardwood forest in the mid-western United States, *Agricultural and Forest Meteorology, 103*, 357-374.

Shaw, R. H., G. den Hartog, K. M. King, and G. W. Thurtell (1974), Measurements of mean wind flow and three-dimensional turbulence intensity within a mature corn canopy, *Agricultural and Forest Meteorology, 13*, 419-425.

Shaw, R. H. (1977), Secondary wind speed maxima inside plant canopies, *Journal of Applied Meteorology, 16*, 514-521.

Shaw, R. H., G. D. Hartog, and H. H. Neumann (1988), Influence of foliar density and thermal stability on profiles of Reynolds stress and turbulence intensity in a deciduous forest, *Boundary-Layer Meteorology, 45*(4), 391-409.

Simon, E., F. X. Meixner, L. Ganzeveld, and J. Kesselmeier (2005a), Coupled carbon-water exchange of the Amazon rain forest, I. Model description, parameterization and sensitivity analysis, *Biogeosciences, 2*, 231-253.

Simon, E., F. X. Meixner, U. Rummel, L. Ganzeveld, C. Ammann, and J. Kesselmeier (2005b), Coupled carbon-water exchange of the Amazon rain forest, II. Comparison of predicted and observed seasonal exchange of energy, CO_2, isoprene and ozone at a remote site in Rondônia, *Biogeosciences, 2*, 255-275.

Siqueira, M., and G. Katul (2002), Estimating heat sources and fluxes in thermally stratified canopy flows using higher-order closure models, *Boundary-Layer Meteorology*, *103*, 125-142.

Siqueira, M., G. G. Kutal, and C.-T. Lai (2002), Quantifying net ecosystem exchange by multilevel ecophysiological and turbulent transport models, *Advances in Water Resources*, *25*, 1357-1366.

Siqueira, M., R. Leuning, O. Kolle, F. M. Kelliher, and G. G. Katul (2003), Modeling sources and sinks of CO_2, H_2O and heat within a Siberian pine forest using three inverse methods, *Quarterly Journal of the Royal Meteorological Society*, *129*, 1373-1393.

Sperry, J. S. (2000), Hydraulic constraints on plant gas exchange, *Agricultural and Forest Meteorology*, *104*(1), 13-23.

Spitters, C. J. T. (1986), Separating the diffuse and direct component of global radiation and its implications for modelling canopy photosynthesis. Part II. Calculation of canopy photosynthesis, *Agricultural and Forest Meteorology*, *38*, 238-241.

Spitters, C. J. T., H. A. J. M. Toussaint, and J. Goudriaan (1986), Separating the diffuse and direct component of global radiation and its implications for modelling canopy photosynthesis. Part I. Components of incoming radiation., *Agricultural and Forest Meteorology*, *38*, 225-237.

Sreenivasan, K. R., S. Tavoularis, and S. Corrsin (1982), A test of gradient transport and its generalization, in *Turbulent Shear Flow III*, edited, pp. 96-112, Springer-Verlag, New York.

Stenberg, P. (1998), Implications of shoot structure on the rate of photosynthesis at different levels in a coniferous canopy using a model incorporating grouping and penumbra, *Functional Ecology*, *12*, 82-91.

Stoy, P., G. G. Katul, M. B. S. Siqueira, J.-Y. Juang, H. R. McCarthy, H.-S. Kim, C. Oishi, and R. Oren (2005), Variability in net ecosystem exchange from hourly to inter-annual time scales at adjacent pine and hardwood forests: a wavelet analysis, *Tree Physiology*, *25*, 887-902.

Stoy, P., G. G. Katul, M. B. S. Siqueira, J.-Y. Juang, K. A. Novick, J. M. Uebelherr, and R. Oren (2006), An evaluation of models for partitioning eddy covariance-measured net ecosystem exchange into photosynthesis and respiration, Agricultural and Forest Meteorology, *Agricultural and Forest Meteorology*.

Stull, R. B. (1976), The energetics of entrainment across a density interface, *Journal of the Atmospheric Sciences*, *33*, 1260-1267.

Stull, R. B. (1988), *An Introduction to Boundary Layer Meteorology*, 666 pp., Kluwer Academic Publishers Group, Dordrecht, The Netherlands.

Styles, J. M., M. R. Raupach, G. D. Farquhar, O. Kolle, K. A. Lawton, W. A. Brand, R. A. Werner, A. Jordan, E. D. Schulze, O. Shibistova , and J. Lloyd (2002), Soil and canopy CO_2, $^{13}CO_2$, H_2O and sensible heat flux partitions in a forest canopy inferred from concentration measurements, *Tellus Series B-Chemical and Physical Meteorology*, *54B*, 655-676.

Tans, P. P., and J. W. C. White (1998), In balance, with a little help from the plants, *Science*, *281*, 183-184.

Tennekes, H. (1973), A model for the dynamics of the inversion above a convective boundary layer, *Journal of the Atmospheric Sciences*, *30*, 558-567.

Thom, A. S. (1971), Momentum absorption by vegetation, *Quarterly Journal of the Royal Meteorological Society*, *97*, 414-428.

Trenberth, K. E., and C. J. Guillemont (1996), Physical processes involved in the 1988 drought and 1993 floods in North America, *Journal of Climate*, *9*, 1288-1298.

Valentini, R., G. Matteucci, A. J. Dolman, E.-D. Schulze, C. Rebmann, E. J. Moors, A. Granier, N. O. J. P. Gross, K. Pilegaard, A. Lindroth, A. Grelle, C. Bernhofer, T. Grünwald, M. Aubinet, R. Ceulemans, A. S. Kowalski, T. Vesala, O. Rannik, P. Berbigier, D. Loustau, J. Gu, H. Thorgeirsson, A. Ibrom, K. Morgenstern, R. Clement, J. Moncrieff, L. Montagnani, S. Minerbi, and P. G. Jarvis (2000), Respiration as the main determinant of carbon balance in European forests, *Nature*, *404*, 861-865.

Wang, Y. P., and R. Leuning (1998), A two-leaf model for canopy conductance, photosynthesis and partitioning of available energy I: Model description and comparison with a multi-layered model, *Agricultural and Forest Meteorology*, *91*, 89-111.

Wear, D. N., and J. G. Greis (Eds.) (2002), *Southern forest resource assessment. Gen. Tech. Rep. SRS-53*, 635 pp., U.S. Department of Agriculture, Forest Service, Southern Research Station, Asheville, NC.

Webb, E. K., G. I. Pearman, and R. Leuning (1980), Correction of flux measurements for density effects due to heat and water vapour transfer, *Quarterly Journal of the Royal Meteorological Society*, *106*, 85-100.

Weiss, A., and J. M. Norman (1985), Partitioning solar radiation into direct and diffuse, visible and near-infrared components, *Agricultural and Forest Meteorology*, *34*, 205-213.

Wetzel, P. J. (1990), A simple parcel method for prediction of cumulus onset and area-averaged cloud amount over heterogeneous land surfaces, *Journal of Applied Meteorology*, *29*(6), 516-523.

Williams, M., E. B. Rastetter, D. N. Fernades, M. L. Goulden, S. C.Wofsy, G. R. Shaver, J. M. Meillo, J. W. Munger, S. M. Fan, and K. J. Nadelhoffer (1996), Modeling the soil-plant-atmosphere continuum in a Quercus-Acerstand at Harvard Forest: The regulation of stomatal conductance by light, nitrogen and soil/plant hydraulic properties, *Plant, Cell, and Environment*, *19*, 911-927.

Williams, M., Y. Malhi, A. D. Nobre, E. B. Rastetter, J. Grace, and M. G. P. Pereira (1998), Seasonal variation in net carbon exchange and evapotranspiration in a Brazilian rain forest: a modelling analysis, *Plant, Cell, and Environment*, *21*, 953-968.

Wilson, J. D. (1989), Turbulent transport within the plant canopy, in *Estimation of Areal Evapotranspiration*, edited, pp. 43-80, IAHS Pub., Gentbrugge, Belgium.

Wilson, N. R., and R. H. Shaw (1977), A higher order closure model for canopy flow, *Journal of Applied Meteorology*, *16*, 1198-1205.

Wofsy, S. C., M. L. Goulden, J. W. Munger, S.-M. Fan, P. S. Bakwin, B. C. Daube, S. L. Bassow, and F. A. Bazzaz (1993), Net exchange of CO_2 in a mid-latitude forest., *Science*, *260*, 1314-1317.

Woodwell, G. M., and W. R. Dykeman (1966), Respiration of a Forest Measured by Carbon Dioxide Accumulation during Temperature Inversions, *Science*, *154*, 1031-1034.

Wu, W., and R. E. Dickinson (2005), Warm-season rainfall variability over the U.S. Great Plains and its correlation with evapotranspiration in a climate simulation, *Geophysical Research Letters*, *32*(17), L17402.

Zilitinkevich, S. S. (1972), On the determination of the height of the Ekman boundary layer, *Boundary-Layer Meteorology*, *3*, 141-145.

Biography

JEHN-YIH JUANG

BIRTH PALACE & DATE

Born in Chiayi, Taiwan on January 7, 1975

EDUCATION

Ph. D. (2001/09 ~ 2007/03), Nicholas School of the Environment and Earth Sciences, Duke University, Durham, NC, USA.

M.S. (1997/09~ 1999/06), Graduate Institute of Environmental Engineering, National Taiwan University, Taipei, Taiwan.

B.S. (1993/09~ 1997/06), Department of Civil Engineering, National Taiwan University, Taipei, Taiwan.

RESEARCH/WORKING EXPERIENCE

1. **Postdoctoral Research Fellow** (expected to start in March 2007), Atmospheric Sciences Modeling Division, National Oceanic & Atmospheric Administration (NOAA) and Environmental Protection Agency (EPA), Research Triangle Park, NC, USA
2. **Graduate Research Assistant** (2001~2007), Biosphere-Atmosphere Interaction Laboratory (Dr. Gabriel G. Katul), Duke University, Durham, NC, USA
3. **Environmental engineer** (2001), Dao-Cheng Engineering Consultants LTD., Taipei, Taiwan
4. **Programming officer/Infantry platoon leader (Rank: Second Lieutenant)** (1999~2001), Taiwanese Marine Corps Command, Taiwanese Ministry of National Defense, Kaohsiung, Taiwan
5. **Graduate Research Assistant** (1997~1999), Atmospheric Pollution Modeling Laboratory (Dr. Len-Fu W. Chang), National Taiwan University, Taipei, Taiwan
6. **Graduate Research Assistant** (1997~1999), Taiwan's Environmental Protection Administration, Taipei, Taiwan

7. **Undergraduate Research Assistant** (1995~1996), Rock Mechanics Laboratory (Dr. Fu-Shu Jeng), National Taiwan University, Taipei, Taiwan

TEACHING EXPERIENCE

1. **Teaching Assistant** (2005), Nicholas School of the Environment and Earth Sciences, Duke University, Durham, NC, USA. Course: Differential Equations in Environmental Sciences (graduate course)
2. **Teaching Assistant** (1998), Graduate Institute of Environmental Engineering, National Taiwan University, Taipei, Taiwan. Course: Environmental Fluid Mechanism (graduate course)
3. **Teaching Assistant** (1997), Department of Civil Engineering, National Taiwan University, Taipei, Taiwan. Course: Introduction to Environmental Engineering (undergraduate course)

AWARDS AND HONORS

1. **Postdoctoral Research Fellowship** (2007/03 ~ 2008/02), Oak Ridge Institute for Science and Education (ORISE), Oak Ridge, TN, USA (Funding sources: US EPA, US DOE, and NOAA).
2. **Research Assistantship** (2001~2007), Nicholas School of the Environment and Earth Sciences, Duke University, Durham, NC, USA
3. **Excellent Master Thesis Award** (1999), Graduate Institute of Environmental Engineering, National Taiwan University, Taipei, Taiwan.
4. **Sinotech Engineering Research Scholarship** (1998), Sinotech Engineering Consultants LTD., Taipei, Taiwan.
5. **Excellent Award in Engineering Technology Contest** (1996), College of Engineering, National Taiwan University, Taipei, Taiwan

INVITED TALKS

1. "*Investigating biosphere-atmosphere interactions from leaf to atmospheric boundary layer scales*", Atmospheric Sciences Modeling Division, National Oceanic & Atmospheric Administration (NOAA) and Environmental Protection Agency (EPA), Research Triangle Park, NC, USA. January 11, 2007.
2. "*Eco-hydrological Controls on Growing-Season Convective Rainfall Events in a Southeastern US Mosaic Landscape*", Department of Atmospheric Sciences, National Taiwan University, Taipei, Taiwan. October 24, 2006.

3. "*Investigating biosphere-atmosphere interactions from leaf to atmospheric boundary layer scales*", National Center for High-Performance Computing (NCHC) & National Center for Typhoon and Flooding Research (NCTFR), Hsinchu Science Park, Taiwan. October 13, 2006.

PROFESSIONAL LICENSE

Professional Engineer Certificate in Hydraulic Engineering (1998), Taiwanese Ministry of Economic Affairs, Taipei, Taiwan

PROFESSIONAL AFFILIATION

American Geophysical Union

JOURNAL PUBLICATIONS

1. Detto M., Katul G. G., Siqueira M., **Juang J.-Y.**, and Stoy P. (2007) *The structure of turbulence near a tall forest edge: The backward facing step flow analogy*. Ecological Applications (in press)
2. **Juang J.-Y.**, Katul G. G., Porporato A., Stoy P. C., Siqueira M. S., Detto M., Oishi A. C., Kim H.-S., Oren R. (2007), *Eco-hydrological controls on triggers of summertime convective rainfall*. Global Change Biology (in press) doi: 10.1111/j.1365-2486.2007.01315.x.
3. **Juang J.-Y.**, Porporato A., Stoy P. C., Siqueira M. B. S., Oishi A. C., Detto M., Kim H.-S., Katul G. G. (2007), *Hydrologic and Atmospheric Controls on Initiation of Convective Precipitation Events*. Water Resources Research (in press).
4. Katul G. G., Porporato1 A., Oishi A. C., Kim H.-S., Stoy S., **Juang J.-Y.**, Daly E., Siqueira M. B. S. (2007) *On the spectrum of soil moisture in a shallow-rooted uniform pine forest: from hourly to inter-annual scales*. Water Resources Research (in press).
5. Stoy P, Palmroth S., Oishi A. C., Siqueira M. B.S., **Juang J.-Y.**, Novick K. A., Ward E. J, Katul G. G, Ram Oren R, (2007). *Are ecosystem carbon inputs and outputs coupled at short time scales? A case study from adjacent pine and hardwood forests using impulse-response analysis*. Plant Cell and Environment (in press).
6. **Juang, J.-Y.**, Katul G. G., Siqueira M. B. S., Stoy P. C., Palmroth S., McCarthy H. R., Kim H.-S., Oren R. (2006),Modeling nighttime ecosystem respiration from

measured CO2 concentration and air temperature profiles using inverse methods, Journal of Geophysical Research- Atmospheres, 111: D08S05 doi:10.1029/2005JD005976

7. Stoy P. C., Katul G. G., Siqueira M. B. S., **Juang J.-Y.**, Novick, K. A., Oren R. (2006). *An evaluation of methods for partitioning eddy covariance-measured net ecosystem exchange into photosynthesis and respiration*. Agricultural and Forest Meteorology, 141: 2-18.
8. Stoy P. C., Katul G. G., Siqueira M. B. S., **Juang J.-Y.**, McCarthy H. R., Oishi A. C., Uebelherr J. M., Kim H.-S., Oren R. (2006), *Separating the effects of climate and vegetation on evapotranspiration along a successional chronosequence in the southeastern U.S.* Global Change Biology, 12: 2115-2135.
9. Siqueira M. B. S., Katul G. G., Sampson D. A., Stoy P. C., **Juang J.-Y.**, McCarthy H. R., Oren R. (2006). *Multi-scale model inter-comparisons of CO2 and H2O exchange in a maturing southeastern U.S. pine forest*. Global Change Biology, 12: 1189–1207.
10. Stoy P. C., Katul G. G., Siqueira M. B. S., **Juang J.-Y.**, McCarthy H. R., Kim H.-S., Oishi A. C., Oren R. (2005), *Variability in net ecosystem exchange from hourly to inter-annual time scales at adjacent pine and hardwood forests: a wavelet analysis*. Tree Physiology 25: 887-902.
11. Novick K. A., Stoy P. C., Katul G. G., Ellsworth D. E., Siqueira M. B. S., **Juang J.-Y.**, Oren R. (2004), *Carbon dioxide and water vapor exchange in a warm temperate grassland*. Oecologia, 138: 259-274.
12. **Juang J.-Y.**, Siqueira M. B. S., Stoy P. C., Katul G. G. (in review) *Investigating a hierarchy of Eulerian closure models for scalar transfer inside forested canopies*, Boundary-Layer Meteorology.
13. **Juang J.-Y.**, Stoy P. C., Siqueira M. B. S., Katul G. G. (to be submitted) *Separating the effects of albedo from eco-physiological changes on surface temperature along a successional chronosequence in the Southeastern US*, Geophysical Research Letters.

CONFERENCE PRESENTATIONS/PUBLICATIONS

As Primary Author

1. **Juang, J.-Y.**, G. G. Katul, A. Porporato, P. C. Stoy, M. B. S. Siqueira. *The effect of land cover on growing-season convective precipitation*. American Geophysical Union 2006 Fall Meeting, December 11-15, 2006, San Francisco CA.
2. **Juang, J.-Y.**, A. Porporato, P. C. Stoy, M. B. S. Siqueira, A. C., Oishi, H.-S. Kim, J. Uebelherr and G. G. Katul. *The effect of land cover change on the convective*

precipitation during the growing season in the Southeastern United States. American Geophysical Union 2005 Fall Meeting, December 5-9, 2005, San Francisco CA.

3. **Juang, J.-Y.**, A. Porporato, P. C. Stoy, M. S. S. Siqueira, and G. G. Katul, *Investigating hydrologic and atmospheric pathways to summertime convective rainfall in the Southeastern United States*, American Geophysical Union 2005 Joint Assembly, May 23-27, 2005, New Orleans LA.
4. **Juang, J.-Y.**, P. C. Stoy, M. Siqueira, and G. G. Katul (2004), *Constraining Night Time Ecosystem Respiration by Inverse Approaches*, American Geophysical Union 2004 Fall Meeting, December 13-17, 2004, San Francisco CA.
5. **Juang, J.-Y.**, G.G. Katul, M. Siqueira, and P. Stoy (2003) *How Complex Must the Parameterization of Canopy Turbulent Transport Be to Capture Biophysical Sources and Sinks?* American Geophysical Union 2003 Fall Meeting, December 8-12, 2003, San Francisco CA.
6. **Juang, J.-Y.** and G.G. Katul (2002), *The Role of Thermal Stratification in Modeling Biosphere-Atmosphere Scalar Fluxes*, American Geophysical Union 2002 Spring Meeting, May 28-31, 2002, Washington DC.

Contribution to conference presentation/publication

7. Novick K. A., Katul G. G., **Juang J.-Y.** and Siqueira M. (2006), *Inter-specific Variation in Canopy Conductance With Tree Height*, 91st ESA Annual Meeting, August 6-11, 2006, Memphis, TN.
8. Stoy, P. C., Katul G. G., **Juang J.-Y.** and Novick K. A. (2006), *Explaining the Interannual Variability of Carbon Exchange in Successional Ecosystems*, 91st ESA Annual Meeting, August 6-11, 2006, Memphis, TN.
9. Daly E, **Juang J.-Y.**, Siqueira M., Stoy P., Maggi F., Oren R., and Katul G. G., *Subsurface Soil CO_2 Concentration Dynamics: Data Analysis and Stochastic Modeling.* American Geophysical Union 2006 Fall Meeting, December 11-15, 2006, San Francisco CA.
10. Siqueira M., Katul G., **Juang J.-Y.**, Novick K., *A Coupled Soil-Plant Hydrodynamics Model for the Soil-Plant System* American Geophysical Union 2006 Fall Meeting, December 11-15, 2006, San Francisco CA.
11. Katul G. G., Siqueira M. B. S., Stoy P. C., **Juang J.-Y.**, Palmroth S., Daly E., Poggi D., Porporato A., Oren R. (2005) *Multiscale models of biosphere-atmosphere exchange rates of H_2O and CO_2: Crossing the seconds to years and leaf to canopy scale barriers*. 3rd CNR-Princeton workshop, May 17-20, 2005, Princeton, NJ.
12. Siqueira M., G. Katul, D. Sampson, P. Stoy, **J.-Y. Juang**, H. McCarthy, R. Oren (2005). *Multi-scale Model Inter-comparisons of CO_2 and H_2O Exchange Rates in*

a Maturing Southeastern U.S. Pine Forest. American Geophysical Union 2005 Fall Meeting, December 5-9, 2005, San Francisco CA.

13. Stoy, P. C., Katul G. G., Siqueira M. B., **Juang J.-Y.**, Novick K. A., Oren R. (2005), *Vegetative controls on coupled ecosystem water and carbon fluxes on hourly to successional temporal scales*. American Geophysical Union 2005 Fall Meeting, December 5-9, 2005, San Francisco CA.
14. Stoy P. C., Katul G. G., Siqueira M. B. S., **Juang J.-Y.**, Palmroth S., Kim, H.-S., McCarthy H., Oishi A. C., Uebelherr J. M., Oren R. (2005). *The carbon and water cycles in SE piedmont ecosystems: Insights from 17 site-years of eddy covariance data*. 2005 Southeastern Evolution and Ecology Conference, March 11-13, 2005, Athens, GA.
15. Siqueira M. B. S., Katul G. G., Samson D. A., Stoy P. C., **Juang J.-Y.**, Oren R. (2004) *Nesting high-resolution multi-layer photosynthesis approaches in current forest productivity models: A Cost-Benefit Analysis in the Time-Frequency Domain*. American Geophysical Union 2004 Fall Meeting, December 13-17, 2004, San Francisco CA.
16. Stoy P. C., Katul G. G., Siqueira M. B. S., **Juang J.-Y.**, McCarthy H. R., Kim H.-S., Oishi A. C., Oren R. (2004) *Modeling net ecosystem exchange at multiple time scales in a pine and a hardwood forest*. Pages 375-381. In Hasenauer H and Mäkelä A. eds. Proceedings of the International Conference on Modeling Forest Production. Department of Forest and Soil Sciences. BOKU University of Natural Resources and Applied Life Sciences, April 19–22, 2004,Vienna, Austria.
17. Stoy P. C., Katul G. G., **Juang J.-Y.**, Siqueira M., Palmroth, S., Kim H.-S., McCarthy H., Oishi A. C., Uebelherr J. M., Oren R. (2004). *Interactions between the carbon and water cycles along a successional gradient in the southeastern US*. American Geophysical Union 2004 Fall Meeting, December 13-17, 2004, San Francisco CA.
18. Katul G. G., Oren R, Stoy P. C., Siqueira M. B. S., McCarthy H. R., **Juang J.-Y.** (2003) *Ecosystem Water and Carbon States: A Dynamical Systems View*. American Geophysical Union 2003 Fall Meeting, December 8-12, 2003, San Francisco CA.
19. Oren R., Katul G. G., Stoy P. C., Siqueira M. B. S., **Juang J.-Y.**, Palmroth S., Albertson J. D. (2003) *Controls of Net Ecosystem Exchange at an Old Field, a Pine Plantation, and a Hardwood Forest under Identical Climatic and Edaphic Conditions*. AmeriFlux Meeting, Boulder, CO.
20. Siqueira M. B. S., Schlesinger W. H., Katul G. G., Oren R., Stoy P. C., **Juang J.-Y.**, Palmroth S. (2003) *Assessing Ecological Models of Varying Complexity for Predicting Carbon Sequestration in Managed Pine Plantations*. National Institute for Global Environmental Change (NIGEC) Meeting, Indianapolis, IN.

21. Siqueira M. B. S., Katul G. G. Stoy P. C., **Juang J.-Y.** (2003). *Evaluating Three Forest Growth Models of Varying Complexities with Data from a Southern US Loblolly Pine Forest under Ambient and Elevated Atmospheric CO_2*. 2003 AGU/EGF Joint Assembly, Nice, France.

22. Siqueira, MBS, Katul G. G., Stoy P. C., **Juang J.-Y.** (2003) *Evaluating three forest growth models for a southern US loblolly pine forest under ambient and elevated atmospheric CO_2*. 18th International Conference on Transport Theory, July 20-25, 2003, Rio de Janeiro, Brazil.

23. Stoy P. C., Katul G. G., Siqueira M. B. S., **Juang J.-Y.**, Oren R. (2003) *Controls of net ecosystem exchange at an old field, a pine plantation, and a hardwood forest under identical climatic and edaphic conditions*. 88th ESA Annual Meeting, August 3-8, 2003, Savannah, GA.